Development and Simulation of an Active Load Cell Test Rig

A Thesis

Presented to

the faculty of the School of Engineering and Applied Science

University of Virginia

---

in partial fulfillment
of the requirements for the degree

Master of Science

by

Paul Gancitano

August 2017

APPROVAL SHEET

This Thesis
is submitted in partial fulfillment of the requirements
for the degree of
Master of Science

Author Signature: 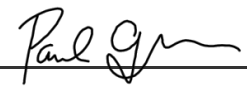

This Thesis has been read and approved by the examining committee:

Advisor: Zongli Lin

Committee Member: Roger Fittro

Committee Member: Gang Tao

Committee Member: _____

Committee Member: _____

Committee Member: _____

Accepted for the School of Engineering and Applied Science:

Craig H. Benson, School of Engineering and Applied Science

August 2017

Abstract

In industrial machinery, fluid-film bearings are used to support high-speed rotating masses in a low friction environment. As technology progresses, the need for higher machine speeds and loading conditions is a driving factor behind many cutting edge designs. Accurate knowledge of fluid-film bearing stiffness and damping coefficients can assist in vibration analysis to prevent a dangerous, costly, and time-consuming machine failure. Test rigs have been developed throughout the past three decades with the sole purpose of identifying these coefficients experimentally, however there is a need for higher accuracy measurements. The effective determination of fluid film bearing *force* is a necessary precursor to making accurate dynamic coefficient measurements, particularly at high frequencies. Current methods of force identification are indirect and subject to significant errors that compound at high frequencies to render these measurements inaccurate.

The "Active Load Cell" is a new experimental method of determining fluid-film bearing force without the need for inertial correction. A control algorithm works in conjunction with accelerometer readings and an electrodynamic shaker to adaptively cancel the motion of the bearing housing. This measurement method has the potential to determine bearing forces directly, to a higher degree of accuracy than previous force identification methods. This research details the development and simulation of an *Active Load Cell Test Rig*, which will be used to validate this concept prior to implementation within full-scale equipment. The results documented here suggest that bearing force amplitude and phase can be determined within 1% of true values across a wide range of test frequencies, stiffness, and dynamic loading conditions.

Acknowledgements

My experience at the University of Virginia has been both rewarding as well as challenging. I would like to thank my advisor, Zongli Lin, as well as my committee members and research mentors, Roger Fittro, Carl Knospe, and Gang Tao, for their assistance and support on this Master's research project. I am also grateful to the Rotating Machinery and Controls (ROMAC) laboratory and member companies at the University of Virginia for their resources and funding on this project. A special shout-out to Benstone Schwartz, who has been exceedingly patient and helpful over the past two years.

My parents have always been my biggest fans, pushing me to pursue my dreams and tackle larger and larger challenges, and without their continued love and support, I wouldn't be the man I am today. I owe them my utmost gratitude for being by my side through everything that life has thrown at me. Finally, a big thank you to my friends, who were always ready to provide a laugh, or at least a cold beer.

This work is dedicated to the memory of my grandparents, Stanley and Clara Szymanski. I am confident that they would both be extremely proud of all the accomplishments I have made throughout my college career and beyond.

Contents

List of Figures

List of Tables

1 Introduction

Across a wide array of applications, rotating machinery is utilized to convert rotating inertial energy into work. In the case of pumps, compressors, and engines, this work may be the transport or compression of a fluid. Generators or wind turbines my have the goal of generating electricity. Other applications feature the conversion of rotational motion to linear motion to actuate or drive a mechanism. In all of the above cases, rotating machinery relies on *bearings* to support the rotating shaft in a low friction environment. Bearings come in a variety of forms, but the majority of bearings can be categorized as either rolling element or fluid film bearings. Rolling element bearings feature a set of rolling elements between two running surfaces called races; these components offer a balance of efficiency, cost, and durability, however the cyclic stresses limit their capabilities in highly demanding applications. For applications that involve high load, speed, accuracy, and low friction operation, fluid-film bearings are often a better choice.

Fluid-film hydrodynamic bearings support the rotating mass on a thin lubricating film. Multiple geometry types exist, from basic cylindrical plain bearings to common tilting-pad bearings, which allow for the flexure of multiple bearing lobes to compensate for differing pressures within the fluid film. They also provide damping capabilities which help to reduce vibrations in rotating machinery that may occur. These types of bearings are the focus of many academic and industrial research projects, one of which is the *Fluid-Film Bearing Test Rig* (FFBTR) at the University of Virginia which will be referenced frequently throughout this paper.

1.1 Motivation

As technology and innovation progresses, rotating machinery operates at more demanding speed and load conditions. Higher rotational speeds allow for increased machine efficiency and higher power density. Some particular areas of advanced equipment design are in the petrochemical, oil and gas, and power generation industries. Oftentimes these ultramodern machines operate above one or more critical speeds or natural shaft frequencies, necessitating the need for advanced rotordynamic modeling studies. At very high speeds, the bearing fluid film may be in the turbulent regime which is difficult to fully analyze [2]. In addition, there is a complex interaction between thermal, mechanical and fluid dynamic behavior which is difficult to accurately model.

Machines typically are subjected to vibration analysis prior to construction in order to analyze dynamics and stability. However, there are numerous challenges in accurately modeling fluid-film bearing dynamics, for example the choice of synchronous vs. non-synchronous bearing coefficients, which turbulence model is employed, or which lubrication starvation method is used. All of these choices can severely impact the results of rotordynamic analysis [3]. Results from thermoelastohydrodynamic (TEHD) bearing analysis may be inaccurate [4], and an instability mechanism may be missed until it is encountered on the actual machine during the testing phase. This can result in a catastrophic failure and/or the need for a very expensive redesign.

Fluid-Film Bearing Test Rig The need for accurate fluid-film bearing properties gave birth to a research objective to develop a test facility that would be able to determine fluid-film bearing dynamic coefficients accurately, so that this data could be used by manufacturers and end-users to analyze their equipment and not encounter unsafe and costly downtime. A tabulation of fluid-film bearing coefficient determination endeavors and their uncertainty ranges are well documented in an article by T. Dimond et. al. in [5]. Within the Rotating Machinery and Controls Laboratory at the University of Virginia, there has been an ongoing fluid-film bearing test program for over three decades. This process began in 1985 and is detailed in a dissertation by L.J. Read and R.D. Flack, in "The Design and Implementation of a Fluid-Film Bearing Test Rig" [6].

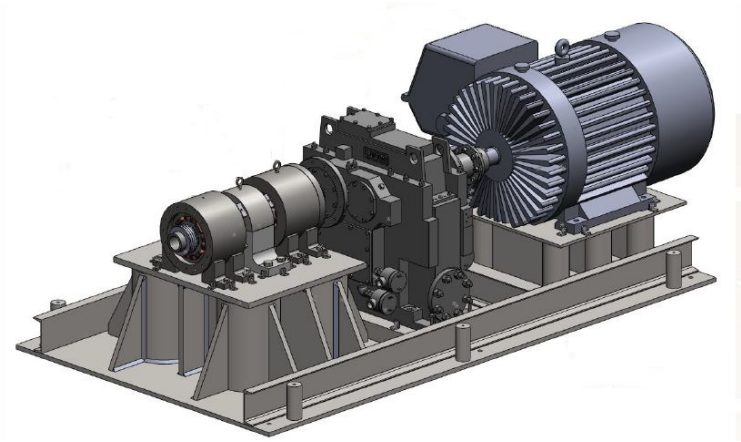

Figure 1.1: Fluid Film Bearing Test Rig design at the Rotating Machinery and Controls Lab at the University of Virginia (2011)

The newest fluid-film bearing test rig design began development in 2008 by T. Dimond, R. Rockwell, P. Sheth, and P. Allaire [3]. This rig is similar in construction to a rig design by Knopf and Nordmann in 2000 [7], but with higher operational load and speed capabilities. Full development of the FFBTR, in 2011, is covered in "Modeling of Fluid-Film Bearings and Design of a Fluid-Film Bearing Test Rig" [2]. Currently, the development of the Fluid-Film Bearing Test Rig is being headed by B. Schwartz, R. Fittro, and C. Knospe at the University of Virginia. Information on the development of this rig can be found in on the ROMAC Website [8].

Challenges The development of a high speed, high load fluid-film bearing test rig has not been without its challenges. Most notably, a consistent downfall to FFBTR development is the fact that bearing coefficients can not be measured directly; rather, they are derived from a series of other measurements based off of an applied dynamic load [9]. Typically in the test rigs, shakers are used to perturb the bearing housing while the shaft is rigidly held by ball bearings. Stiffness and damping coefficients can then be identified from dynamic force and displacement measurements [10]. A thorough overview of how uncertainties in force measurements affect the accuracy of the derived coefficients is documented by Kostrkewsky & Flack in [11].

At the time of the development of the FFBTR at the University of Virginia in 2008, two force measurement methods were being considered as part of this identification process. The first, as documented by Zutavern and Childs [12] utilizes fiber optic strain gages on the magnetic bearing poles and infers the applied force from the strain. The second is a technique studied by Knopf & Nordmann [7] / Aenis & Normann [13] and measures magnetic flux in the bearing poles to infer force. Other methods, such as identification with piezoelectric load cells [14], [15] and empirical formulae that relate magnetic bearing current to applied force [16] have been used. The common factor between all of these force determination methods is that they are all indirect; meaning the bearing force is estimated through other equipment or a mathematical process, which may have errors that render these estimates to be significantly inaccurate, especially at higher frequencies.

Introduction to the Active Load Cell No test rig to date has employed a direct method of measuring bearing force, leaving an opportunity for a new technology with this purpose. If bearing force can be measured directly, the compounded errors from other sources of measurement would be eliminated, and force measurements would be substantially more accurate. The *Active Load Cell* (ALC) is a new experimental method that aims to fill this void in force identification. Further sections will fully cover the ALC's theory and operation, but generally speaking, it relies on applying a dynamic force to the fluid-film bearing housing directly and monitoring the resulting housing acceleration. A controller can adaptively balance the bearing force through an iterative force identification process. The FFBTR can be modified to accept this setup and have its identifications improved by this technology. Prior to implementation, however, the aim is to validate this concept by analyzing its effectiveness in a controlled and separate setting. Thus there is a need for a new test rig, the *Active Load Cell Test Rig* (ALCTR), which will be a standalone study in observing the effectiveness of the ALC and identify challenges or downfalls with its design.

1.2 Objectives

The primary objective of this project is to determine the capability of the ALCTR to accurately identify fluid film bearing force amplitude and phase, across a range of test frequencies, dynamic excitation forces, and bearing stiffnesses. Confidence bounds can be developed on the rig's ability to make these identifications under a variety of systematic error sources and draw conclusions as to whether pursing the Active Load Cell as a viable source of force measurement is plausible. The degree of accuracy to which we can determine bearing force can be utilized in FFBTR models to make a more insightful prediction as to the types of errors that can be expected when determining bearing stiffness and damping coefficients. The target accuracy for force amplitude determination is +/- 1% of the true value and +/- 1 degree of force phase.

1.3 Organization of this Thesis

The development of the Active Load Cell test Rig was done from the ground up, and as such involved a constant back-and-forth iterative process between physical system modeling and component simulation. For that reason it is difficult to create a concise workflow. This thesis is presented in the following format for ease of readability, but all work was not necessarily done in a linear fashion.

Section 2 gives a background on the physical relationship between bodies subjected to external forces and vibrations in the most general sense. This section is provided to illustrate the theory behind the operation of the Active Load Cell, and provides the backbone for the future sections. Section 3 goes through the development of solid body modeling. This section comes before Simulation modeling because the development of coordinate frames and component interconnectivity is crucial to the understanding of the simulated environment. Section 4 comprises the bulk of this thesis, and goes into detail regarding component simulation, control schemes, data flow, and error modeling. Finally, section 5 presents the results of these simulations along with commentary on the efficacy of the Active Load Cell concept, its ability to meet the predetermined goals, insights into data trends or model inaccuracies, and future advancements that can be made in the continuing effort to develop this particular test rig.

2 Theory

2.1 Active Load Cell Concept

The primary goal of the active load cell is to provide a direct way of measuring bearing force without the need for inertial correction. This new method primarily relies on balancing dynamic forces on solid bodies and observing the acceleration over time. A look at several spring-mass-damper systems will serve as an introduction to the Active Load Cell's operation.

2.1.1 Physics

To understand the theory behind the Active Load Cell's primary operation, a Newtonian approach can be taken to analyze the system from a physics perspective. The study of fluid-film bearings and traditional vibration analysis are closely interconnected because fluid-film bearings behave similar to spring-damper systems under dynamic loading conditions. Understanding the response of a mass-spring-damper system can help develop more accurate dynamics for an entire rotating system.

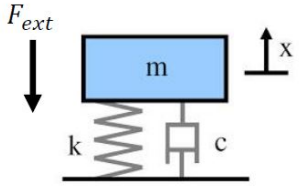

Figure 2.1: Diagram of a simple spring-mass-damper system

Example 1: Single Mass System Figure 2.1 shows a simple spring-mass-damper system along with a reference coordinate. The equation of motion for this system is defined by the general form in equation 2.1.

$$m\ddot{x} = -F_{ext} - c\dot{x} - kx \tag{2.1}$$

Where k is the stiffness constant of the spring, in N/m, c is the damping coefficient, in Nm/s, and m is the block mass, in kg. x gives the block's vertical position in m, $\dot{x}$ is the velocity in m/s, and $\ddot{x}$ is the acceleration in m/s^2.

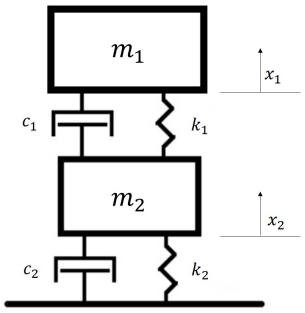

(a) Two-Mass system

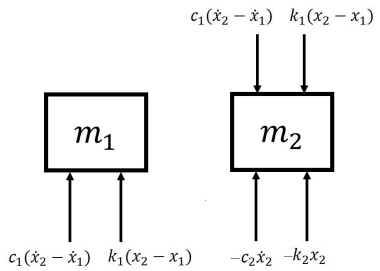

(b) Free-body diagrams of each mass

Example 2: Two-Mass System Figure 2.2a shows the same spring/damper system placed between two masses. The reference positions of each mass are shown along with a coordinate system convention. Forces from the spring and damper act between the two masses; spring force F_k is in proportion to their relative *displacement*, and damping force F_c is in proportion to their relative *velocity*. Free body diagrams for each mass are shown in figure 2.2b.

Example 3: Two-Mass System with External Forces Consider now the same two mass system as in Example 2, but instead it is being affected by external forces F_1 and F_2, as in figure 2.3. The equations of motion for the two masses in this system can be written as equations 2.2 and 2.3.

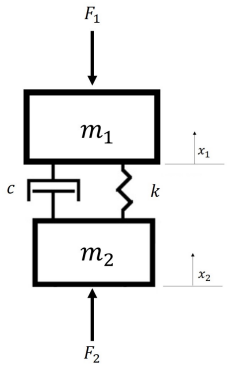

Figure 2.3: Two mass system with external forces

$$m_1\ddot{x}_1 = -F_1 + k(x_2 - x_1) + c(\dot{x}_2 - \dot{x}_1) \tag{2.2}$$

$$m_2\ddot{x}_2 = F_2 - k(x_2 - x_1) - c(\dot{x}_2 - \dot{x}_1) \tag{2.3}$$

As a shortcut, we can establish a new force, F_b, and define this as $F_b = k(x_2 - x_1) + c(\dot{x}_2 - \dot{x}_1)$. This force can be a basic representation of a fluid-film bearing connecting the two masses. F_1 and F_2 are external forces, and as such:

$$m_1\ddot{x}_1 = -F_1 + F_b \tag{2.4}$$

$$m_2\ddot{x}_2 = -F_b + F_2 \tag{2.5}$$

By observation, when the acceleration of a particular mass, say m_2, is exactly zero, that is, $\ddot{x}_2 = 0$, the forces acting on the body, F_b and F_2 would be equivalent. It is also important to note that in this case the value of F_b can be determined without any knowledge of F_1 if we know our input force F_2 exactly. Therefore by controlling external force F_2 and observing the acceleration $\ddot{x}_2$ we have all of the information we need to draw an accurate inference as to the value of F_b.

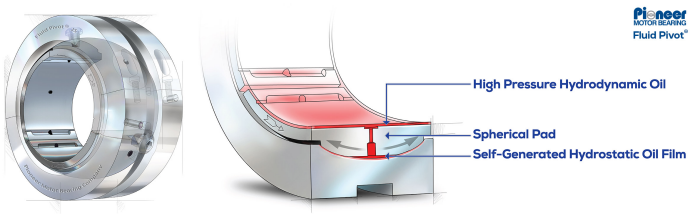

Figure 2.4: Fluid-Film tilt pad bearing, taken from the Pioneer Motor Bearing website [1]

Generally, in rotating machinery, the fluid-film bearing is situated between the *rotor*, which is a rotating mass, and a *housing*, which is static. The bearing force acts between these components, similar to F_b in figure 2.3. If we treat the rotor as mass m_1 and housing as mass m_2, this model becomes a basic representation of a cross-section of a rotating machine. The load on the rotor will have static and dynamic components due to equipment weights and imbalances, so we will need to expand the definition of applied forces. The true forces present on the rotor mass as a function of time are given by equation 2.6.

$$F_1(t) = F_{st} + A_p \cos(\omega_p t + \phi_p) \tag{2.6}$$

Here:

- A_p is the dynamic force amplitude, in N.
- ω_p is the frequency, in rad/s.
- ϕ_p is the phase, in rad.
- F_{st} is the static loading condition, in N.

The force required to bring the acceleration of m_2 to zero will also be dynamic in nature. The spring and damping coefficients of the bearing force will contribute to a change in amplitude and phase, however the applied frequency will be the same due to the conservation of energy. This external force that has the purpose of driving the acceleration to zero in attempt to make a force identification will be referred to as the *cancellation* force.

Dynamic Force Production In order to effectively produce a cancellation force at the test frequency, a mechanism capable of providing dynamic load to a high degree of accuracy and controllability is required. The most appropriate choice for this task is an electrodynamic shaker, shown in figure 2.5. These shakers are widely used in experimental test rigs in many applications, such as structural testing of buildings, shock loading on mechanical assemblies, and cyclic fatigue testing of materials. There are multiple sizes available, each with a force range and operational frequency bandwidth.

Figure 2.5: Two types of permanent magnet electrodynamic shakers, from Sentek Dynamics

These shakers operate by using electromagnetic induction. A wire is wound around a cylindrical coil that is part of the shaker armature and elastically suspended in a radial magnetic field. This results in an axial force acting on the armature in proportion to the applied current. The suspension holds the coil concentric within the magnetic field. It allows the armature to move a limited distance axially relative to the shaker body (displacement stroke), as depicted in Figure 2.6 [17].

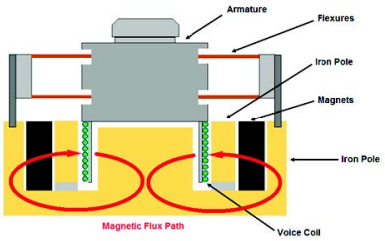

Figure 2.6: Components of an Electrodynamic Shaker, from Sentek Dynamics

This means that the dynamic force on the bearing housing can be precisely tuned by adjusting the phase and magnitude of the current into the shaker. The highly linear relationship between applied current and output force make these actuators ideal in critical applications where accuracy is imperative. These parameters can be adjusted using a controller that aims to *adaptively* cancel the effects of acceleration on the housing, as read by a sensor, in this case an *accelerometer*. More detail on the control system to accomplish this is covered in section 4.

2.1.2 Implementation within the FFBTR

A simplified schematic of the Fluid Film Bearing Test Rig is shown in figure 2.7a and consists of the following components:

- A steel *rotor*
- A fluid-film bearing, situated in a *housing*

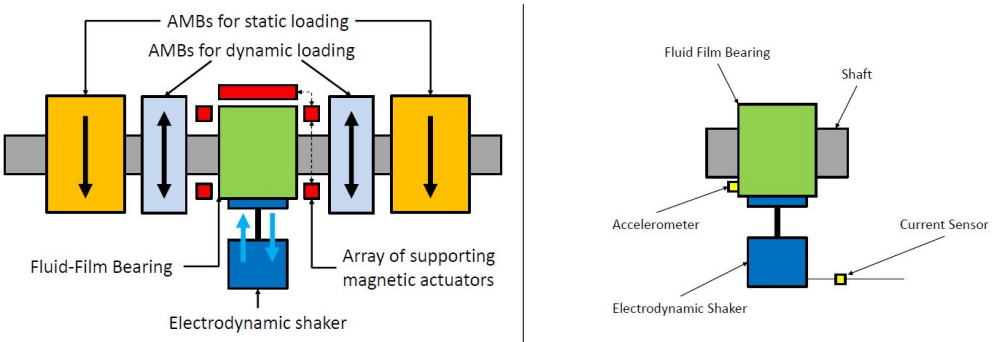

(a) FFBTR

(b) Active Load Cell assembly

Figure 2.7: Major System Components

- Active magnetic bearings to provide a dynamic excitation on the rotor
- Active magnetic bearings to provide a static load on the rotor
- An array of magnetic actuators supporting the bearing housing. These will stabilize the system in planes that are not being tested.

As mentioned in the introduction, in the past, dynamic stabilization on similar test rigs has been done through the active magnetic bearings. The forces these bearings apply was inferred through other measurement methods and not determined directly. The addition of an additional component, the electrodynamic shaker, is where the application of this experimental concept begins. This shaker is responsible for providing dynamic, adaptive *cancellation* forces directly on the bearing housing.

What is considered the *Active Load Cell* in relation to the FFBTR is shown in Figure 2.7b. This is comprised of the aforementioned shaker affixed to the bearing housing. The addition of (one or more) accelerometers on the bearing housing and current sensor on the shaker will complete the equipment necessary to build a controller to adaptively alter the effective cancellation force on the assembly. The control scheme follows that of a typical feedback control system, shown in Figure 2.8.

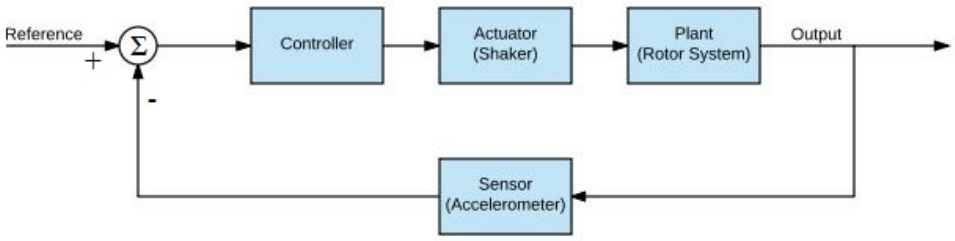

Figure 2.8: Feedback control system of the active load cell

The acceleration error is fed into the controller, which varies the current into the shaker. The altered force amplitude and phase attempt to drive the acceleration to zero, which is monitored by the accelerometer mounted to the fluid film bearing housing, and fed back into the control loop. More detail on the control system, including the algorithms applied, are covered in section 4.5.

2.2 Development of Experimental Test Rig

It would be a significant risk to modify the existing foundation to apply the ALC setup to the FFBTR without truly knowing its capabilities. For that reason, we want to develop a standalone test rig that can validate this concept. This controlled setting will allow the system capabilities, challenges, and downfalls to be identified.

The design of the active load cell test rig will feature components to replicate those that are involved in the FFBTR without rebuilding the entire complex structure. An initial mockup of this system was developed by C. Knospe and R. Fittro in an August 2015 proposal. This design served as a starting point for this Master's thesis project and has since been expanded and thoroughly analyzed. The rotor and housing will be simulated with solid body masses, and the static and dynamic loading will be provided by a secondary electrodynamic shaker rather than a magnetic bearing, for simpler construction and controllability. Rather than attempting to analyze a fluid directly, we will instead use a solid body that has been specially manufactured to have stiffness and damping coefficient similar to that of a fluid film. The principle of the operation is the same; this just makes it more accessible to swap out test pieces and attempt to identify forces for multiple bearing stiffnesses.

Section 3 details the mechanical design and how it is an effective representation of the simulated system.

2.2.1 Test Rig Overview

The block diagram in Figure 2.9 represents the high-level interaction between the Active Load Cell test rig components. This block model is helpful in understanding the construction of the physical rig, as well as the simulation model to be discussed in later sections.

Interconnectivity The excitation shaker will provide a dynamic force at a given test frequency, amplitude and bias (simulating a static load). This force will directly affect the rotor mass. A bearing component, that is situated between the rotor and housing masses, will provide an equal and opposite force between these bodies as discussed above. The housing mass will also have an electrodynamic shaker coupled to it that will provide the cancellation force at the same frequency, but with an amplitude and phase as dictated by the control loop.

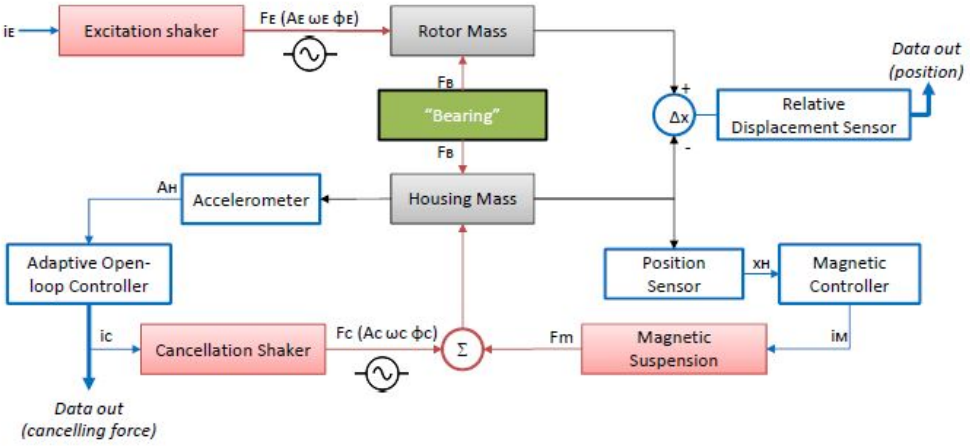

Figure 2.9: Block Diagram representation of Active Load Cell operation

Control loops The model will feature two independent control loops. The housing position will be tracked by four proximity sensors, which feed data into a controller that applies a current to the magnetic actuators. The purpose of this is to stabilize the platform at all frequencies that are not the test frequency. The second control loop reads data from an accelerometer mounted to the housing body and uses this information in the adaptive open loop controller. This controller is responsible for altering the current into the cancellation shaker to adaptively match the applied bearing force on the housing at the applied test frequency. The final bearing force will be in the form of equation 2.7.

$$F_b(t) = A_b cos(\omega_b t + \phi_b) \tag{2.7}$$

2.2.2 Expected Results

The goals of this thesis are as follows:

- Develop a simulation model that represents the Active Load Cell's construction.

- Use this simulation to test and verify the experimental concept.
- Develop confidence bounds on the ability of the rig to accurately determine bearing force amplitude & phase.

Results that are consistently within 1% of true bearing force will set this method apart as an excellent and reliable method of force determination. This test rig would also be versatile in the sense that it could be used for accurate force determination of any physical component that we can fit in the test bed. This could include thrust washers, O-rings, and squeeze film dampers.

3 Test Rig Mechanical Design

Introduction Prior to constructing any sort of simulation, the test rig needs to be designed from a physical perspective to know how the components should be interconnected, and to establish a coordinate and directional system. An early mockup of an ALCTR was provided by C. Knospe in 2015, and is shown below in figure 3.1. This model provided a rough outline for how the test rig could be constructed, however this model is conceptual and purely theoretical. The new model that has been developed for this Master's thesis provides a more thorough representation of a physical test rig, and sufficient analysis has been conducted using parameters taken from the solid model.

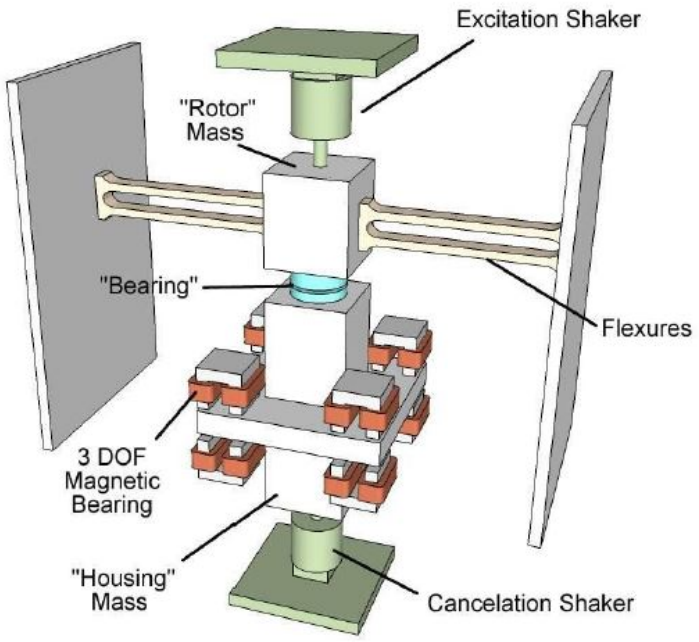

Figure 3.1: Conceptual design of a single-axis Active Load Cell experiment, developed by C. Knospe 2015.

Another important consideration is the ultimate use of the Active Load Cell within the fluid film bearing test rig. The development of the ALC and FFBTR are taking place side-by-side in order to design ALC test rig components to roughly replicate their respective masses on the full test rig. Initial design analyses of the FFBTR models the system with the parameters in Table 1. The ALCTR is designed with these specifications in mind, and as such the rotor and housing masses have a similar ratio.

Parameter	Value
Rotor mass	50 - 60 kg
Housing mass	40 - 50 kg
Bearing stiffness range	200000-1000000 lbf/in

Table 1: FFBTR Parameters

3.1 Solid Model

2017 Design The most recent mockup of the ALC in its entirety is shown in figure 3.2. All of the solid modeling was done using Autodesk Inventor 2016. This model reflects all major dimensions and build materials. A general overview of the components are provided in the list below.

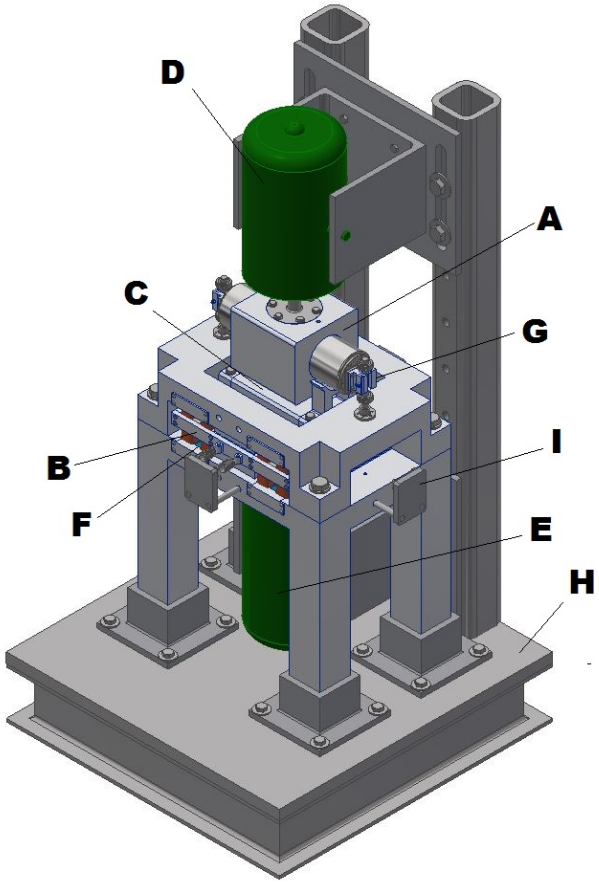

Figure 3.2: 2017 Design of the Active Load Cell Test Rig

Major components are labeled as follows:

- (A): Rotor Mass
- (B): Housing Mass
- (C): Test Bearing
- (D): Excitation Shaker
- (E): Cancellation Shaker
- (F): Electromagnetic Actuators
- (G): Linear Guide Rails
- (H): Foundation & support structure
- (I): Attachments for Housing Flexures

The Rig stands roughly 1.2 m (48 in) tall and can be mounted standalone or against a wall. The shaker mounting platforms are slotted to easily allow the upper assembly to be slid upwards to load in a bearing test piece, and lowered back down and secured into place. This model does not show auxiliary equipment such as data acquisition hardware. This section goes into further detail on the design of individual components and assemblies.

3.1.1 Rotor Mass

Component overview The rotor mass will be directly mounted to the excitation shaker and will receive excitation forces, both static and dynamic. This part features a cubic housing with a cylindrical insert which proximity sensors will be pointed towards in order to more closely resemble true rotor geometry (1). This mass will only have one degree of freedom, in order to reduce system complexity. It will be guided in the z-direction by the use of linear bearings (2), which move along solid shafts mounted to the test rig framework. The top side will feature a mounting bolt pattern where the stinger of the excitation shaker will attach (3). The underside features an adapter plate that surrounds the bearing test substrate to prevent it from dislodging or shifting excessively.

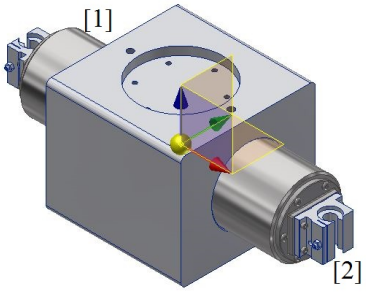

(a) Rotor Coordinate Convention

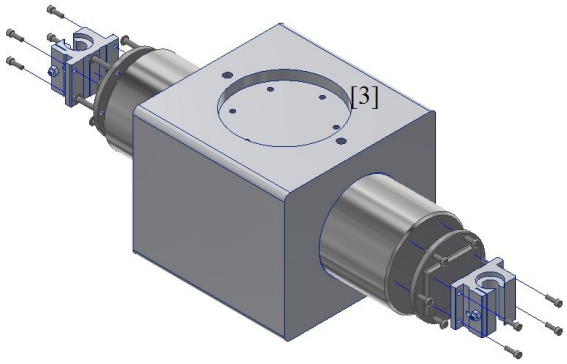

(b) Rotor Assembly

Figure 3.3: Rotor Mass

3.1.2 Housing Mass

Component overview The housing mass is roughly a rectangular prism, but also features a wide flange that will provide the surface area for the four magnetic actuators (1). Silicon iron inserts will be set in the aluminum body and secured into place with a retention bar (2). Like the rotor mass, the housing will feature a bolt pattern to attach to the cancellation shaker (underside) as well as an adapter plate to capture the bearing substrate on top (3).

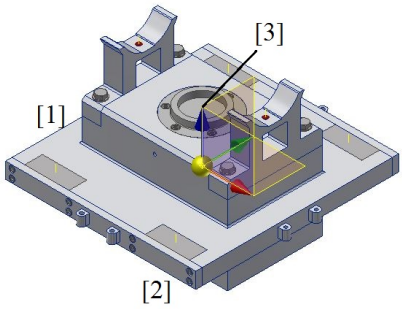

(a) Housing Coordinate Convention

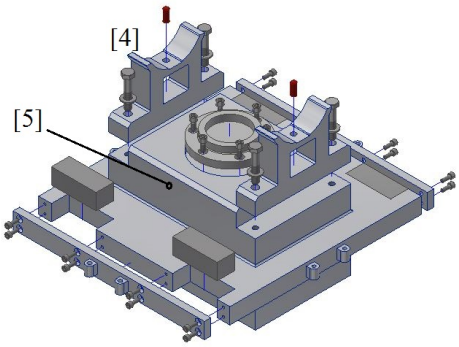

(b) Housing Assembly

Figure 3.4: Housing Mass

The housing mass will also feature two extension arms that match the rotor geometry (4). Displacement sensors will be mounted in two locations and point in the $+z$ direction at the rotor. While the primary objective of the Active Load Cell is to determine fluid film bearing *force*, by monitoring the relative displacement between the rotor and housing, we can also analyze the effectiveness of the force estimation in the determination of the stiffness and damping coefficients by comparing them to the known true values. The sensor mounting location is slightly inset within the arms to prevent the rotor from making direct contact with the sensors in the event of user error.

Because the housing is only controllable in the z, α , and β directions, spring-like flexures will restrain the housing from moving in uncontrollable degrees of freedom. These flexures will be attached to the test rig framework. Care must be taken to keep the effect of z stiffness to a minimum because this can severely impact the results of the control force.

One (or more) accelerometers will be mounted to the housing body as indicated by the mounting hole (5).

3.1.3 Bearing

The test subject can be any object that is manufactured to fit in the test rig. The stiffness of these bearings will be within the rage of stiffnesses of the bearings aimed to be identified by the FFBTR. The geometries we choose must be simple in order to conduct an analysis with Finite Element Analysis software, such as ANSYS. They will likely be aluminum or copper hemispheres (shown in Figure 3.5), arches, or rings. The simulation results, as detailed in later sections, analyzes the ability of the rig to identify forces with two different bearing stiffnesses.

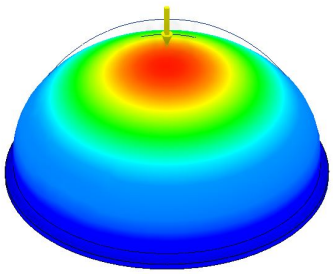

Figure 3.5: Hemispherical test bearing

3.1.4 Framework

The primary purpose of the frame is to contain the horseshoe electromagnets to stabilize the housing platform. These actuators need to be mounted both above and below the housing, and therefore the frame is divided into upper and lower segments that effectively clamshells around the housing flange. These two parts will be bolted together and then secured to the foundation. This setup also allows the gap to precisely adjusted simply by moving the upper platform up or down.

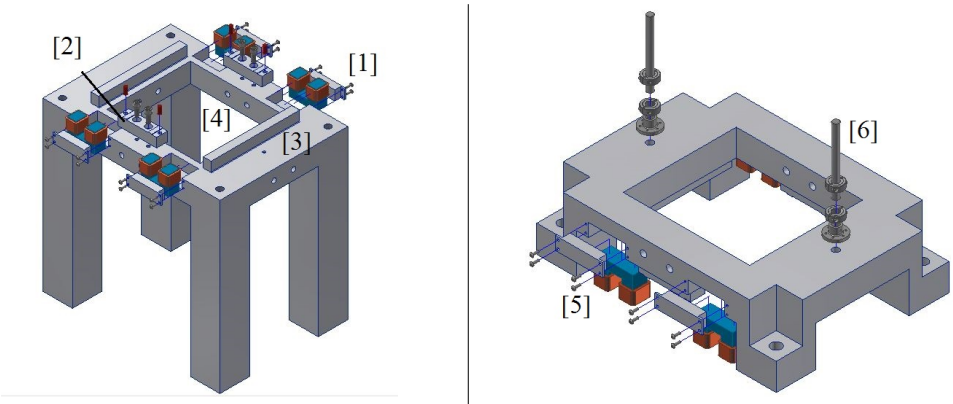

(a) Lower Frame Assembly

(b) Upper Frame Assembly

Figure 3.6: Frame Structure

Lower Platform The lower frame, shown in Figure 3.6a, contains slots where the electromagnetic actuators slide in and then are secured with retention plates from the outside (1). The sensors that provide gap information for the magnetic control loop are also mounted on the lower platform. These are secured in a mounting block, which can then be adjusted by the use of shims (2). The platform is lined with two touchdown bars that are set slightly higher than the actuators to catch the housing before they make contact with the electromagnets or sensors (3). The rig also features sliding flexure extenders that are guided into the lower frame by guide holes (4) and secured from underneath.

Upper Platform The upper frame will also contain slots for magnetic actuators and retention plates (5). It will also feature touchdown bars to prevent the housing from making contact with the upper actuators. The topside of the upper platform has slots and flange mounting locations for the linear guide rails that retain the rotor to one degree of freedom (6).

Note on framework For the purposes of this thesis, the framework and foundation was not fully analyzed. For example, more work needs to be done in regards to the manufacturability of the upper and lower framing platforms, legs, flexures, vertical rails, etc. Once the development of the test rig continues, further work will need to be done to develop a framing support structure. This structure would need to remain stable under a bandwidth of test frequencies. This design provides only a guideline for the construction and execution. More detail in improvements to the structure are covered in section 6.2.

Coordinate Convention A coordinate convention is established for all solid bodies to organize the simulation model and make sure applied forces, torques, and mounting locations are consistent. The coordinate convention of a particular body is defined below.

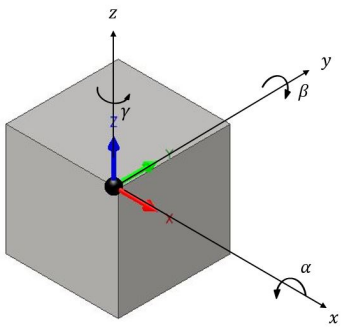

Figure 3.7: Coordinate convention of all solid bodies & transforms

The origin of the part is located at the part's *center of gravity* (CG), indicated in figure 3.7. The mass is aligned with a cartesian plane, and we define six *degrees of freedom* as translation in three perpendicular axes (x, y, and z) and rotation about three axes (α, β, and γ). The arrows indicate the direction which the axis is considered positive (for observing displacements and aligning mounting locations). All masses, unless otherwise indicated, will follow a similar convention.

3.2 Hardware & Sensors

Electrodynamic Shakers The shaker modeled in the physical rig is an MB Dynamics PM-250HP. It has an operating range of 0-1110 N which covers the entire range of test forces required on the dynamic excitation. There are other suppliers of electrodynamic shakers available; this selection was only made as an initial modeling approximation. Due to the mounting configuration of the test rig, another model of shaker can be used; the mounting brackets would simply need to be adjusted up or down using the hex bolts shown in Figure 3.2.

Accelerometers The accelerometer modeled in this system is a PCB Piezoelectronics ICP-353B33. This accelerometer was chosen for its small noise floor and relatively low sensitivity for effective performance of the adaptive open loop controller. This model features one mounting location for the accelerometer, however, a more likely developmental update may feature several accelerometers in multiple locations. Averaging or weighing data from multiple acceleration sources may improve the reliability of the data.

Displacement Sensors The sensors that feed displacement information to be used by the magnetic actuator controllers are modeled as Lion Precision model CPL190 C8S capacitive sensors. These sensors provide high resolution data and have an operational range that is within the anticipated z direction motion of the housing platform.

Other hardware Other hardware including: sensor electronics, amplifiers, and program interface were not included as part of this simulation study. In the next phase of test rig development following the results of this study, these pieces of equipment will need to be specified. See section 6.2 for more details.

3.3 Magnetics

Intro The success of the adaptive open loop algorithm depends on the ability to analyze the housing acceleration to a high degree of accuracy. Any physical connections to the housing structure may add unknown forces or affect the system stiffness. For those reasons, we can levitate the housing structure using a platform of magnetic actuators. This allows us to precisely control the position of the housing and eliminate any external loading factors.

3.3.1 Basics of Electromagnetic Actuation

There are many references that delve into the analysis of electromagnetic systems and magnetism theory. One example is *Magnetic Bearings: Theory, Design & Applications to Rotating Machinery* [18] from which some examples for this paper were taken. For the purpose of this thesis, only an overview of magnetic systems will be covered as it relates to its application in the ALC test rig.

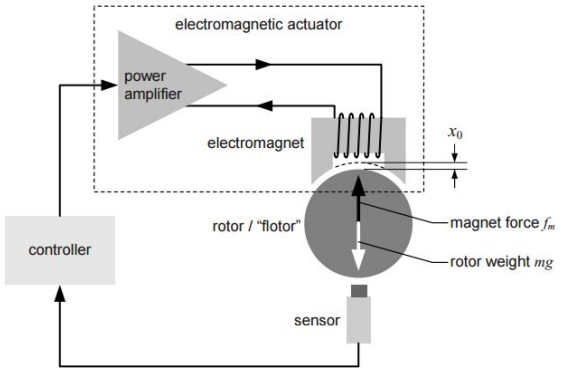

Figure 3.8: Simple magnetic suspension system

Figure 3.8 shows the main components of a simple electromagnetic suspension system. The function of controlling the position of a mass using this setup is as follows:

- The displacement of the mass to be controlled is measured from its "reference position" by use of a displacement sensor.
- A control signal is generated by a processor using the data from the displacement sensor. This signal is transformed to a control current, which is then applied to the windings around the magnetic actuator.
- The electrical current around the core material induces a magnetic field, which attracts the ferromagnetic material (mass). This magnetic force keeps the mass hovering at or near its reference position.

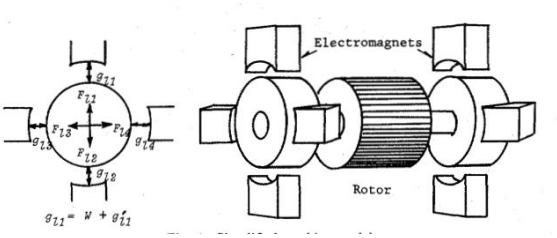

Figure 3.9: Magnetic Bearing suspension system for a rotor

In most cases for a mass that is subject to external forces, two or more magnetic actuators are used to more precisely control the rotor position. This is the case in magnetic bearings, shown in figure 3.9, where the actuators are arrayed around the rotor to provide attractive forces in multiple directions. In this particular test rig, we are only concerned with providing force on the housing in the z direction, so we can use electromagnetic actuators in pairs to provide attractive forces in specific locations on the housing platform. Each set of actuators only needs a single proximity sensor, because the displacement from the reference position for each actuator can be inferred from a single reading.

Our system will feature four sets of actuators for full control in the z, α, and β dimensions. The net force due to any *pair* of actuators will be given by $F_{net} = F_{top} - F_{bottom}$. All system forces will be along the z-axis, so there should be no need to provide control in the translational degrees of freedom, however, the model will include flexures to prevent any runaway movement in the uncontrollable planes.

3.3.2 Magnetic Actuator Design

The force of an actuator as a function of input current is given as follows:

$$F(t) = \frac{\epsilon \mu_0 N^2 A}{4g^2}[i(t)]^2 \tag{3.1}$$

Where:

- ϵ is a correctional coefficient for fringing/leakage
- μ_0 is the permeability of free space
- N is the number of turns of the wire around the actuator
- A is the actuator area
- g is the air gap between the actuator and control body
- $[i(t)]$ is the input current as a function of time.

It is clear from this equation that electromagnetic force is nonlinear and dependent on the gap and input current. However, we can aim to operate the electromagnet primarily in its *linear* range by designing around a desired equilibrium gap, g_0 and current i_0. This constant current input is called the *bias* current, which is independent of time, and instead study the *perturbation* current, $i_p(t)$ which varies to compensate for shifts from the equilibrium position, so $i(t) = i_b + i_p(t)$.

Actuator Sizing The dimensions of the magnetic actuators affect the available force we can achieve from them. At a certain point, a magnetic material reaches *saturation*, meaning additional increases in current will not provide a substantial increase in magnetic flux. This is dependent on the material's *saturation flux density*, or B_{sat}, measured in Tesla. The force at saturation is calculated below:

$$f_{sat} = \frac{B_{sat}^2 A_g}{\mu_0} \tag{3.2}$$

Here A_g represents the total area required for all magnetic actuators. Because the load will be split by all actuators in the system, the required area for each actuator would be $A'_g = A_g/M$ where M is the number of actuators (in our case, four). This assumes the load will be shared equally between them. We can use these details to plan out the necessary sizing of the horseshoe magnets by anticipating what our maximum loading condition on the system will be.

Loading Conditions Analyzing the load to be compensated by the magnetic actuators can be done by observing all loads that will be present in the system. The excitation force (applied directly to the rotor) will be sinusoidal in nature. Static loading conditions include the applied static load from the electrodynamic shaker bias, plus the gravitational force of the solid bodies. That being said, the net force on a single actuator at any point in time can be written by:

$$F_{act}(t) = \frac{(m_r + m_h)g + A_{ex}cos(\omega_{ex}t + \phi_{ex}) + F_{st}}{M} \tag{3.3}$$

This assumes an equal load sharing between all magnetic actuators. The only times this will not be the case is when forces are required to compensate for tilting in the α or β directions, but these perturbations will be very small and can be ignored for the purpose of specifying the actuator size.

The maximum load, when $cos = 1$, then is given by $F_{max} = (m_r+m_h)g+A_{ex}+F_{st}$.

To construct what would be considered the "nominal" magnitude on the system, we find an arithmetic mean of the applied forces and label this as F_{RMS}, or *root mean square* force. RMS of a constant σ is simply its value, and RMS of a sinusoid is $\frac{A}{\sqrt{2}}$. Total RMS for a combined signal is $\sqrt{RMS_1^2 + RMS_2^2 + \cdots RMS_n^2}$.

Here, the RMS load is given by:

$$F_{RMS} = \sqrt{(F_{st})^2 + (\frac{F_{dyn}}{\sqrt{2}})^2} \tag{3.4}$$

Where F_{st} are all static forces (gravity + applied force).

Design Utility The external dimensions of the actuators can be designed to be an appropriate scale with respect to the housing mass. The cross-sectional area, and number of windings, however, can be optimized for F_{max} and F_{RMS}. For additional simplicity, we aim to manufacture all actuators to have the same dimensions and number of windings for ease of interchangeability.

First observe what the minimum cross-sectional area needs to be in order to support the max load, if it were to occur at the point where the magnet reaches saturation. It is generally good practice to design the load capacity well above the maximum expected force so the operation remains primarily in the linear region of the actuator. Apply a safety factor, η, to the minimum area A_g to obtain a corrected value.

$$A_g' = \eta \frac{f_{max}\mu_0}{B_{sat}^2} \tag{3.5}$$

Next we analyze the fact that a pair of actuators, top and bottom, will together need to support an RMS load at F_{net}. For two actuators that have the same geometry & number of windings, the relationship would then be:

$$F_{RMS} = (\frac{\epsilon\mu_0 A_g N^2}{4g_0^2})(i_2^2 - i_1^2) \tag{3.6}$$

Where i_2 is the current into the top actuator and i_1 is the current into the bottom actuator. We can choose a number of windings, N, and observe what the bias currents would be for the top and bottom actuators. A design utility built in Matlab, as shown in Figure 3.10, can easily visualize the effective bias current for a given number of turns. This also allows us to see graphically how far the maximum anticipated load condition occurs from magnetic saturation. As expected, the anticipated bias on the top actuator will always be greater than the bottom because the upwards attractive force must compensate for gravity and downward static loading.

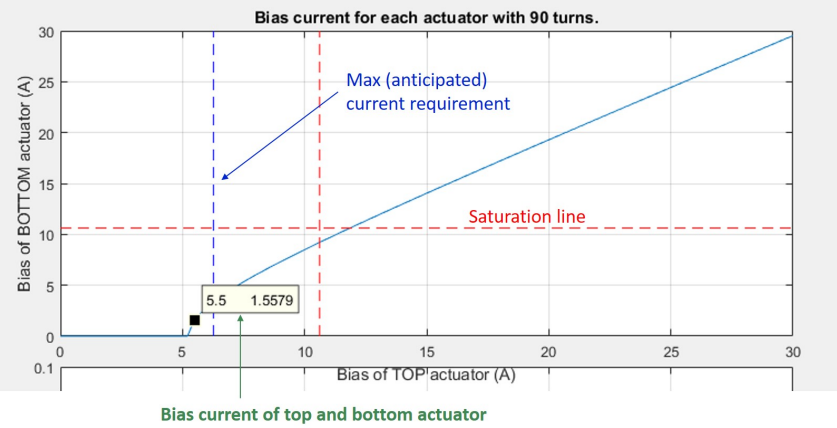

Figure 3.10: Designing a pair of magnetic actuators to be optimized about their respective bias currents

3.4 Ties between physical rig and simulated rig

The next section will go into detail regarding the simulated model for this test rig. Physical parameters from the solid model as outlined above are used to define component mass and transformation matrices. Section 4.6.2 details the error analyses conducted, and measurement errors that are modeled are dependent on hardware specifications in each respective sensors spec sheet, provided in the Appendix.

4 Simulation Model

A full simulation of the Active Load Cell test rig is designed prior to full physical construction in order to analyze the capabilities of the rig in an ideal setting. By using a simulated model, we can not only test the plausibility of the active load cell concept, but also track the position of all physical components in space to gain insight as to the type of motion to expect. This can help us to design the support structure and verify that our selected hardware is appropriate.

In this project, all programming and algorithm development is done using MATLAB script. Matlab m-code can be exported to a control interface (such as LabView) after the physical rig has been built. For a clear schematic as to the interaction of parts and the transfer of data, a model is built using the MATLAB graphical programming environment, *Simulink*. Simulink allows the creation of a block structure of the test rig components and pull in MATLAB script to modify parameters and control the system dynamics. In addition, data can be tracked in real time. Further subsections in this paper describing the simulation will refer to specific capabilities within these utilities.

4.1 Overview

Structure The Simulink model primarily consists of three sub-structures: The rotor subsystem, bearing subsystem, and housing/actuation subsystem. These blocks are connected in a way to represent the physical connections that they represent (See Figure 4.1). All external forces present on the rotor mass are summed and applied as an input to the rotor subsystem. The same goes for the bearing and housing subsystems.

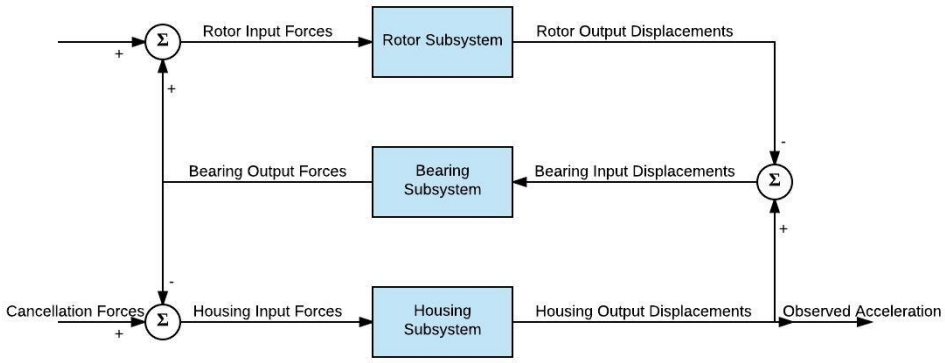

Figure 4.1: Block Diagram of the Active Load Cell Simulation System

From the model overview we can also track the motion of the components and use them for data analysis or algorithm execution. The housing acceleration, for example, can be viewed graphically, and this data is used in the adaptive open loop algorithm to modify the cancellation shaker amplitude and phase. The ultimate goal is to have the housing acceleration converge to zero, or as small as possible so that the error between true bearing force and measured bearing force is very low.

In our Simulink model we have the luxury of observing true bearing force for data validation. This force, however, will not be able to be measured directly in the physical test rig. This parameter is what we are trying to determine experimentally through the cancellation shaker force. For verification of the simulated model, we compare our result signal characteristics with that of the true force being applied.

The next few sections will go into further detail of each subsystem.

4.2 Physical Bodies

General scheme As touched upon in the section above in equation 2.1, the general representation of a 1-DOF spring-mass-damper system where all forces are acting along the same axis would be written

$$m\ddot{x} = F_{ext} - c\dot{x} - kx \tag{4.1}$$

If we were to analyze this system in state-space representation, it would be constructed:

$$\begin{bmatrix} \dot{x}_1 \\ \dot{x}_2 \end{bmatrix} = \begin{bmatrix} 0 & 1 \\ -k/M & -c/M \end{bmatrix} \begin{bmatrix} x_1 \\ x_2 \end{bmatrix} + \begin{bmatrix} 0 \\ 1/M \end{bmatrix} u$$
$$y = \begin{bmatrix} 1 & 0 \end{bmatrix} \begin{bmatrix} x_1 \\ x_2 \end{bmatrix} \tag{4.2}$$

The terms in this equation are scalars, meaning that we are only analyzing the system in one degree of freedom. In order to expand our equations of motion to 6 DOF, we need to establish *matrices* that contain the relevant coefficients in all planes. The position, velocity, and acceleration, then, become *vectors*, broken down into their respective values in each of the six degrees of freedom. For example, the state-space representation of the housing would be given as follows:

$$\begin{bmatrix} \dot{x}_1 \\ \dot{x}_2 \end{bmatrix} = \begin{bmatrix} 0_6 & I_6 \\ -K_H M^{-1} & -C_H M^{-1} \end{bmatrix} \begin{bmatrix} x_1 \\ x_2 \end{bmatrix} + \begin{bmatrix} 0_6 & 0_6 \\ M^{-1} & M^{-1} \end{bmatrix} \begin{bmatrix} u_1 \\ u_2 \end{bmatrix}$$
$$y = \begin{bmatrix} I_6 & 0_6 \end{bmatrix} \begin{bmatrix} x_1 \\ x_2 \end{bmatrix} \tag{4.3}$$

In equation 4.3, x_1 is the [6x1] vector that includes x, y, z (housing CG displacements) and α, β, γ (housing CG rotations). x_2 is the [6x1] vector that includes $\dot{x}$, $\dot{y}$, $\dot{z}$ (housing CG linear velocities) and $\dot{\alpha}$, $\dot{\beta}$, $\dot{\gamma}$ (housing CG angular velocities). u_1 are the input forces and torques due to the magnetic suspension, and u_2 are the input forces and torques due to an external load factor (i.e., cancellation shaker).

4.2.1 Solid Body Subsystems

Rotor Subsystem The motion of the rotor can be described using the general form:

$$M_r \ddot{u}_r = \Sigma F \tag{4.4}$$

Where M represents the *mass matrix* of the rotor and is constructed as follows:

$$M_r = \begin{bmatrix} m_r & 0 & 0 & 0 & 0 & 0 \\ 0 & m_r & 0 & 0 & 0 & 0 \\ 0 & 0 & m_r & 0 & 0 & 0 \\ 0 & 0 & 0 & I_{xx,r} & I_{xy,r} & I_{xz,r} \\ 0 & 0 & 0 & I_{xy,r} & I_{yy,r} & I_{yz,r} \\ 0 & 0 & 0 & I_{xz,r} & I_{yz,r} & I_{zz,r} \end{bmatrix} \tag{4.5}$$

Here, m_r is the rotor mass, in kg. The parameters $I_{xx,r}$, $I_{yy,r}$ & $I_{zz,r}$ etc. represent the planar and cross-plane moments of inertia of the physical body. These can be determined through calculation knowing the structure geometry and material, but thanks to sophisticated software tools like Autodesk Inventor, these parameters can be extracted from a solid model. The acceleration of the rotors *center of gravity* can be represented by the vector $\ddot{u}_r$ and is composed of the following terms:

$$\ddot{u}_r = \begin{bmatrix} \ddot{x}_r & \ddot{y}_r & \ddot{z}_r & \ddot{\alpha}_r & \ddot{\beta}_r & \ddot{\gamma}_r \end{bmatrix}^T \tag{4.6}$$

Where $\ddot{x}$, $\ddot{y}$ and $\ddot{z}$ represent the rotor accelerations in each respective axis (measured in m/s^2). $\ddot{\alpha}$, $\ddot{\beta}$ and $\ddot{\gamma}$ are the angular accelerations in the yz, xz, and xy planes respectively (measured in rad/s^2). This labeling system will be consistent across all bodies and structures in the entire Active Load Cell simulated model. External forces and torques will be transferred to the body's CG because in this simulation all bodies are assumed to be rigid.

The rotor stiffness matrix, K_r, takes the form:

$$K_r = \begin{bmatrix} k_{x,r} & 0 & 0 & 0 & 0 & 0 \\ 0 & k_{y,r} & 0 & 0 & 0 & 0 \\ 0 & 0 & k_{z,r} & 0 & 0 & 0 \\ 0 & 0 & 0 & k_{\alpha,r} & 0 & 0 \\ 0 & 0 & 0 & 0 & k_{\beta,r} & 0 \\ 0 & 0 & 0 & 0 & 0 & k_{\gamma,r} \end{bmatrix} \tag{4.7}$$

Where k_x, k_y & k_z are planar stiffnesses (measured in N/m) and k_α, k_β & k_γ are torsional stiffnesses (measured in Nm/rad). In this test rig setup, all stiffnesses except the z direction are high because the rails completely restrict motion in all other axes.

Similarly, the damping matrix, C_r, is constructed:

$$C_r = \begin{bmatrix} c_{x,r} & 0 & 0 & 0 & 0 & 0 \\ 0 & c_{y,r} & 0 & 0 & 0 & 0 \\ 0 & 0 & c_{z,r} & 0 & 0 & 0 \\ 0 & 0 & 0 & c_{\alpha,r} & 0 & 0 \\ 0 & 0 & 0 & 0 & c_{\beta,r} & 0 \\ 0 & 0 & 0 & 0 & 0 & c_{\gamma,r} \end{bmatrix} \tag{4.8}$$

Where c_x, c_y & c_z are linear damping coefficients (measured in Ns/m) and k_α, k_β & k_γ are torsional damping constants (measured in Nms/rad).

The rotor force is a *vector* consisting of applied forces and moments on the *center of gravity* (CG). $\vec{F}_r = \begin{bmatrix} F_{x,r} & F_{y,r} & F_{z_r} & M_{\alpha,r} & M_{\beta,r} & M_{\gamma,r} \end{bmatrix}^T$. How the moments about the rotor CG are calculated given an offset load are described in a later section.

Rotor acceleration in all degrees of freedom can be determined by:

$$\ddot{u}_r = [M]_r^{-1} \vec{F}_r \tag{4.9}$$

The rotor velocity vector, $\dot{u}_r$, is found by integrating once ($\dot{u}_r = \int \ddot{u}_r$), and position u_r by integrating twice ($u_r = \int \dot{u}_r$).

Bearing Subsystem Bearing force is calculated by the general form:

$$F_b = C_b \dot{u}_b + K_b u_b \tag{4.10}$$

The bearing model is similar to the rotor model, except that we assume the bearing to have negligible mass. In addition, the bearing may have cross-coupled stiffness (k_{xy}, k_{x_z}, k_{yz}) and damping (c_{xy}, c_{xz}, c_{yz}) components that we need to include in the respective matrices. The bearing stiffness and damping matrices are documented in Appendix E.

Housing Subsystem The housing mass, stiffness, and damping matrices are constructed similar to the rotor matrices. These can be found in Appendix E. The stiffness and damping in the z, α, and β directions are zero, because these degrees of freedom are dependent only on the magnetic actuator control. The x, y, and γ stiffness and damping are due to the flexures retaining the housing in these directions.

4.3 Other Equipment

4.3.1 Shakers

Excitation shaker output force vector is as follows:

$$\vec{F}_{exc}(t) = \begin{bmatrix} 0 \\ 0 \\ F_{dyn} + F_{st} \end{bmatrix} \tag{4.11}$$

With $F_{dyn}(t) = A_{exc} \cos(\omega_\tau t + \phi_{exc})$. ω_τ is the test frequency. Force in the x and y directions will be zero in the orientation that the shaker is mounted (it will not provide force in these directions). This [3x1] matrix is transformed to the rotor center of gravity by $\vec{F}_{exc}(t)' = [Q_{exc}]^T \vec{F}_{exc}(t)$. The excitation shaker transformation matrix is

$$[Q_{exc}] = \begin{bmatrix} 1 & 0 & 0 & 0 & \tilde{z}_{exc} & -\tilde{y}_{exc} \\ 0 & 1 & 0 & -\tilde{z}_{exc} & 0 & \tilde{x}_{exc} \\ 0 & 0 & 1 & \tilde{y}_{exc} & -\tilde{x}_{exc} & 0 \end{bmatrix} \tag{4.12}$$

Where $\tilde{x}$, $\tilde{y}$, and $\tilde{z}$ are the x, y, and z coordinates of the shaker mounting location relative to the rotor's CG. The cancellation shaker follows the same convention, but its transform is relative to the *housing* center of gravity since this is where this load will be applied.

$$\vec{F}_{can}(t) = \begin{bmatrix} 0 \\ 0 \\ A_{can}\cos(\omega_\tau t + \phi_{can}) \end{bmatrix} \tag{4.13}$$

And $\vec{F}_{can}(t)' = [Q_{can}]^T \vec{F}_{can}(t)$.

4.4 Magnetic Support System

4.4.1 Magnetic Actuation Hardware

Electromagnets can only provide force on a ferromagnetic material, and as such the housing mass will need to be fitted with iron inserts where the magnetic actuators can align. As seen in image 3.4a, a flange on the housing allows for the attachment of silicon iron plates. In order to simulate the control of the housing due to electromagnets, we first need to develop a transformation scheme to relate the actuator sensors and actuators back to the housing center of gravity.

As seen in image 4.2, each set of actuators will have an central actuated location - this is the location where each actuator is providing force on the housing mass. Sensors will be located near their respective actuators, but will have their own locations.

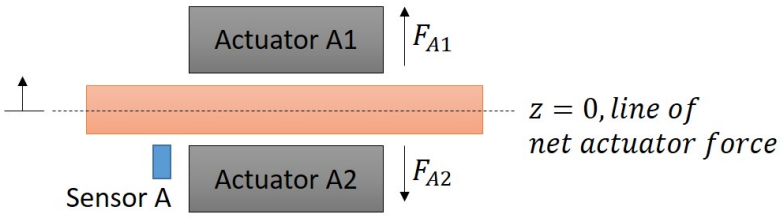

Figure 4.2: Line of actuator net force

Displacements in each dimension will be regarded as the displacement of the housing CG in that dimension, plus the effect of housing tilt in the relative axis. Since all rotations θ are assumed to be very small, we can linearize the effect of a rotation in a plane such that $d \sin\theta \approx d\theta$. We also assume all rotations to be decoupled, that is, for example, a small rotation about the α axis can be observed independently from a simultaneous rotation about β. See figure 4.3.

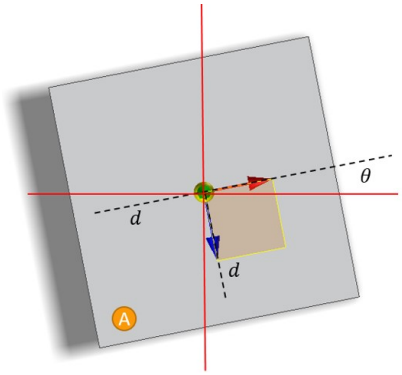

Figure 4.3: Tilt of housing, θ degrees in γ axis

Sensor transforms Given the convention shown in figure 4.4, the displacement at the given sensor S_A is found by using the coordinate transform:

$$\vec{u}_{SA} = [Q_{SA}]\vec{u}_h \tag{4.14}$$

Where $\vec{u}_{SA}$ is the sensor position vector $\begin{Bmatrix} x_{SA} & y_{SA} & z_{SA} \end{Bmatrix}^T$, $\vec{u}_h$ is the housing CG translate/tilt vector, and the transform matrix $[Q_{SA}]$ is given by:

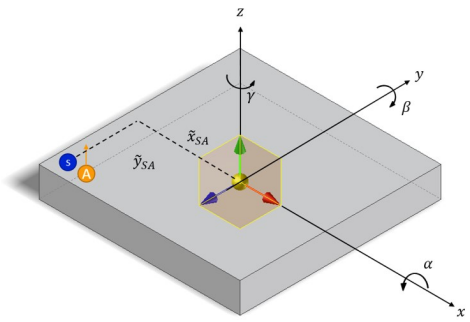

Figure 4.4: Coordinate Convention of Sensor location

$$[Q_{SA}] = \begin{bmatrix} 1 & 0 & 0 & 0 & \tilde{z}_{SA} & -\tilde{y}_{SA} \\ 0 & 1 & 0 & -\tilde{z}_{SA} & 0 & \tilde{x}_{SA} \\ 0 & 0 & 1 & \tilde{y}_{SA} & -\tilde{x}_{SA} & 0 \end{bmatrix} \tag{4.15}$$

Each sensor (A, B, C, D) will have its own $[Q]$ matrix that follows the same convention. Because all sensors will be affected by the housing position and angle, combine all four matrices into a larger one for the sake of only executing one transformation, where:

$$\vec{u}_S = [Q_S]\vec{u}_h \quad \text{with} \quad [Q_S] = \begin{bmatrix} Q_{SA} & Q_{SB} & Q_{SC} & Q_{SD} \end{bmatrix}^T \tag{4.16}$$

The vector u_S provides the x, y, and z location of all four sensors in the system.

Actuator transforms Transforming to the magnetic actuator locations is done in the same way as the sensor locations. In this case, the x, y, and z positions of a particular actuator set refer to the centerpoint of the actuator set, because this the location where the actuator force will be analyzed from a point-load perspective.

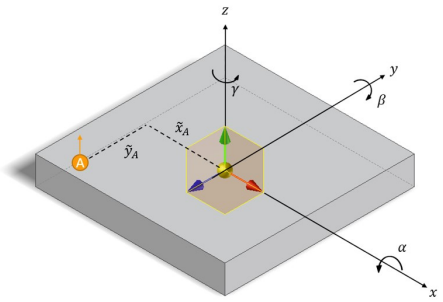

Figure 4.5: Coordinate Convention of Actuator location

The displacement of actuator A is given by $\vec{u}_A = \begin{Bmatrix} x_A & y_A & z_A \end{Bmatrix}^T = [Q_A]\vec{u}_h$ with

$$[Q_A] = \begin{bmatrix} 1 & 0 & 0 & 0 & \tilde{z}_A & -\tilde{y}_A \\ 0 & 1 & 0 & -\tilde{z}_A & 0 & \tilde{x}_A \\ 0 & 0 & 1 & \tilde{y}_A & -\tilde{x}_A & 0 \end{bmatrix} \tag{4.17}$$

And similarly to the sensor system, we construct a generic transform for all actuators such that

$$\vec{u}_A = [Q_{AC}]\vec{u}_h \quad \text{with} \quad [Q_{AC}] = \begin{bmatrix} Q_A & Q_B & Q_C & Q_D \end{bmatrix}^T \tag{4.18}$$

Called the actuator transform matrix, $[Q_{AC}]$.

4.4.2 Actuator Analysis in F.E.M.M.

Introduction A sophisticated magnetic model will provide a more accurate representation of magnetic forces than a linearized model alone. In particular, the reason why we need a robust actuator model is due to the variability in the load applied on the system. Linearizing around a single bias is not sufficient because under different loading conditions, the effective bias will shift up or down, potentially straying far from the linear range of a particular actuator and potentially approach saturation. We need to be able to create a magnetic model that takes all nonlinear effects into consideration, and test it under a variety of load cases to validate its effectiveness in the test rig design.

Rather than try to tackle the complexities of a magnetic system computationally, we can employ a software tool called *Finite Element Method Magnetics*, or F.E.M.M. [19]. FEMM is a Windows finite element solver for 2D and axisymmetric magnetic, electrostatic, heat flow, and current flow problems with graphical pre- and post-processors [20].

This software uses finite element analysis to solve magnetostatic problems, and can take many factors into consideration when solving magnetics problem such as flux paths, hysteresis effects, and magnetic losses. Full documentation on the operation of F.E.M.M. can be found in reference [19].

Preprocessing After the actuator dimensional parameters are chosen, we can import the dimensions into FEMM and build a 2D representation of a single actuator/flotor system. Using the FEMM tools we can assign a material to each solid body, and provide a virtual circuit of windings in a location around the actuator to match our analysis done in part 3.3.2. Before analysis, we implement an *improvised open boundary* condition around the actuator. The open boundary is emulated by placing thin layers of isotropic material at the outer extents of the domain. By careful selection of the magnetic permeability of the layers, asymptotic boundary conditions (ABCs) are produced. This method allows for accurate open-boundary solutions with nearby boundaries [21].

A current is set to be applied through the simulated windings. FEMM then builds a mesh of the solid and runs an analysis as shown in figure 4.6.

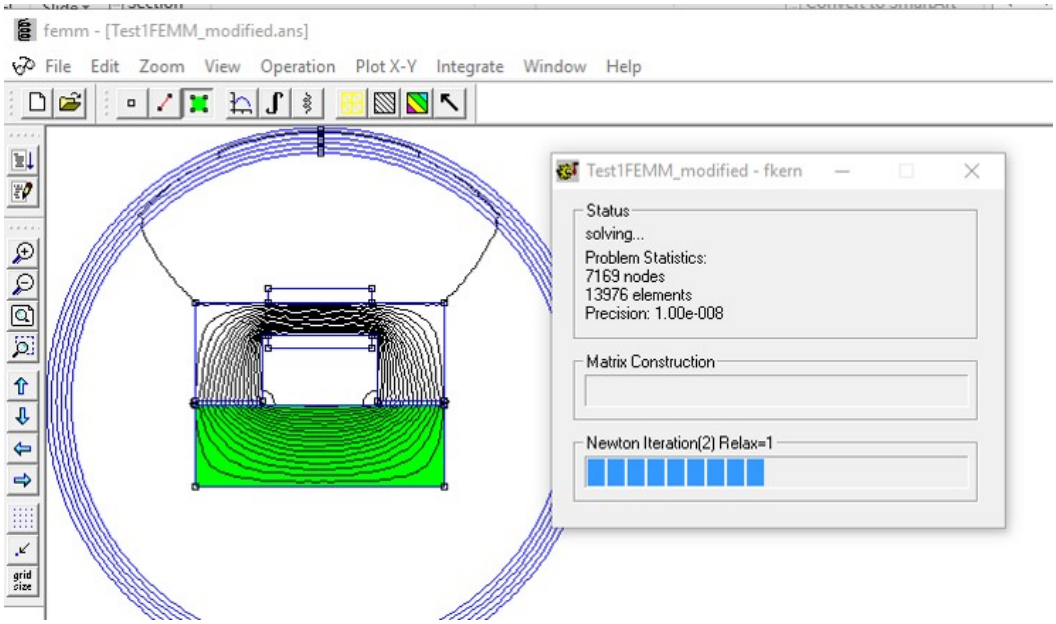

Figure 4.6: Screenshot of the FEMM solver running an analysis

Postprocessing After analysis is complete, we can observe the force on the 'flotor' mass via a volume integral. The program computes the weighting function by solving an additional Laplace equation over the air surrounding the blocks upon which the force is to be computed. The stress tensor is then evaluated as a volume integration, and the results are displayed [22].

This process is iterated through all combinations of gap distances and currents within the range that was set. We use this information to build a 2-dimensional table, which we can access with a function by inputting gap and current and outputting actuator force. A 3-dimensional visualization of the relationship between gap, current, and actuator force are shown in figure 4.7.

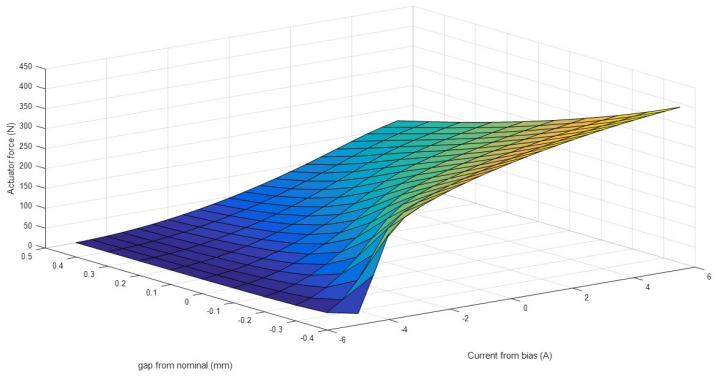

Figure 4.7: 3D contour plot of lookup table data

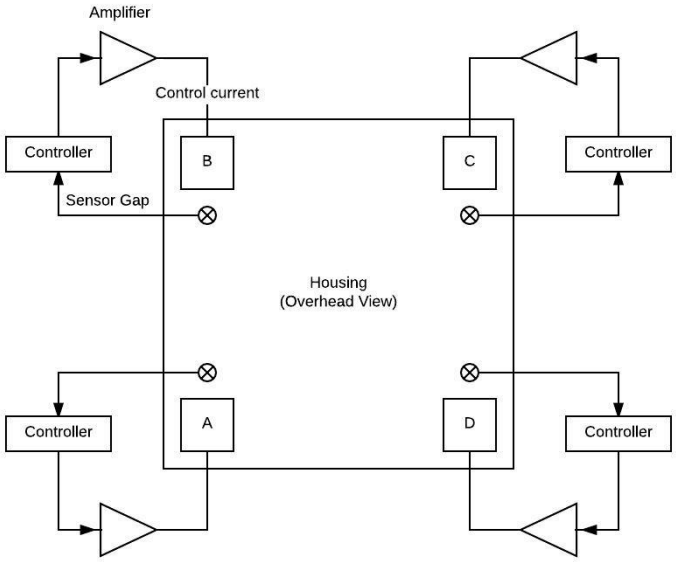

Figure 4.8: Control scheme of the housing platform with four independent actuators

4.4.3 Magnetic Control

Control of the magnetic actuators is achieved through a classical feedback control scheme. Each of the four sets of actuators in either corner of the housing mass are controlled independently, and as such, have their own sensors and amplifiers, as shown in Figure 4.8. The current into the upper and lower actuator on any particular set are dictated by a single sensor and controller. The sensor, situated on the underside of the housing platform, measures the gap and compares this value to a reference (see Figure 4.9). The PID controller processes a control *voltage*, which relates directly to a perturbation current around the pre-selected bias. A very basic amplifier is modeled in this study that restricts the control current at a 10,000 Hz sample rate, however, further work will feature a realistic amplifier model transfer function.

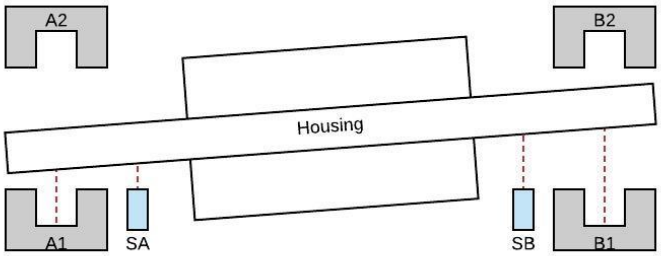

Figure 4.9: Gap values at both the displacement sensors and magnetic actuators. The housing tilt angle and gap values are exaggerated for easier understanding.

The control output represents the physical current i flowing through the electromagnet's coil [18]. It is at this point where the lookup table takes place of the nonlinear magnetic model, by taking in inputs of current i and measured gap x to produce a force f. The gap value fed into the nonlinear model is the true gap at the actuator location rather than the sensor gap, because this scheme leads to more accurate force interpretation.

PID control of Actuators *Proportional-Integral-Derivative* (PID) controllers a are simple and robust method for controlling an electromagnetic actuator. PID control is used to stabilize the plant (in this case, the housing mass). Tuning the PID parameters is done manually within Simulink. A static load is applied on the system to observe the response over time. Next we adjust the relevant PID parameters to get a response that is reasonably fast, doesn't allow for excessive deflection in the z direction (otherwise the housing plate risks 'bottoming out', and has very low steady-state error to aid in adaptive open loop algorithm convergence, as shown in Figure 4.10. The parameters were chosen using the sequence in the list below. PID control blocks within Simulink also feature built-in lowpass filters on the derivative term in order to prevent the amplification of measurement noise. In our case the filter sampling frequency is set to 10,000 Hz.

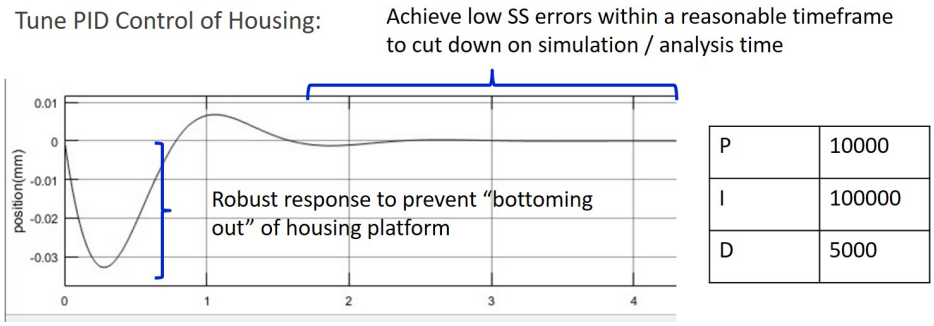

Figure 4.10: Response of housing under a step load after PID tuning

PID Tuning Procedure:

1. Set all gains to zero.

2. Increase P gain until oscillations are steady.

3. Increase D gain until the system is critically damped.

4. Repeat the above two steps until further increases in D gain do not significantly reduce oscillations.

5. Increase I gain until steady-state response is appropriate.

Bandstop Filter It is necessary to prevent the magnetic actuators from producing any forces at the test frequency, because forces that are compensated within the magnetic structure will affect the cancellation force. To achieve this, we pass the control current through a *band stop* or *notch* filter. This passes most frequencies through un-altered, but attenuates frequencies over a certain range to very low levels.

The transfer function of a bandstop filter is shown below:

$$H(s) = \frac{s^2 + (2\varepsilon\omega_n)s + \omega_n^2}{s^2 + (2\zeta\omega_n)s + \omega_n^2} \tag{4.19}$$

Where:

- ω_n is the test frequency, in rad/s
- ε and ζ are parameters that affect the width and depth of the filter notch

Creating a bode plot of this transfer function, as in Figure 4.11 allows easy visualization of the effects of the notch filter. For example, increasing the ζ value increases the notch width, but also affects the phase shift of system frequencies, particularly those close to the test frequency. The ε parameter changes the notch depth, that is, the maximum negative gain at the test frequency. We can alter this parameter to get a filter that applies an effective amount of attenuation without overtaxing the control system. The parameters selected (shown in Figure 4.11) offer an acceptable level of frequency attenuation. Initial application of the bandstop filter will prevent control of the housing platform at the test frequency, however, the cancellation shaker will compensate for this once the adaptive open loop algorithm is implemented.

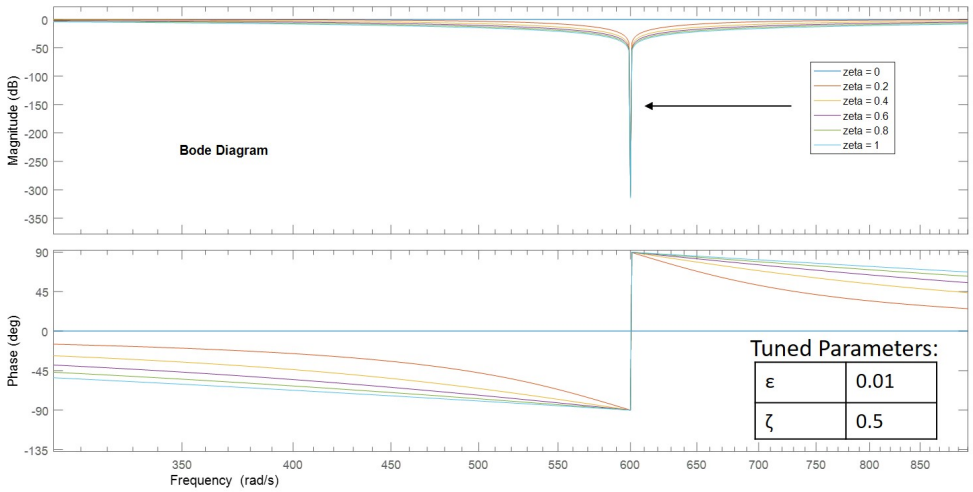

Figure 4.11: Bode Plot of various filter gains

4.4.4 Simulink Integration

Actuator data and operation is simulated in Simulink through the following process:

1. Displacement at each sensor is calculated using the transform in equation 4.16.
2. Sensor x, y, and z positions are compared to their nominal position (zero vector)
3. Sensor z-offset is fed through a PID controller (see below) to determine an appropriate actuator voltage. Sensor offset in x and y dimensions are discarded because the system is uncontrollable in these directions.
4. Voltage is converted to a control current through a magnetic amplifier model.
5. Current is passed through a bandstop filter (see below) to filter out any signals that would be applied at the test frequency.
6. Displacement at each associated actuator is calculated using the transforms in equation 4.18.

7. Actuator displacement and current are both passed through a *duplicator* matrix. Because two actuators are controlled with a single displacement sensor, equate a negative displacement in the z-direction for the bottom actuator with an equivalent positive displacement on the top actuator. See Figure 4.9.

8. Current values are passed through a saturation curve to represent the total current an amplifier can realistically provide.

9. Corrected gap and current values are fed into a 3-dimensional lookup table where the previously determined magnetic force data lies. Gap or current values not aligning to a table entry will be linearly interpolated between adjacent entries. The relevant actuator force is output.

10. Net force for a pair of actuators is calculated.

11. Forces for all four actuators are applied to the housing at their locations using the transform $[Q_{AC}]$.

4.5 Adaptive open-Loop control

Introduction The primary objective of the Active Load Cell test rig relies on being able to counter the effects of the dynamic excitation and provide a cancellation force such that the acceleration of the housing approaches zero. Achieving stability under a dynamic loading condition can be achieved via *closed-loop* control, similar to the scheme employed by the magnetic actuators, or by *open-loop* control, which superimposed on top of the already existing feedback control forces. Developing a closed-loop control system would involve altering the magnetic actuator controller to produce appropriate responses to dynamic excitation. This would entail implementing a more sophisticated control algorithm than the PID currently in place, plus the addition of filters to remove the synchronous vibration. In addition, closed-loop systems can adversely affect the stability of the system through feedback [23].

An open-loop scheme superimposes the cancellation forces on top of the already existing magnetic stabilization forces. This force can be altered as the characteristics (frequency, amplitude, phase) of the dynamic force is altered without any changes to the magnetic actuator feedback controller. In order to make this additional controller effective in this test, an iterative method is used to adapt the open-loop forces to reach a predetermined performance - in our case, minimized acceleration. The result is a *forced* response so it does not affect system stability. To be sure that the control force selected produces the optimal vibration reduction, the force is updated based on the performance of the previous force iteration. This type of control is referred to as *adaptive open-loop control* [23].

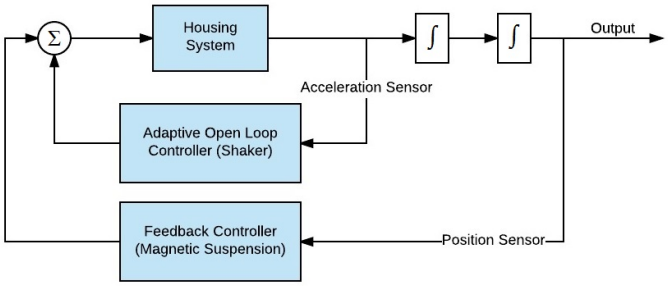

Figure 4.12: Block diagram of system with the addition of adaptive open loop controller

4.5.1 Theory

In this control scheme, a set of control signals, $u(t)$, are applied to a system in order to affect its response. As shown in figure 4.12, open-loop signals are superimposed on top of the existing feedback signals from the magnetic actuators. The control signals are pre-calculated, meaning that knowledge of the system dynamics is required before it can be implemented. To determine the amplitude and phase of open-loop control signals, it is necessary to estimate a system influence coefficient matrix, $[T]$, which relates the system response at a frequency due to open-loop control signals at the same frequency [24].

This type of control has been well documented by R.W. Hope and C.R. Knospe (1994) [25] with more experimental results reported in Knospe *et al.* (1995) [26]. This methodology will be discussed in terms of its application to this research project.

A forced response of a system is given by:

$$x = \mathbf{T}u + x_0 \tag{4.20}$$

Where x is the [2nx1] vector of synchronous Fourier coefficients of vibration at n position sensor locations, and u is the [2mx1] vector of synchronous Fourier coefficient of open-loop forces applied through m axes. In our case, we are using a single piece of dynamic actuation equipment (electrodynamic shaker) and monitoring the acceleration in one axis (z) so n and m are both 1, making x and u both [2x1] vectors. $\boldsymbol{T}$ is the [2x2] matrix of influence coefficients that relate the open-loop forces to the synchronous vibrations. x_0 is the [2x1] vector synchronous Fourier coefficients of uncontrolled vibration.

If open-loop forces are applied in an iterative fashion, vibration at some iteration k will be given as follows:

$$x_k = \boldsymbol{T}u_k + x_0 \tag{4.21}$$

If $\boldsymbol{T}$ and x_0 remain constant and subtracting iteration k from iteration $(k+1)$ we arrive at

$$(x_{k+1} - x_k) = \boldsymbol{T}(u_{k+1} - u_k) \tag{4.22}$$

$$\Delta x = \boldsymbol{T}\Delta u \tag{4.23}$$

Due to the complex system dynamics, this influence coefficient matrix $\boldsymbol{T}$ is not known exactly, so we need a way to estimate this matrix through experimentation. We can apply a series of p synchronous open loop test signals and record the resulting vibration. The number of test forces must be greater than or equal to $2m+1$ in order to fully determine the solution [25]. The test forces and subsequent vibrations are compiled into batch matrices:

$$\Delta U = \begin{bmatrix} u_1 - u_2 & u_2 - u3 & \dots & u_{p-1} - u_p \end{bmatrix} \tag{4.24}$$

and

$$\Delta X = \begin{bmatrix} x_1 - x_2 & x_2 - x3 & \dots & x_{p-1} - x_p \end{bmatrix} \tag{4.25}$$

As above, these matrices can be placed together such that

$$\Delta X = \hat{\boldsymbol{T}} \Delta U \tag{4.26}$$

Where $\hat{\boldsymbol{T}}$ is an estimator of $\boldsymbol{T}$. Solving for $\hat{\boldsymbol{T}}$ we can construct

$$\hat{\boldsymbol{T}} = \Delta X (\Delta U)^T [\Delta U (\Delta U)^T]^{-1} \tag{4.27}$$

based on a least squares linear regression model.

The aim is to develop a control law that will reduce x, the synchronous system vibration. If a performance measure is to be taken such that:

$$\boldsymbol{J} = x^T \boldsymbol{W} x \tag{4.28}$$

Where $\boldsymbol{W}$ is a weighing factor, or adaptation parameter. As outlined in *Hope, 1994* [25], a control law for synchronous vibration control is given by:

$$u_{i+1} = u_i - (\boldsymbol{T}^T \boldsymbol{W} \boldsymbol{T})^{-1} \boldsymbol{W} \boldsymbol{T}^T x_i \tag{4.29}$$

Here, u_{i+1} represents the next iterated control force to apply after the control u_i and respective vibration response x_i are measured. When $m = n$ the performance measure $\boldsymbol{J}$ will converge to zero, or as small as can be achieved within the noise floor of the vibration sensor (accelerometer). A simplified control scheme, where the weighing factor $\boldsymbol{W}$ is a [2x2] identity matrix (indicating 100% adherence to the least squares linear regression) is given as in equation 4.30. During testing, this weighing factor is reduced in order to observe a slower adaptive open-loop convergence.

$$u_{i+1} = u_i - \boldsymbol{T}^{-1} x_i \tag{4.30}$$

The control law in equation 4.30 is used in the execution of the algorithm as detailed in the selection below.

4.5.2 Implementation

The implementation of the adaptive open-loop control algorithm in this particular application follows the sequence below.

1. Run simulation under a dynamic excitation load but with no input to the cancellation shaker and observe the resulting acceleration.

2. Determine the amplitude and phase of the acceleration using a fourier transform (obtain x_0).

3. Define a batch of arbitrary control inputs, u_i(cancellation shaker forces). Run the simulation at each input and observe the resulting acceleration, x_i.

4. Calculate the influence coefficient matrix, $\boldsymbol{T}$ using $\Delta X/\Delta U$.

5. Define the first adaptive input into the cancellation shaker using $u_{i+1} = -\boldsymbol{T}^{-1}x_i$

6. Observe the resulting acceleration, x_{i+1} and repeat the iterative process until the value has converged to zero (or as small as can be measured).

In some instances, especially in the presence of errors, the algorithm may fail to correctly identify the influence matrix, leading to the possibility of amplified accelerations. If accelerations become large, the algorithm attempts to re-identify the influence matrix using a different series of test inputs. If the convergence still fails, the controller will throw an exception that the system could not be identified.

The controller is designed to wait an adequate amount of time after the magnetic platform has had an opportunity to stabilize from the addition of static and dynamic forces. The transient activity during start-up may lead to an incorrect identification as well. Typically lower test frequencies require a longer time to stabilize. Generally 3-4 iterations will eliminate over 90% of vibration, with additional iterations providing decrementing improvements, as shown in Figure 4.13, which was run at a test frequency of 100 Hz.

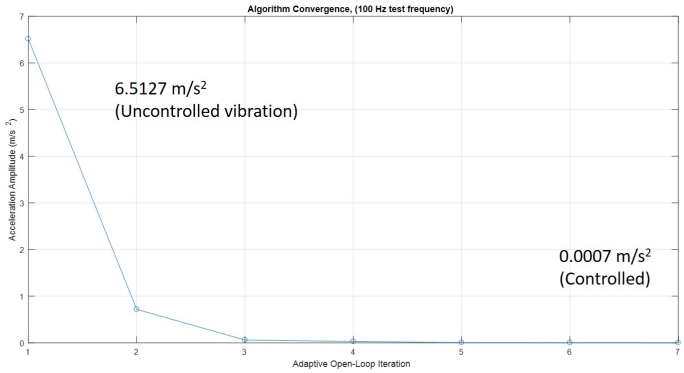

Figure 4.13: Convergence of Adaptive Open Loop Controller for one Test Case

4.6 Running test cases

4.6.1 Force adjustment

Varying system gains Due to variations in system gain when excited at different frequencies, the system response may result in an unacceptably high amount of relative movement between components. On the other hand, too small of a dynamic excitation may not elicit significant enough results to appropriately run an optimization algorithm. It is useful to adjust the excitation parameters on the system in order to target a relative amount of motion that would make sense for this type of machine. Additionally, by assuring that there is a common and expected relative component displacement, we can more confidently select a sensor that can handle this range, and adjust the sensor position appropriately.

The aim is to alter the dynamic force on the system depending on the test frequency being applied. To achieve this, a bisecting algorithm is used to adjust dynamic shaker force and measure the resulting rotor-housing displacement until the target displacement is achieved. The output of this process is a Force-Frequency relationship curve, which will be used in our test cases to be sure the applied load is appropriate for the given frequency.

The anticipated relative displacement between components on the FFBTR is expected to be on the order of 1/10 mil (0.002 mm). For the purposes of this test rig, our target threshold is 0.005 mm, a more relaxed requirement.

Figure 4.14a shows one particular system's relative displacement at a dynamic load of 400 N for a range of test frequencies. Figure 4.14b shows what the compensated dynamic forcing function looks like after the algorithm has been run. All resultant displacements are within 1% error of the target. The results section of this paper also includes the compensated force table for each of the bearing stiffnesses being tested. As one would expect, generally the compensated forces for the bearing with higher stiffness are larger, due to less relative movement between components.

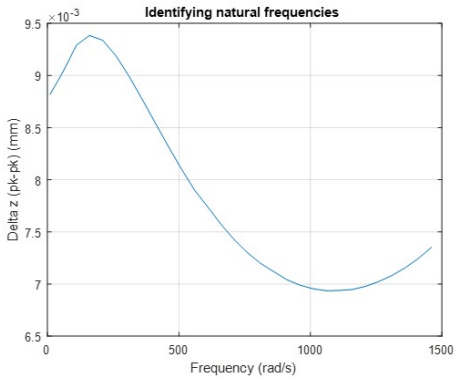

(a) Relative displacement between rotor and housing at a consistent load of 400 N

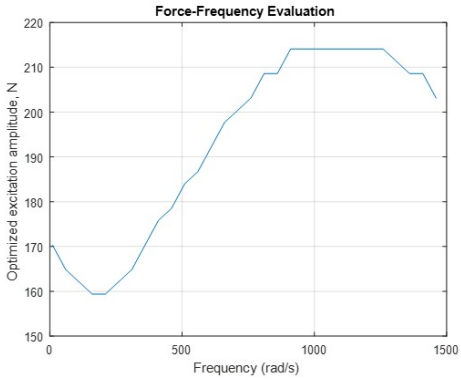

(b) Compensated Force in order to achieve a target relative displacement

As part of the experimental results, however, consistent dynamic loads across all test frequencies are also tested. The purpose for this is to evaluate whether the magnitude of the dynamic load has an effect on the capability of the rig to identify forces accurately.

4.6.2 Monte Carlo analysis

The first iteration of the simulation model featured a direct link between all sensors and their controllers. In other words, there are no inconsistencies, noise, or sources of error that would serve to make the simulation any less than ideal. Perhaps unsurprisingly, initial testing showed an ability of the rig to identify force to an incredible accuracy - in most cases within 0.001% of truth. Analyzing the best-case scenario is useful for initial proof of concept, but in order to truly analyze the capabilities of the test rig, it is necessary to identify sources of measurement error and observe their effect on the results. In reality, error can originate from a large variety of sources, such as calibration of equipment, manufacturing tolerances, electronic hardware delays, etc.

To make a prediction as to the consistency of ALC test rig outputs, we conduct a *Monte Carlo* analysis. In its broadest sense, Monte Carlo simulation can be defined by: modeling a system as a series of probability density functions (PDF), repeatedly sample from the PDFs, and tally/compute the statistics of interest [27]. In this thesis, a simple analysis was conducted in order to form a statistical distribution of expected errors, and potentially identify those errors which cause a failure of accurate identification.

Sources of Measurement Error For the purposes of this thesis, the sources of error to be analyzed were directly related to the sensor readings. This best represents the types of errors that would be present in the actual system. In reality, this list is not exhaustive; however, it doe represent some of the most significant expected error sources. The sources of error that were included in this study are tabulated in Table 2.

Error Source	Nom. Val.	Error Range
Magnetic Sensor Errors (x4)		
Sensor Gain [1]	1.0	[0.997 1.003]
Sensor Offset [2]	0.0 mm	[-0.1 +0.1] mm
Sensor Tilt [2] (α & β)	0 deg	[-3.0 +3.0] deg
Actuator Location Errors (x4)		
Actuator Offset [2]	0.0 mm	[-0.1 +0.1] mm
Accelerometer Errors		
Sensor Gain [1]	1.0	[0.95 1.05]
Sensor Phase	0.0 deg	[0.0 2.0] deg
Sensor Noise [1]	0.0 m/s^2 (RMS)	[0.005] m/s^2 (RMS)
Sensor Cross-talk [1] (X & Y)	0.0 %	[-5.0 +5.0] %
Sensor Tilt [2] (α & β)	0 deg	[-3.0 +3.0] deg

Table 2: Monte Carlo Parameters

For this study, errors within their respective ranges are randomized and applied to the model. This is repeated 250 times for each test case. Using the results of these parametric runs, it is possible to observe the statistical distributions of the final force amplitude and phase errors to develop confidence intervals.

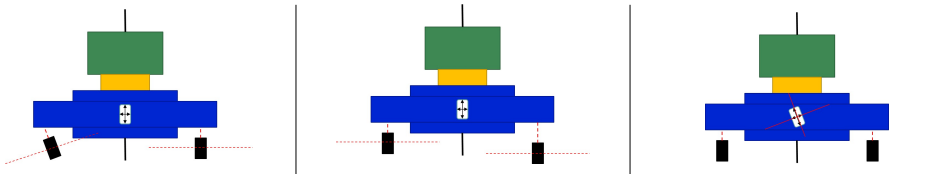

(a) Sensor Tilt (b) Sensor Offset (c) Accelerometer Tilt

Figure 4.15: Visualization of some Error Sources

[1]Based on Spec Sheet

[2]Based on anticipated manufacturing capabilities

5 Simulation Results

5.1 Test Case Setup

The simulation model was tested to verify convergence of the adaptive open loop controller and to establish anticipated errors. Moving forward with the Fluid-Film Bearing Test Rig, further studies can be done knowing the confidence bounds that are achievable on bearing force measurements.

5.1.1 Bearing Stiffness Matching

The stiffness range of bearings to be identified by the FFBTR is roughly 400,000 - 2,000,000 lbf/in (7.0E7 - 3.5E8 N/m). We want to choose two bearing test stiffnesses towards either end of this range to see how the ALCTR handles each scenario. Due to different equipment masses (between the ALCTR and FFBTR) we need a way of establishing an equivalent stiffness range for this rig. In the most simple sense, we can analyze the natural frequency of the two-mass system joined by a spring for an approximation. The natural frequency of a this system can be determined by equation 5.1.

$$k(m_1 + m_2) = (m_1 m_2)\omega_n^2 \tag{5.1}$$

For the lower and upper stiffness range we analyze the natural system frequency, match this to our ALC model, and determine an equivalent stiffness to give the system the same natural frequency. As displayed in Table 4, The equivalent ALC stiffness range is approximately 2.7E7 - 1.3E8 N/m (154,000 - 742,000 lbf/in). There are two test "bearings," one at a low and one at a high stiffness, to observe the identification capabilities at either end of this range. The 'soft' bearing studied will have a stiffness of **3.0E7 N/m** and the 'stiff' bearing will have a stiffness of **1.0E8 N/m**.

Mass	FFBTR	ALCTR
m_1	60 kg	22.319 kg
m_2	50 kg	20.870 kg

Table 3: Masses of FFBTR and ALCTR

Stiffness (FFBTR)		ω_n	Eq. Stiffness (ALCTR)
Low	7.0E7 N/m	1602 rad/s	**2.7E7 N/m**
High	3.5E8 N/m	3582 rad/s	**1.3E8 N/m**

Table 4: Equivalent ALCTR Stiffnesses

5.1.2 Frequencies & Force Amplitudes

Test Frequency For consistency, all trials were run at each of the frequencies indicated in table 5. These frequencies are within the range of test frequencies expected to be operated on the fluid film bearing test rig. They were chosen based on a logarithmic scale to span two decades.

(rad/s)	**(Hz)**	**(rad/s)**	**(Hz)**
120	19.09	1280	203.71
205	32.62	1800	286.47
300	47.74	2340	372.42
440	70.02	2750	437.67
650	103.45		

Table 5: Test Frequencies

Dynamic Force Amplitude All frequencies are run through the Monte Carlo Analysis in three trials:

- *Compensated* Force, which is the adjusted dynamic load for the particular test frequency as described in section 4.
- *Moderate* Force, which is a constant value of **350 N** across all frequencies. This value is approximately 60% of the static system load.
- *Low* Force, which is a constant value of **50 N** across all frequencies. This value is approximately 8% of the static system load.

5.1.3 Test Sequence

Test cases are run in the following sequence:

1. For the given test frequency and dynamic force amplitude, run the model with no errors present and observe the housing motion. This is a visual check to make sure the displacement caused by the dynamic force doesn't threaten to "bottom out" against the touchdown flanges, and that all transient motion has died down in the allotted timeframe. Additionally, observe the current requirements of the electromagnetic actuators to make sure they are appropriate (are not approaching saturation). Figure 5.1 shows the uncontrolled housing motion, in the z-direction at a test case of 628 rad/s & 410 N dynamic load.
2. Apply the adaptive open loop controller with no errors present to be sure the identification process is working correctly. Observe the controlled housing response, as shown in Figure 5.2 for the same test conditions.
3. Once the model has been verified, run the Monte Carlo studies by varying the error sources and running the simulation for 250 iterations. The following restraints are used:
    - Adaptive open-loop controller will make two attempts to identify the influence matrix (T). If acceleration is diverging after this, the simulation aborts and throws a "failure to identify" exception.

- Algorithm is run until acceleration converges to the noise floor, or reaches 7 iterations, whichever happens first.
- Cancellation force amplitude and phase are reported along with their respective errors from analyzing true bearing force/phase.

4. Build a statistical distribution of the Monte Carlo studies to develop anticipated errors and confidence limits.

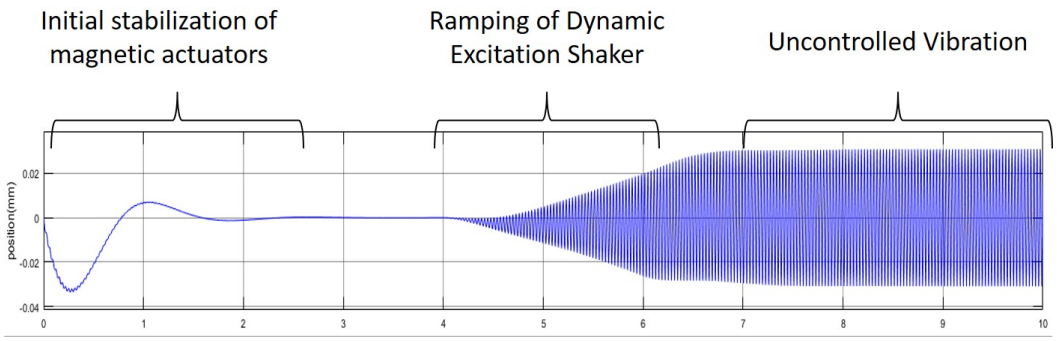

Figure 5.1: Uncontrolled Housing motion, 628 rad/s

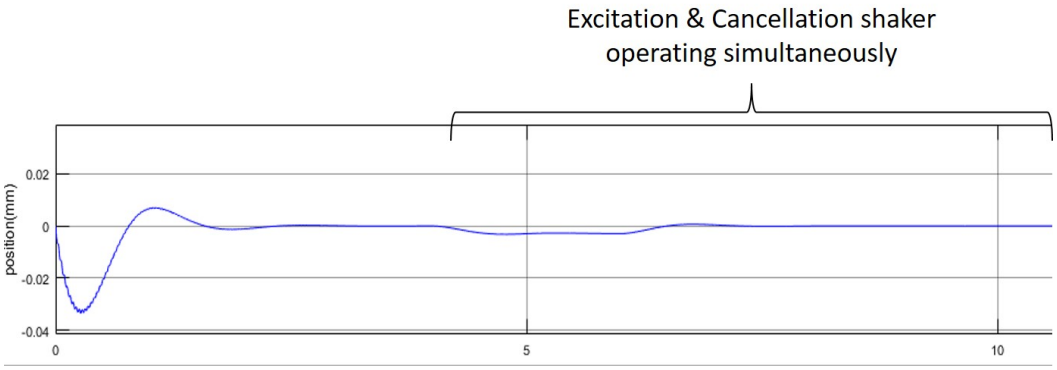

Figure 5.2: Controlled Housing motion, 628 rad/s

One example of the controller stabilizing the housing and identifying bearing force in the presence of errors is shown in Figure 5.3.

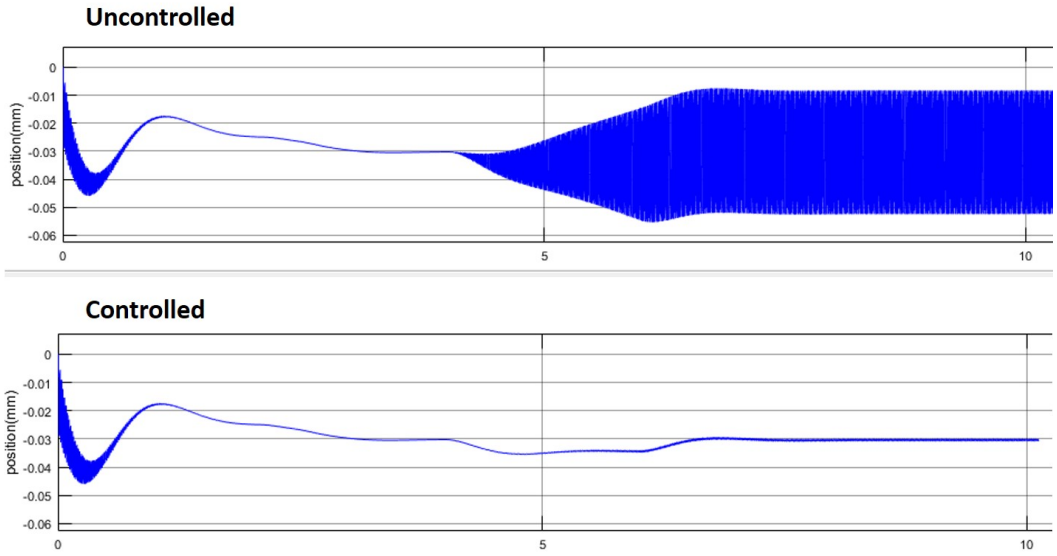

Figure 5.3: Uncontrolled and Controlled housing motion in the presence of errors

5.2 Test Case 1: Low Stiffness Bearing

5.2.1 Test Parameters

This bearing was modeled with the following parameters:

- Z-Direction Stiffness: 30,000,000 N/m (171,000 lbf/in)
- Z-Direction Damping: 1500 Ns/m (8.5 lbfs/in)

5.2.2 Tabular Results

Simulation Convergence As mentioned above, if the adaptive open loop controller fails to identify the influence matrix correctly, acceleration will typically diverge rather than converge. If this happens, a new set of test forces (U inputs) are used to try to identify the T matrix. If the acceleration still diverges, the simulation aborts. Simulation runs where acceleration decreases are separated into three categories: *Strong* results, *Weak*, and *Failure*. Strong results are those which have a final acceleration less than 1 m/s^2. Typically, simulation runs that converge below this threshold result in a low error - usually well within 1% of truth. Weak results are those that elicit slowly converging acceleration and result in a final acceleration between 1 - 5 m/s^2. These results are often accurate but can occasionally stray far outside an acceptable error range, above 10%. Failure results are those that diverge or have a final acceleration greater than 5 m/s^2. These results are almost always in the unacceptable range, and will not be included in statistical plots.

For the compensated loading condition, tabular results of convergence are displayed in Table 6. Convergence tables for the 50 N and 350 N cases can be found in Appendix B.

Test Condition		Convergence (%)			Result (%)		
Freq. (rad/s)	Exc. Force (N)	Run 1	Run 2	Failure	Strong	Weak	Failure
120	68.6	100	0	0	100	0	0
205	59.1	100	0	0	100	0	0
300	50.0	100	0	0	100	0	0
440	91.9	100	0	0	100	0	0
650	173.2	91.2	8.8	0	94.8	0.4	4.8
1280	83.2	100	0	0	100	0	0
1800	50.0	100	0	0	100	0	0
2340	150.3	100	0	0	100	0	0
2750	263.7	100	0	0	100	0	0

Table 6: Compensated Dynamic Force (Bearing 1)

Measurement Errors Failed results are discarded but Strong & Weak results are included in these tabulations. In reality, a trial that ends in a weak result should be taken with caution. Figures 5.4a and 5.4b show histograms of resultant amplitude and phase errors, respectively, for the 120 rad/s test case. Results at each frequency and dynamic load condition were analyzed in the same manner. In table 7, 95% confidence intervals are established around the median of each dataset. Error values are absolute value (i.e., a 0.3% error may represent a +0.3% or -0.3% difference from truth). Results tables for the 50 N and 350 N cases can be found in Appendix B. The information presented in these tables are shown graphically in the next section for easier analysis.

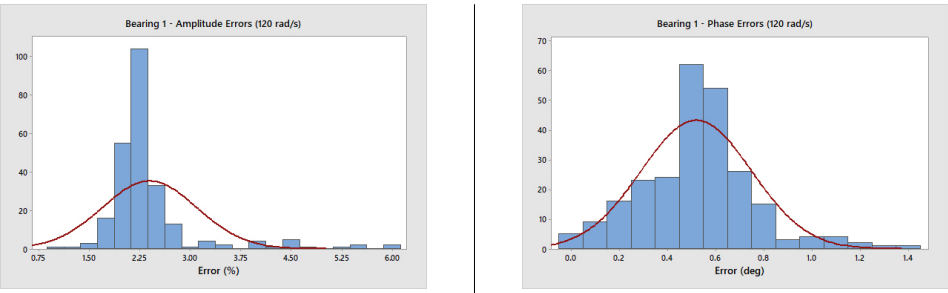

(a) Amplitude Error Distribution (%)

(b) Phase Error Distribution (rads)

Figure 5.4: Results from the 120 rad/s Compensated Dynamic force test case for Bearing 1

	Amplitude Error (%)			Phase Error (deg)		
Freq. (rad/s)	Lower	**Median**	Upper	Lower	**Median**	Upper
120	1.600	**1.630**	1.660	0.444	**0.461**	0.495
205	0.460	**0.530**	0.570	0.246	**0.283**	0.312
300	0.160	**0.170**	0.190	0.175	**0.197**	0.210
440	0.190	**0.225**	0.300	0.036	**0.041**	0.057
650	0.094	**0.122**	0.169	0.017	**0.021**	0.027
1280	0.680	**0.790**	0.860	0.037	**0.040**	0.046
1800	0.680	**0.730**	0.790	0.375	**0.416**	0.458
2340	0.230	**0.248**	0.260	0.226	**0.265**	0.295
2750	0.351	**0.377**	0.398	0.148	**0.173**	0.219

Table 7: Amplitude & Phase Errors (Bearing 1)

5.2.3 Graphical Results

Figures 5.5 through 5.8 show the median errors and limits of the 95% confidence bounds for all test frequencies on a logarithmic scale. Most test cases fall at or below the 1% target force amplitude error. All test cases are within the 1 degree target phase error. There is a bit of variability in the median errors across frequencies which may be due to inherent system gains. This becomes especially apparent at the lower dynamic load cases in figures 5.7 and 5.8. Further study would need to be conducted for a better perspective on the slight shifts in median error across the test frequency bandwidth.

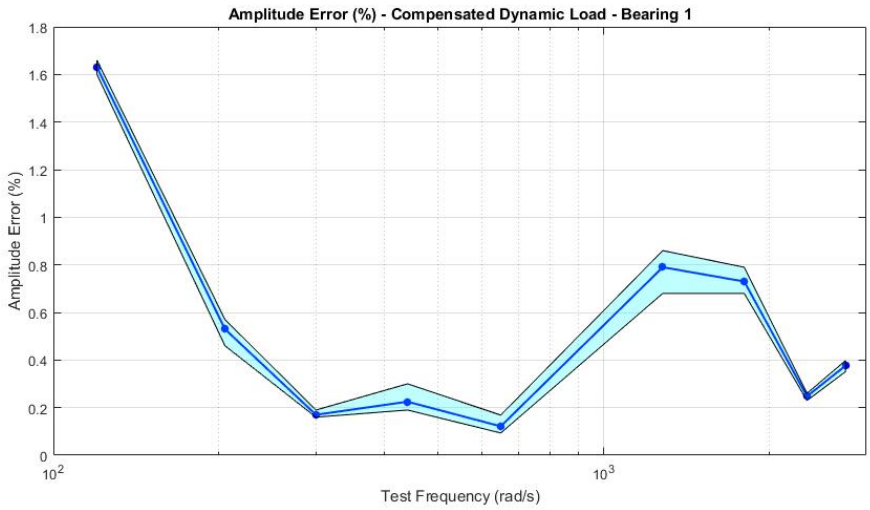

Figure 5.5: Amplitude Error, Compensated Dynamic Force

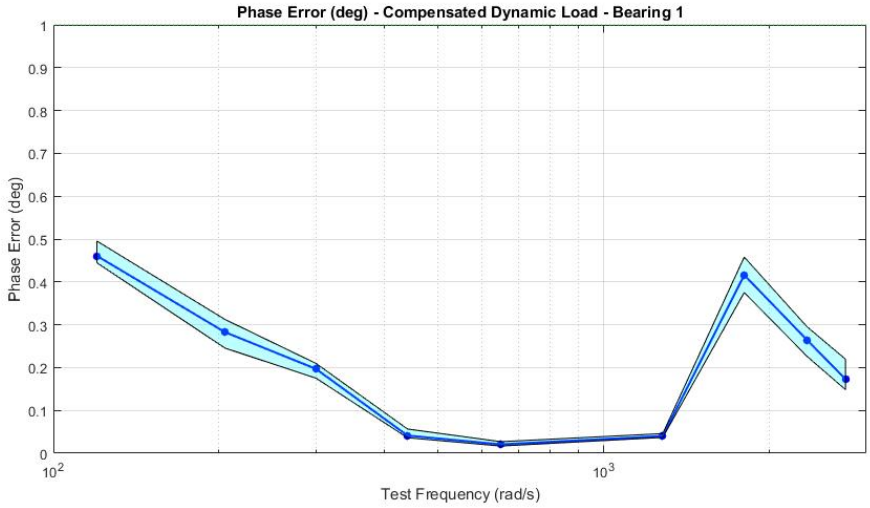

Figure 5.6: Phase Error, Compensated Dynamic Force

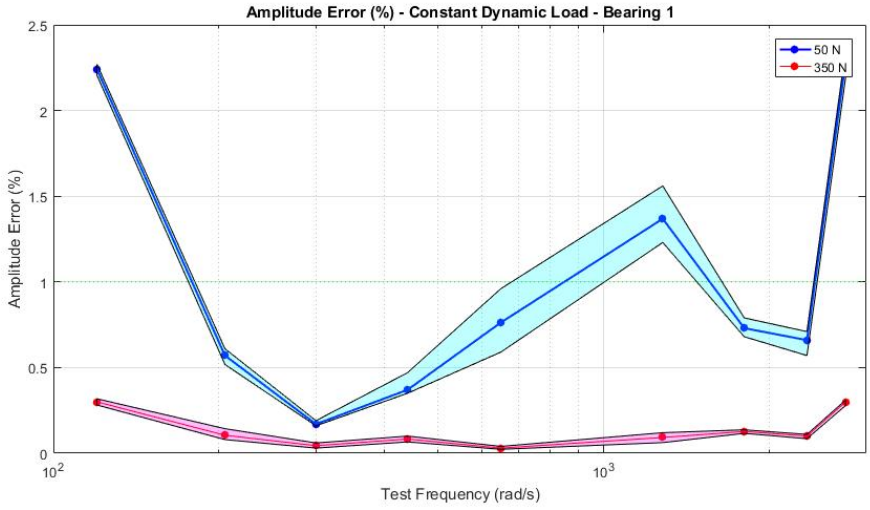

Figure 5.7: Amplitude Error, 50 & 350 N Dynamic Force

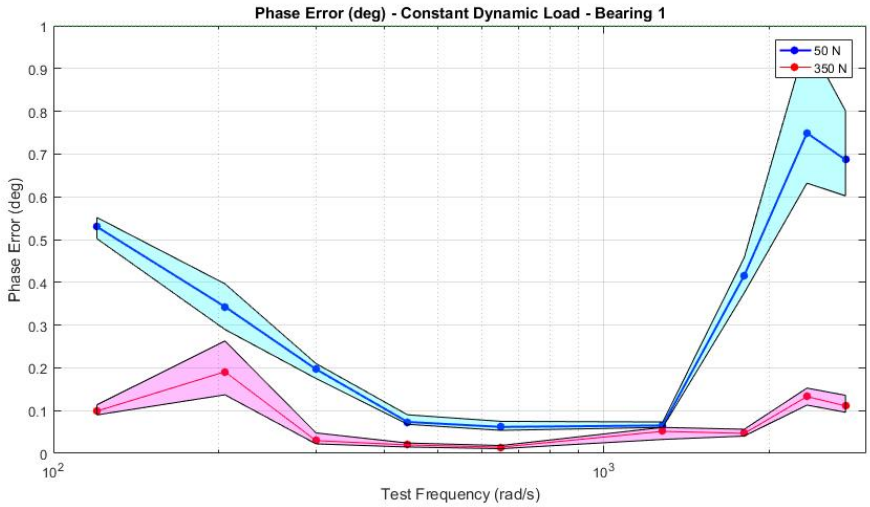

Figure 5.8: Phase Error, 50 & 350 N Dynamic Force

5.3 Test Case 2: High Stiffness Bearing

5.3.1 Test Parameters

This bearing was modeled with the following parameters:

- Z-Direction Stiffness: 100,000,000 N/m (571,000 lbf/in)
- Z-Direction Damping: 5000 Ns/m (28.5 lbfs/in)

5.3.2 Tabular Results

For the three loading conditions, tabular results of convergence are displayed in Table 8. Measurement errors for bearing 2 follow the same format as those for bearing 1, described above. The results of the compensated load case are shown in Table 9, with additional results tabulated in Appendix B.

Test Condition		Convergence (%)			Result (%)		
Freq. (rad/s)	Exc. Force (N)	Run 1	Run 2	Failure	Strong	Weak	Failure
120	236	100	0	0	100	0	0
205	213	80.0	18.4	1.6	94.4	2.0	3.6
300	193	92.4	7.6	0	97.2	2.0	0.8
440	338	100	0	0	91.2	4.0	4.8
650	525	77.2	17.2	5.6	84.8	3.6	11.6
1280	382	90.4	8.8	0.8	91.6	3.2	5.2
1800	286	88.0	11.6	0.4	92.4	2.4	5.2
2340	162	100	0	0	90.8	4.0	5.2
2750	66	100	0	0	100	0	0

Table 8: Compensated Dynamic Force (Bearing 2)

	Amplitude Error (%)			Phase Error (deg)		
Freq. (rad/s)	Lower	**Median**	Upper	Lower	**Median**	Upper
120	0.470	**0.480**	0.491	0.093	**0.107**	0.124
205	0.110	**0.146**	0.180	0.101	**0.135**	0.179
300	0.035	**0.045**	0.051	0.040	**0.052**	0.061
440	0.080	**0.100**	0.126	0.020	**0.025**	0.036
650	0.030	**0.040**	0.060	0.012	**0.016**	0.022
1280	0.070	**0.090**	0.120	0.023	**0.027**	0.030
1800	0.200	**0.240**	0.287	0.011	**0.013**	0.016
2340	0.350	**0.411**	0.470	0.027	**0.032**	0.037
2750	1.126	**1.150**	1.200	0.258	**0.268**	0.283

Table 9: Amplitude & Phase Errors (Bearing 2)

5.3.3 Graphical Results

Figures 5.9 through 5.12 show the median errors and limits of the 95% confidence bounds for all test frequencies on a logarithmic scale. Similar to bearing 1, most force amplitude errors are at or below the 1% target, and all phase errors are below the 1 degree error target. There is variability in the median errors across frequencies, which is especially apparent at the low dynamic load cases seen in Figures 5.11 and 5.12.

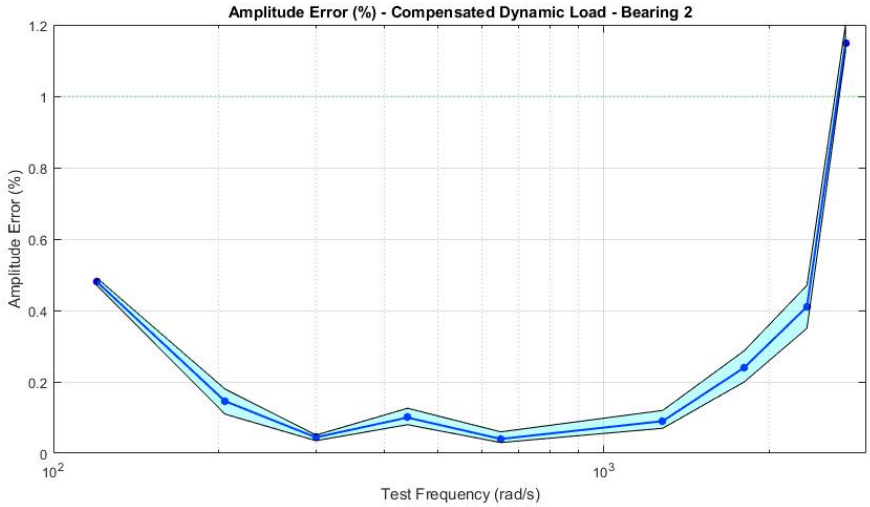

Figure 5.9: Amplitude Error, Compensated Dynamic Force

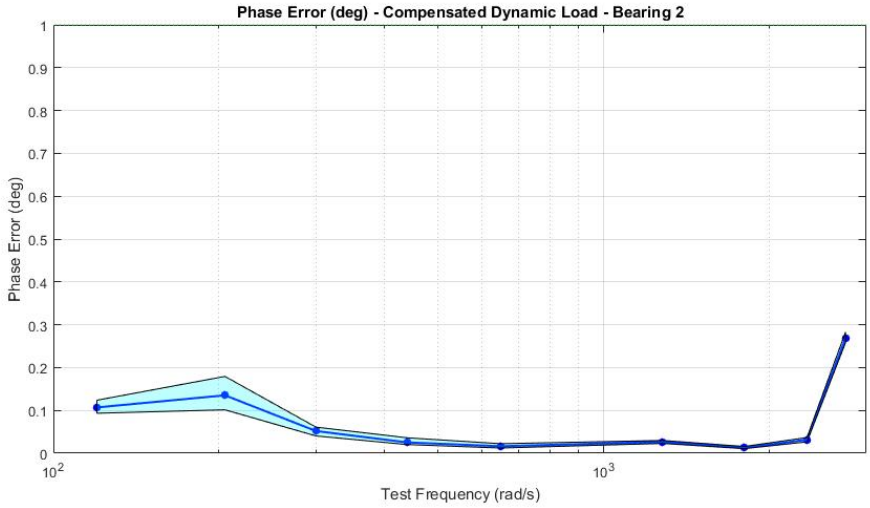

Figure 5.10: Phase Error, Compensated Dynamic Force

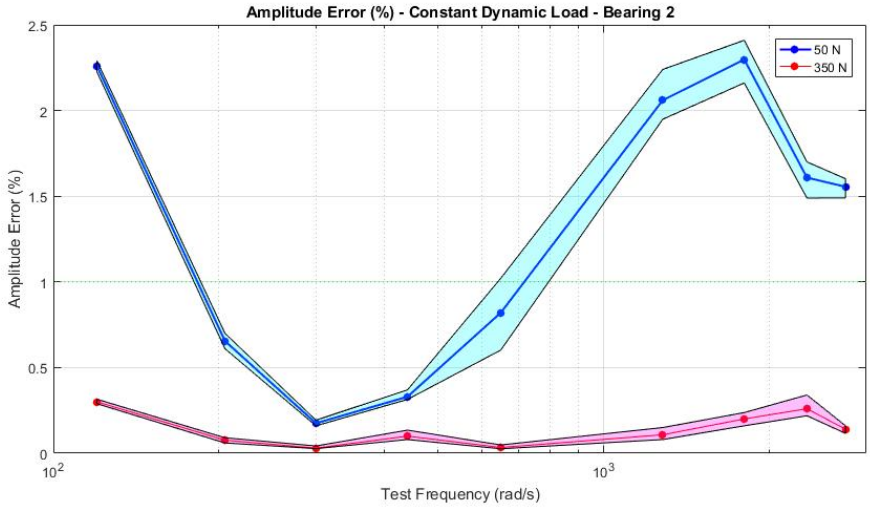

Figure 5.11: Amplitude Error, 50 & 350 N Dynamic Force

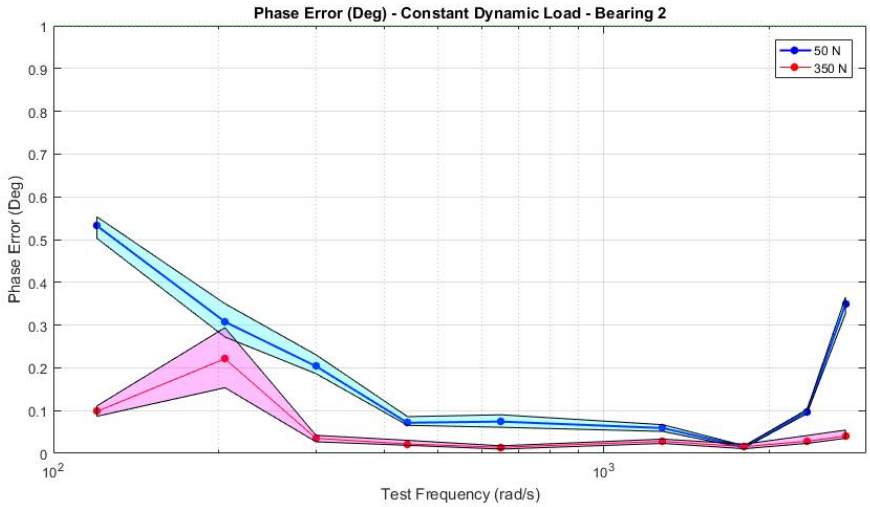

Figure 5.12: Phase Error, 50 & 350 N Dynamic Force

5.4 Discussion

The primary goal of the experiment was to accurately determine bearing force within 1% of true amplitude, and 1 degree of true phase. Collecting the results for all frequencies, the medians of 81.4% of amplitude measurements and 100% of phase measurements fell within the target. Concatenating all results and error boundaries for each bearing, the following confidence intervals can be established for each experiment in Table 10.

	Amplitude Error (%)			Phase Error (deg)		
Bearing	Lower	Median	Upper	Lower	Median	Upper
1 (Soft)	0.3410	0.3510	0.3700	0.1203	0.1271	0.1340
2 (Stiff)	0.3101	0.3200	0.3410	0.0613	0.0635	0.0676

Table 10: Results from All trials, both bearings

Overall error frequency distributions are shown in Figures 5.13 and 5.14. One thing to keep in mind is that these errors were for three dynamic load test cases. If more cases were studied, the distribution would have a slightly different trend.

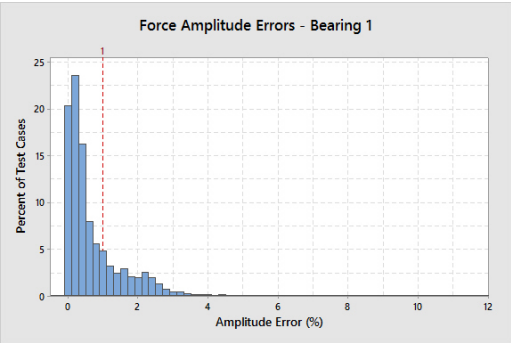

(a) Amplitude Error Distribution (%)

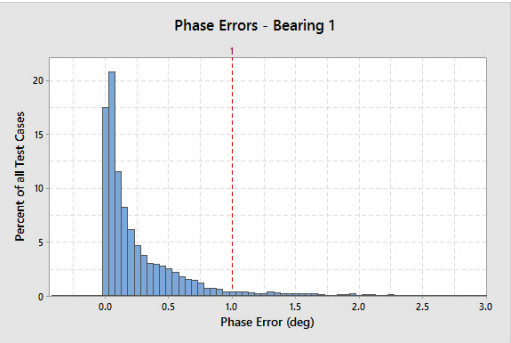

(b) Phase Error Distribution (deg)

Figure 5.13: Results Frequency Distribution for Bearing 1

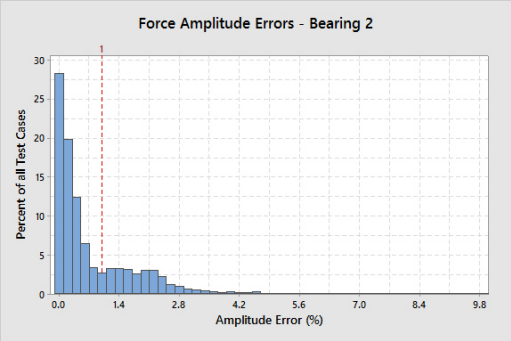

(a) Amplitude Error Distribution (%)

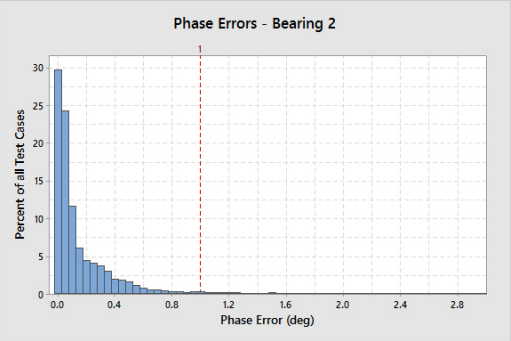

(b) Phase Error Distribution (deg)

Figure 5.14: Results Frequency Distribution for Bearing 2

From the graphical results in the previous section, however, it is obvious that the expected errors are frequency dependent; For example, the median amplitude errors were higher for all dynamic loads at the 120 rad/s frequency than they were at 205 rad/s, and as such, we can expect that an experiment that is run at the lower frequency would elicit larger errors. The error ranges were not consistent between bearings, however, larger errors were generally experienced at the lowest and highest test frequencies for each case.

An important trend that can be seen when comparing the same test frequency at different dynamic excitations is that the amplitude of the dynamic load has a direct effect on the cancellation amplitude and phase errors. This isn't directly obvious because each frequency is tested at a different dynamic load in order to hit the target relative displacement. However, when all frequencies are plotted on a chart of error vs. dynamic excitation, it becomes clear that lower dynamic excitation forces result in higher errors, across all test frequencies. This indicates that force identifications will be more accurate if the dynamic load is at least 20% of the static system load. See Figures 5.15 through 5.18.

Another important consideration should be taken when looking at the convergence failures across test cases. It seems that certain combinations of test frequency and dynamic load are more likely to lead to failed adaptive open loop convergence or "weak" results. Due to the inherent system gains, high cancellation force amplitudes are required at certain frequencies in order to match the bearing force. It seems that the controller is more likely to fail in the test cases that require larger cancellation forces. Figures 5.19 & 5.20 show the percentage of failed convergences as a function of required cancellation force for Bearing 1 & 2, respectively.

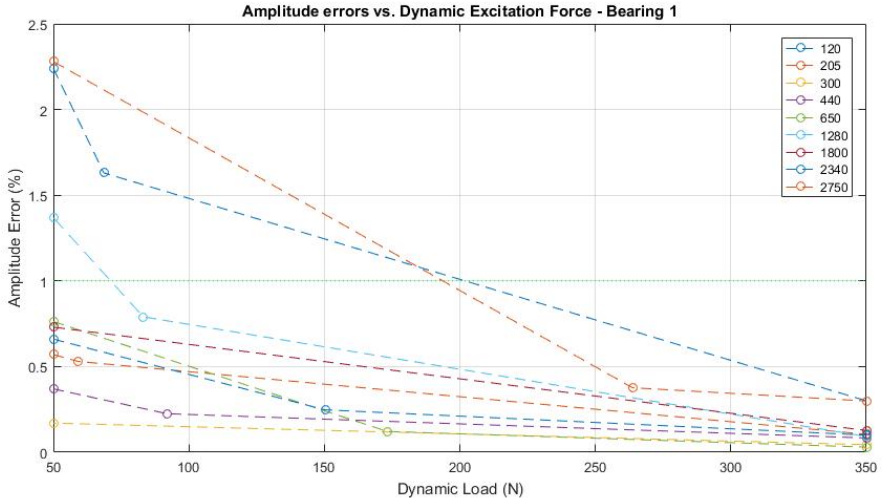

Figure 5.15: Errors for all frequencies as a function of dynamic force amplitude, Bearing 1

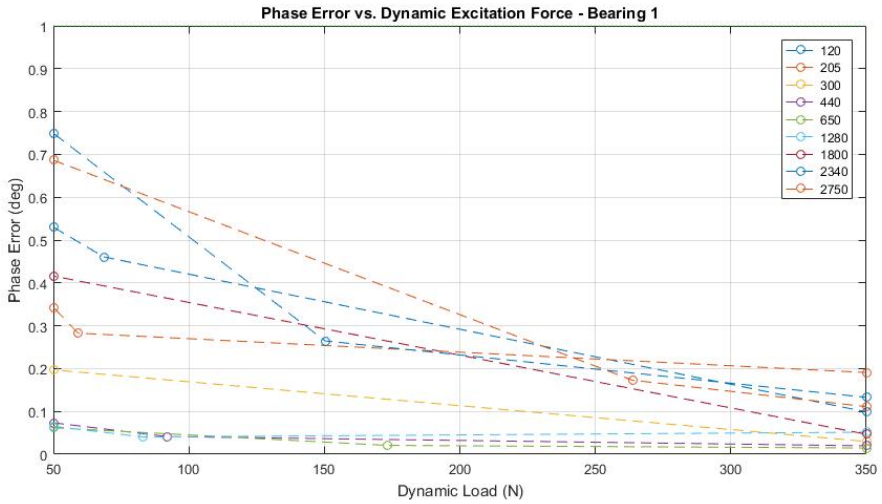

Figure 5.16: Errors for all frequencies as a function of dynamic force amplitude, Bearing 1

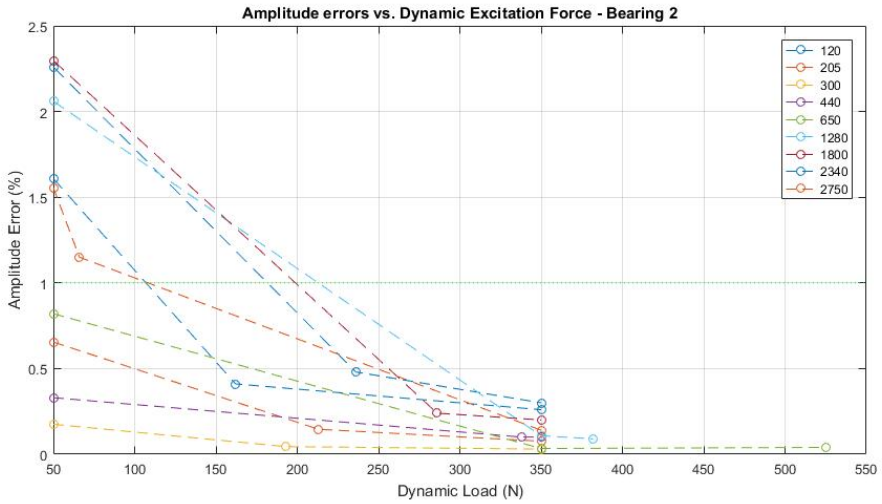

Figure 5.17: Errors for all frequencies as a function of dynamic force amplitude, Bearing 2

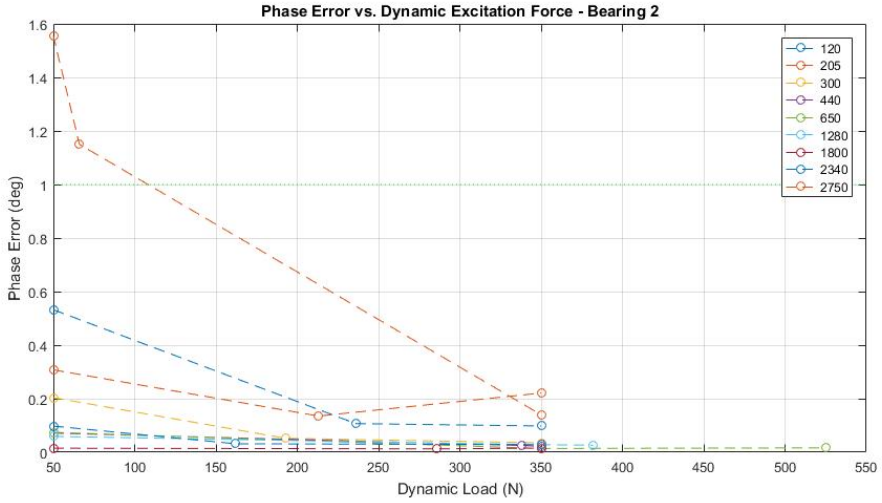

Figure 5.18: Errors for all frequencies as a function of dynamic force amplitude, Bearing 2

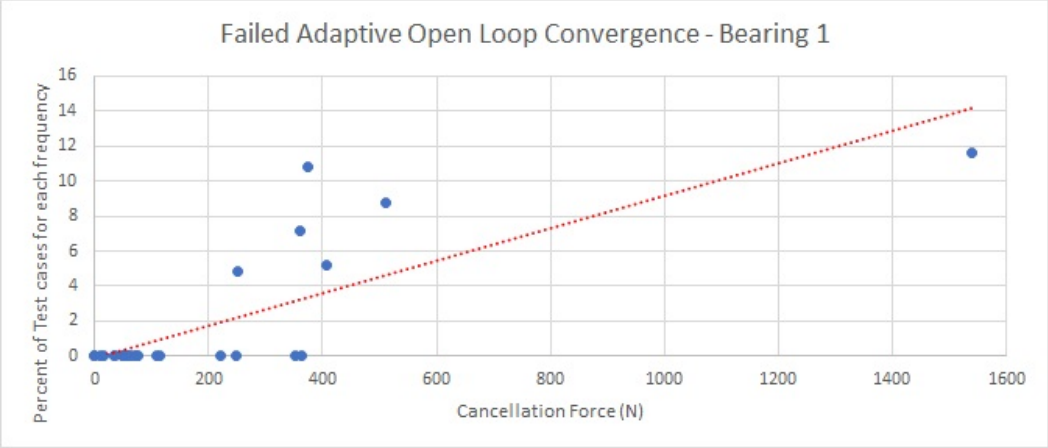

Figure 5.19: Failed Results by Cancellation Force, Bearing 1

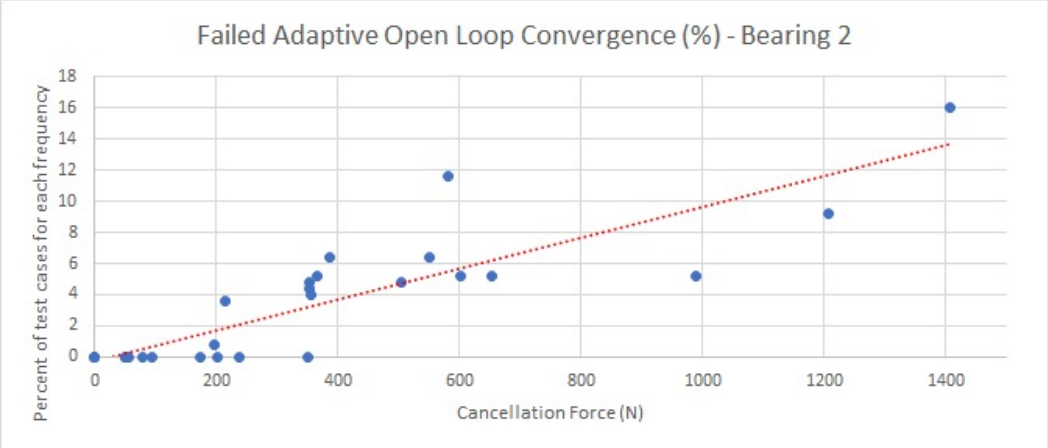

Figure 5.20: Failed Results by Cancellation Force, Bearing 2

5.5 Identifying Dynamic Coefficients with the ALCTR

While the primary purpose of the ALCTR is to provide *force* measurements, it would be useful to begin to make bearing dynamic coefficient estimations using the rig itself. This simulation model is already organized to output data regarding the relative displacement between the rotor and housing, in two sensor locations as indicated in the Solid Modeling section. In addition, sensor errors are defined by the Lion Precision datasheet (see Appendix G) and included in the output for the sensor readings. Tracking the motion between the components, we can develop confidence boundaries on relative *displacement* using the same Monte Carlo study, and use this information together with the force amplitude and phase determinations as defined above to make a prediction as to the dynamic coefficients of the test bearing. Since these values can be determined exactly through finite element analysis software, errors in coefficient determination can be built in the same manner. The use of the relative displacement data to achieve this would be the next milestone in the ALCTR development.

Stiffness and damping coefficients were estimated using the relation below in equation 5.2.

$$\frac{F}{x} = k + j\omega c \tag{5.2}$$

Where F and x are both complex representations of the force and displacement amplitude & phase, respectively. Here, the real component represents the stiffness and the imaginary component, divided by the test frequency, represents the damping. The Monte Carlo study was performed for three test frequencies and two load conditions for each bearing, as indicated in Table 11.

Test Frequencies	205 rad/s
	650 rad/s
	2340 rad/s
Test Loads	Compensated
	350 N

Table 11: Test Conditions for Stiffness & Damping Identification

5.5.1 Dynamic Coefficient Identification Results

Figures 5.21a and 5.21b show the median errors and 95% confidence intervals for the stiffness and damping parameter identifications for Bearing 1. These of course are compared to the true values as determined by the FEA analysis of the solid model.

Figures 5.22a and 5.22b show the median errors and 95% confidence intervals for the stiffness and damping parameter identifications for Bearing 2.

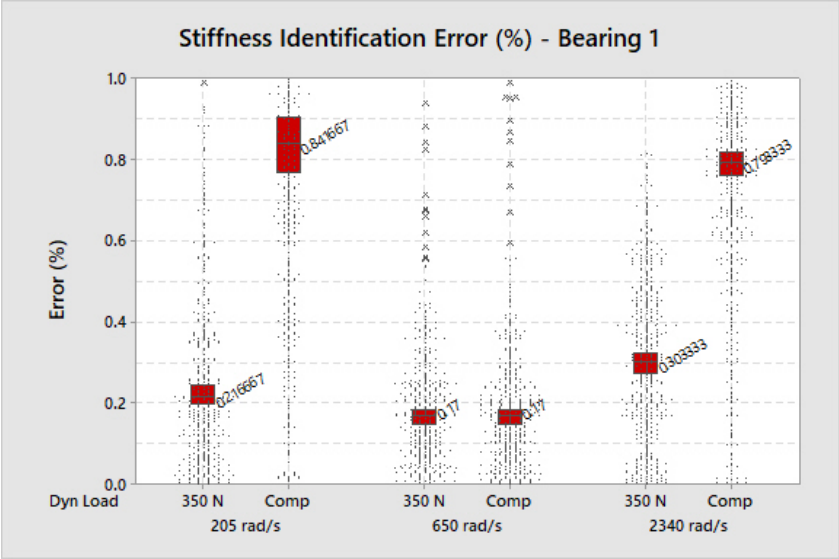

(a) Stiffness Errors (%)

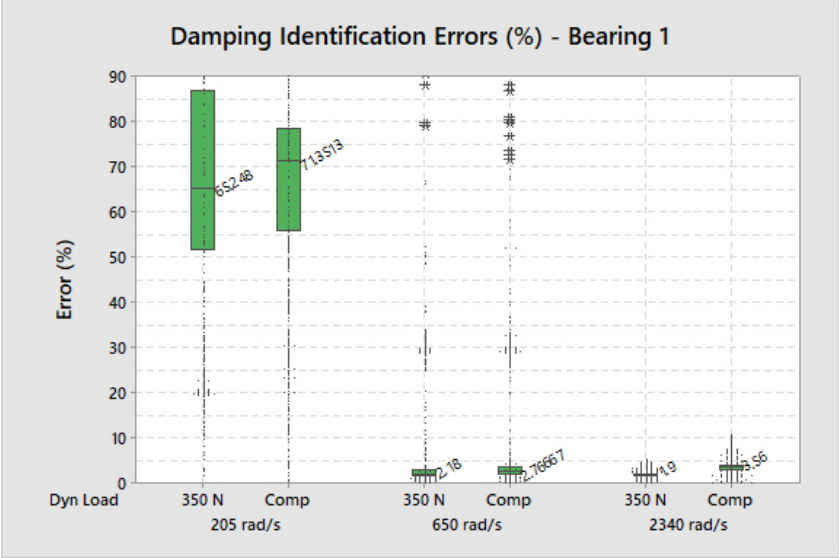

(b) Damping Errors (%)

Figure 5.21: Bearing 1 Stiffness and Damping Identification

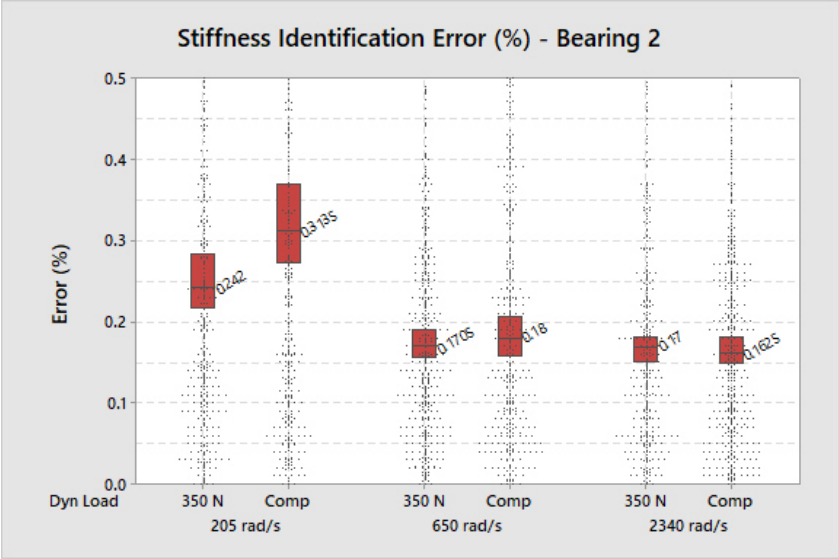

(a) Stiffness Errors (%)

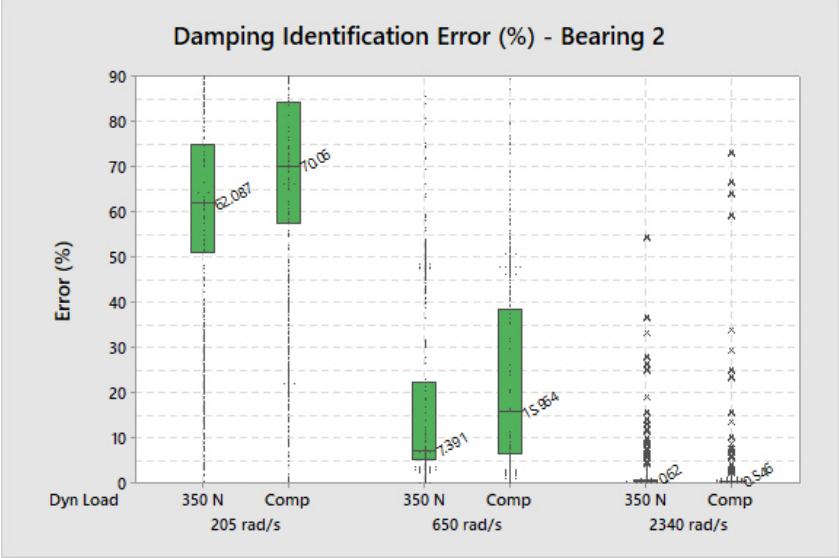

(b) Damping Errors (%)

Figure 5.22: Bearing 1 Stiffness and Damping Identification

Discussion Preliminary results for dynamic coefficient identification indicate that the ALCTR method of force measurement is extremely effective. Stiffness coefficients for all test cases are correctly identified well within 1% of true value. Damping coefficient determination was a bit more variable. Results were heavily dependent on the test frequency, however damping identifications on the 650 and 2340 rad/s cases for both bearings were accurate to a significantly better degree than any previous method of determining damping coefficients. All results from this study are tabulated below, in Table 12

		Stiffness (%)			Damping (%)		
		Lower	**Median**	Upper	Lower	**Median**	Upper
Bearing 1	205 rad/s (all)	0.440	**0.500**	0.563	56.200	**68.100**	77.410
	650 rad/s (all)	0.156	**0.170**	0.177	2.029	**2.440**	3.040
	2340 rad/s (all)	0.470	**0.488**	0.530	2.227	**2.420**	2.566
Bearing 2	205 rad/s (all)	0.255	**0.279**	0.305	58.320	**66.400**	74.432
	650 rad/s (all)	0.161	**0.177**	0.190	6.575	**9.951**	25.016
	2340 rad/s (all)	0.155	**0.165**	0.180	0.522	**0.577**	0.637

Table 12: Confidence intervals for all Stiffness & Damping identification trials

6 Conclusions

6.1 Findings and Contributions

ALCTR Force measurements The results of this experiment indicate that the Active Load Cell is an accurate method of making force amplitude and phase predictions across the range of frequencies between 100-3000 rad/s (20-500 Hz). Results are most accurate when the dynamic load applied is at least 20% of the static system load (equipment weight + external loading). The overall median error in amplitude identification was approximately 0.35% for the Bearing 1 (low stiffness), and 0.32% for Bearing 2 (high stiffness). The overall median error in phase identification was approximately 0.12 degrees for Bearing 1, and 0.06 degrees for Bearing 2.

These results are well within the target range specified prior to this study. The findings of this simulation strongly suggest that pursuing the Active Load Cell as a method of force identification is beneficial not only to the FFBTR, but as a standalone rig capable of making identifications for other purposes within ROMAC and beyond.

ALCTR Dynamic coefficient measurements Initial estimates of bearing coefficient errors indicate that using the Active Load Cell concept for force identification may significantly improve results obtained for dynamic cofficients. The trials runs on three test frequencies were much more accurate for all stiffness and most damping identifications than all previous methods of studying these coefficients. More work needs to be done to develop more realistic confidence bounds, particularly taking additional sources of error into consideration. However, the results of this study show promise that the coupling of the ALC force measurements system and FFBTR may provide significant improvements to the way fluid film bearing coefficients are studied.

6.2 Future Work

The information presented in this thesis comprises a large majority of research and simulated work that is required prior to the time and expense of building a physical test rig. Due to time constraints, some parameters had to be prioritized over others; not that these additional considerations should not be analyzed, but they were less imperative to understanding the overall operation of the rig. Further study on the feasibility of the ALC should cover the below considerations.

Magnetic System Full specifications need to made in terms of identifying appropriate equipment for a robust and effective magnetic suspension system. The analysis done here using FEMM is a strong basis as to the rough actuator requirements, however, these actuators were simulated independently in a vacuum environment. The magnetic amplifier model used in this simulation is rudimentary and not based on hardware specs. The ability of the magnetic actuators to effectively support the housing structure will depend on the slew rate and other parameters available due to the amplifier. This equipment needs to be researched and a more thorough amplifier model should be included for more realistic response of the magnets.

Physical Modeling The solid structures modeled in CAD here are mostly complete when it comes to rotor and housing masses. The framing system was not fully developed for the purposes of this paper. For example, manufacturing the upper and lower platforms out of solid billets of aluminum would be costly and would not allow for any sort of modularity or adjustment. These components are more likely to be constructed from a framing platform, one which was initially considered was the 80/20 product line [28]. A representative from 80/20 came to the University of Virginia to give a product demo and have an initial consultation on the requirements for this project. This is one good option to follow up on when it comes time to develop the ALC test rig framework.

The housing flexures that were designed were modeled from simple extension springs, the specifications of which were pulled from McMaster-Carr part no. 1832K27 (See Appendix G). More sophisticated flexures may need to be developed and analyzed in finite element analysis software in order to evaluate their effect on the ALC test rig control. This is particularly important because through simulation it was shown that stiffness and damping applied on the housing in the test direction (z) had a significant impact on the ability of the adaptive open loop controller to converge. A mechanism that would allow for stiffness in the x and y planes but offer minimal stiffness in the z direction would be ideal.

No research was done into the foundation and vertical support rail system. Developing a robust foundation should also be considered when analyzing the framing structure and establishing a physical footprint in a test facility.

Additional Sources of Error The error sources analyzed were primarily due to equipment misalignments and accelerometer specifications. There are other sources of error that may cast new insight on error boundaries of force identification. These include but are not limited to shaker calibration, support and foundation resonant frequencies, thermal effects on sensors, and user error.

Signal Processing The data from the displacement sensors in this model that was utilized in the PID controllers was assumed to be filtered. A more realistic model should feature noisy sensor data that has been processed through an appropriate lowpass or averaging filter. Spikes in sensor data may cause a jumpy response from the magnetic actuators.

References

[1] "Pioneer motor bearing website." [Online]. Available: https://www.pioneer1.com/engineering/fluid-pivot-tilting-pad-journal-bearings/

[2] P. S. Tim Dimond, Paul Allaire, "Modeling of fluid film bearings and design of a fluid film bearing test rig," UVA, ROMAC Report 586, May 2011.

[3] T. Dimond, R. Rockwell, P. Sheth, and P. Allaire, "A new fluid film bearing test rig for oil and water bearings," UVA, ROMAC Report 530, February 2008.

[4] M. He and P. Allaire, "Thermoelastohydrodynamic analysis of journal bearings with 2d generalized energy equation," in *Proc. 6th international Conference on Rotor dynamics*. IFTOMM, 2002, sydney, Aus.

[5] T. Dimond, P. Sheth, P. Allaire, and M. He, "Identification methods and test results for tilting pad and fixed geometry journal bearing dynamic coefficients–a review," *Shock and vibration*, vol. 16, no. 1, pp. 13–43, 2009.

[6] R. F. L.J. Read, "The design and implementation of a fluid film bearing test rig," UVA, ROMAC Report 225, May 1985.

[7] E. Knopf and R. Nordmann, "Identification of the dynamic characteristics of turbulent journal bearings using active magnetic bearings," in *Proc. 7th International Conference on Vibrations in Rotating Machinery*. IMechE, 2000, pp. 381–390, nottingham, UK.

[8] [Online]. Available: https://pages.shanti.virginia.edu/romac/fluid-film-bearing-test-rig/

[9] G. Kostrzewsky, D. Taylor, and R. Flack, "The design and application of a bearing test rig for dynamic coefficients," UVA, ROMAC Report 325, June 1991.

[10] D. Tschoepe, "Measurements vs. predictions for the static and dynamic characteristics of a four-pad rocker pivot tilting pad journal bearing," Thesis, Texas A&M University, December 2012.

[11] G. Kostrzewsky and R. Flack, "Accuracy evaluation of experimentally derived dynamic coefficients of fluid-film bearings," UVA, ROMAC Report 274, June 1988.

[12] Z. Zutavern and D. Childs, "Fiber-optic strain gage calibration and dynamic flexibility transfer function identification in magnetic bearings," in *Proc. 9th International symposium on Magnetic Bearings*, 2004, lexington, KY.

[13] M. Aenis, E. Knopf, and R. Nordmann, "Active magnetic bearings for the identification and fault diagnosis in turbomachinery," in *Mechatronics*, 2002, pp. 1011–1021.

[14] A. Traxler and G. Schweitzer, "Measurement of the force characteristics of a contactless electromagnetic rotor bearing," *Institite For Mechanics*, 1984, eTH Zurich, Switzerland.

[15] C. Lee, Y. Ha, and C. Kim, "Identification of active magnetic bearing system using magnetic force measurement," in *The Fourth International Symposium on Magnetic Bearings*, 1994, zurich, Switzerland.

[16] M. Matros, J. Sobotzik, and R. Nordmann, "A new model-based method for the accurate measurement of magnetic bearing forces," in *Fourth international symposium Magnetic Bearing Suspension technology*, 1996, pp. 239–248, gifu City, Japan.

[17] S. Dynamics, *Vibration Testing Systems*, Sentek Dynamics, 2370 Owen St Santa Clara CA 95054, July 2015.

[18] G. Schweitzer, H. Bleuler, E. Maslen, M. Cole, P. Keogh, R. Larsonneur, E. Maslen, r. Nordmann, Y. Okada, G. Schweitzer *et al.*, *Magnetic Bearings: Theory, Design, and Application to Rotating Machinery*. Springer Berlin Heidelberg, 2009. [Online]. Available: https://books.google.com/books?id=1Kyg5dWyBasC

[19] D. C. Meeker, "Finite element method magnetics," http://www.femm.info, 03 December 2006, version 4.0.1.

[20] D. Meeker, "Femm finite element method magnetics," http://www.femm.info/wiki/download, 2016-05-16.

[21] D. Meeker, "Improvised open boundary conditions for magnetic finite elements," *IEEE Transactions on Magnetics*, vol. 49, no. 10, pp. 5243–5247, Oct 2013.

[22] D. Meeker, *Finite Element Method Magnetics User's Manual*, version 4.2 ed., IEEE, October 2015, http://www.femm.info/Archives/doc/manual42.pdf.

[23] C. Knospe, "Reducing unbalance response with magnetic bearings," *Int, Rep., Center for Magnetic Bearings, University of Virginia, VA*, 1992.

[24] D. Baun, *Hydrodynamic forces in centrifugal pump and compressor impellers in volute casings: measurements using magnetic bearings and CFD simulations*. University Microfilms, 2004.

[25] R. Hope, "Adaptive open loop control of synchronous rotor vibration using magnetic bearings," Universirty of Virginia, ROMAC Report 375, August 1994.

[26] C. R. Knospe, R. Hope, S. J. Fedigan, and R. D. Williams, "Experiments in the control of unbalance response using magnetic bearings," *Mechatronics*, vol. 5, no. 4, pp. 385 – 400, 1995. [Online]. Available: http://www.sciencedirect.com/science/article/pii/095741589500015W

[27] R. Harrison, "Introduction to monte carlo simulation," *AIP conference proceedings*, no. 1204, pp. 17–21, 2010.

[28] “80/20 website.” [Online]. Available: https://www.8020.net/

A Test Rig Physical Parameters

Mom. of Inertia			**Stiffness**			**Damping**		
Ixx	0.054	*kgm*	**Kx**	1.00E+08	*N/m*	**Cx**	1.00E+02	*Ns/m*
Iyy	0.162	*kgm*	**Ky**	1.00E+08	*N/m*	**Cy**	1.00E+02	*Ns/m*
Izz	0.159	*kgm*	**Kz**	0.00E+00	*N/m*	**Cz**	0.00E+00	*Ns/m*
Ixy	0.000	*kgm*	**K**α	1.00E+08	*Nm/rad*	**C**α	1.00E+02	*Nms/rad*
Ixz	0.000	*kgm*	**K**β	1.00E+08	*Nm/rad*	**C**β	1.00E+02	*Nms/rad*
Iyz	0.000	*kgm*	**K**γ	1.00E+08	*Nm/rad*	**C**γ	1.00E+02	*Nms/rad*
Mass	22.319	*kg*						

Rotor Parameters

Mom. of Inertia			**Stiffness**			**Damping**		
Ixx	0.138	*kgm*	**Kx**	4.15E+04	*N/m*	**Cx**	4.15E+01	*Ns/m*
Iyy	0.156	*kgm*	**Ky**	4.15E+04	*N/m*	**Cy**	4.15E+01	*Ns/m*
Izz	0.210	*kgm*	**Kz**	0.00E+00	*N/m*	**Cz**	0.00E+00	*Ns/m*
Ixy	0.000	*kgm*	**K**α	0.00E+00	*Nm/rad*	**C**α	0.00E+00	*Nms/rad*
Ixz	0.000	*kgm*	**K**β	0.00E+00	*Nm/rad*	**C**β	0.00E+00	*Nms/rad*
Iyz	0.000	*kgm*	**K**γ	4.15E+04	*Nm/rad*	**C**γ	4.15E+01	*Nms/rad*
Mass	20.870	*kg*						

Housing Parameters

Mom. of Inertia			**Stiffness**			**Damping**		
Ixx	0.000	kgm	**Kxx**	3.00E+06	N/m	**Cxx**	1.50E+00	Ns/m
Iyy	0.000	kgm	**Kyy**	3.00E+06	N/m	**Cyy**	1.50E+00	Ns/m
Izz	0.000	kgm	**Kzz**	3.00E+07	N/m	**Czz**	1.50E+03	Ns/m
Ixy	0.000	kgm	**Kxy**	0.00E+00	N/m	**Cxy**	0.00E+00	Ns/m
Ixz	0.000	kgm	**Kxz**	0.00E+00	N/m	**Cxz**	0.00E+00	Ns/m
Iyz	0.000	kgm	**Kyz**	0.00E+00	N/m	**Cyz**	0.00E+00	Ns/m
Mass	0.000	kg	**K**α	0.00E+00	Nm/rad	**C**α	0.00E+00	Nms/rad
			Kβ	0.00E+00	Nm/rad	**C**β	0.00E+00	Nms/rad
			Kγ	0.00E+00	Nm/rad	**C**γ	0.00E+00	Nms/rad

Bearing 1 Parameters

Mom. of Inertia			**Stiffness**			**Damping**		
Ixx	0.000	*kgm*	**Kxx**	1.00E+07	*N/m*	**Cxx**	5.00E+00	*Ns/m*
Iyy	0.000	*kgm*	**Kyy**	1.00E+07	*N/m*	**Cyy**	5.00E+00	*Ns/m*
Izz	0.000	*kgm*	**Kzz**	1.00E+08	*N/m*	**Czz**	5.00E+03	*Ns/m*
Ixy	0.000	*kgm*	**Kxy**	0.00E+00	*N/m*	**Cxy**	0.00E+00	*Ns/m*
Ixz	0.000	*kgm*	**Kxz**	0.00E+00	*N/m*	**Cxz**	0.00E+00	*Ns/m*
Iyz	0.000	*kgm*	**Kyz**	0.00E+00	*N/m*	**Cyz**	0.00E+00	*Ns/m*
Mass	0.000	kg	**K**α	0.00E+00	*Nm/rad*	**C**α	0.00E+00	*Nms/rad*
			Kβ	0.00E+00	*Nm/rad*	**C**β	0.00E+00	*Nms/rad*
			Kγ	0.00E+00	*Nm/rad*	**C**γ	0.00E+00	*Nms/rad*

Bearing 2 Parameters

A	**x**	-0.0440	m	**B**	**x**	-0.0440	m
	y	-0.1360	m		**y**	0.1360	m
	z	-0.0133	m		**z**	-0.0133	m
C	**x**	0.0440	m	**D**	**x**	0.0440	m
	y	0.1360	m		**y**	-0.1360	m
	z	-0.0133	m		**z**	-0.0133	m

Sensor Locations (from housing CG)

A	**x**	-0.0950	m	**B**	**x**	-0.0950	m
	y	-0.1360	m		**y**	0.1360	m
	z	-0.0008	m		**z**	-0.0008	m
C	**x**	0.0950	m	**D**	**x**	0.0950	m
	y	0.1360	m		**y**	-0.1360	m
	z	-0.0008	m		**z**	-0.0008	m

Actuator Locations (from housing CG)

X1R	**x**	-0.1000	m	**X2R**	**x**	0.1000	m
	y	0.0000	m		**y**	0.0000	m
	z	-0.0438	m		**z**	-0.0438	m
X1H	**x**	-0.1000	m	**X2H**	**x**	0.1000	m
	y	0.0000	m		**y**	0.0000	m
	z	0.1171	m		**z**	0.1171	m

Relative Disp. Sensor Locations (from resp body CG)

EXC	**x**	0.0000	m	**CAN**	**x**	0.0000	m
	y	0.0000	m		**y**	0.0000	m
	z	0.1407	m		**z**	-0.1499	m
				ACC	**x**	0.0000	m
					y	-0.0750	m
					z	0.0536	m

Shaker and Accel. Locations (from resp body CG)

B All Results

B.1 Bearing 1

Test Condition		Convergence (%)			Result (%)		
Freq. (rad/s)	Exc. Force (N)	Run 1	Run 2	Failure	Strong	Weak	Failure
120	68.6	100	0	0	100	0	0
205	59.1	100	0	0	100	0	0
300	50.0	100	0	0	100	0	0
440	91.9	100	0	0	100	0	0
650	173.2	91.2	8.8	0	94.8	0.4	4.8
1280	83.2	100	0	0	100	0	0
1800	50.0	100	0	0	100	0	0
2340	150.3	100	0	0	100	0	0
2750	263.7	100	0	0	100	0	0

Compensated Dynamic Force - Convergence Table

Test Condition		Convergence (%)			Result (%)		
Freq. (rad/s)	Exc. Force (N)	Run 1	Run 2	Failure	Strong	Weak	Failure
120	50.0	100	0	0	100	0	0
205	50.0	100	0	0	100	0	0
300	50.0	100	0	0	100	0	0
440	50.0	100	0	0	100	0	0
650	50.0	100	0	0	100	0	0
1280	50.0	100	0	0	100	0	0
1800	50.0	100	0	0	100	0	0
2340	50.0	100	0	0	100	0	0
2750	50.0	100	0	0	100	0	0

50 N Dynamic Force - Convergence Table

Test Condition		Convergence (%)			Result (%)		
Freq. (rad/s)	Exc. Force (N)	Run 1	Run 2	Failure	Strong	Weak	Failure
120	350	100	0	0	100	0	0
205	350	69.2	25.2	5.6	88.8	4.0	7.2
300	350	70.8	18.8	10.4	88.4	0.8	10.8
440	350	94.0	6.0	0	91.2	3.6	5.2
650	350	75.6	19.6	4.8	88.8	2.4	8.8
1280	350	73.6	22.4	4.0	80.8	7.6	11.6
1800	350	100	0	0	100	0	0
2340	350	100	0	0	100	0	0
2750	350	100	0	0	100	0	0

350 N Dynamic Load - Convergence Table

	Amplitude Error (%)			Phase Error (deg)		
Freq. (rad/s)	Lower	**Median**	Upper	Lower	**Median**	Upper
120	1.600	**1.630**	1.660	0.444	**0.461**	0.495
205	0.460	**0.530**	0.570	0.246	**0.283**	0.312
300	0.160	**0.170**	0.190	0.175	**0.197**	0.210
440	0.190	**0.225**	0.300	0.036	**0.041**	0.057
650	0.094	**0.122**	0.169	0.017	**0.021**	0.027
1280	0.680	**0.790**	0.860	0.037	**0.040**	0.046
1800	0.680	**0.730**	0.790	0.375	**0.416**	0.458
2340	0.230	**0.248**	0.260	0.226	**0.265**	0.295
2750	0.351	**0.377**	0.398	0.148	**0.173**	0.219

Compensated Dynamic Force - Amplitude & Phase Errors

	Amplitude Error (%)			Phase Error (deg)		
Freq. (rad/s)	Lower	**Median**	Upper	Lower	**Median**	Upper
120	2.206	**2.240**	2.270	0.502	**0.530**	0.552
205	0.518	**0.570**	0.610	0.290	**0.343**	0.396
300	0.160	**0.170**	0.190	0.175	**0.197**	0.210
440	0.350	**0.370**	0.470	0.068	**0.073**	0.090
650	0.590	**0.763**	0.960	0.054	**0.062**	0.075
1280	1.230	**1.369**	1.560	0.061	**0.065**	0.073
1800	0.680	**0.730**	0.790	0.375	**0.416**	0.458
2340	0.570	**0.660**	0.710	0.632	**0.749**	0.986
2750	2.190	**2.280**	2.350	0.602	**0.686**	0.801

50 N Dynamic Load - Amplitude & Phase Errors

	Amplitude Error (%)			Phase Error (deg)		
Freq. (rad/s)	Lower	**Median**	Upper	Lower	**Median**	Upper
120	0.282	**0.300**	0.318	0.090	**0.099**	0.114
205	0.080	**0.105**	0.143	0.137	**0.191**	0.263
300	.030	**0.044**	0.060	0.022	**0.030**	0.048
440	0.066	**0.083**	0.100	0.015	**0.020**	0.024
650	0.023	**0.030**	0.040	0.011	**0.015**	0.018
1280	0.062	**0.092**	0.120	0.033	**0.052**	0.061
1800	0.116	**0.127**	0.137	0.040	**0.047**	0.056
2340	0.085	**0.100**	0.110	0.113	**0.133**	0.153
2750	0.278	**0.299**	0.310	0.096	**0.111**	0.136

350 N Dynamic Load - Amplitude & Phase Errors

B.2 Bearing 2

Test Condition		Convergence (%)			Result (%)		
Freq. (rad/s)	Exc. Force (N)	Run 1	Run 2	Failure	Strong	Weak	Failure
120	236	100	0	0	100	0	0
205	213	80.0	18.4	1.6	94.4	2.0	3.6
300	193	92.4	7.6	0	97.2	2.0	0.8
440	338	100	0	0	91.2	4.0	4.8
650	525	77.2	17.2	5.6	84.8	3.6	11.6
1280	382	90.4	8.8	0.8	91.6	3.2	5.2
1800	286	88.0	11.6	0.4	92.4	2.4	5.2
2340	162	100	0	0	90.8	4.0	5.2
2750	66	100	0	0	100	0	0

Compensated Dynamic Force - Convergence Table

Test Condition		Convergence (%)			Result (%)		
Freq. (rad/s)	Exc. Force (N)	Run 1	Run 2	Failure	Strong	Weak	Failure
120	50.0	100	0	0	100	0	0
205	50.0	100	0	0	100	0	0
300	50.0	100	0	0	100	0	0
440	50.0	100	0	0	100	0	0
650	50.0	100	0	0	100	0	0
1280	50.0	100	0	0	100	0	0
1800	50.0	100	0	0	100	0	0
2340	50.0	100	0	0	100	0	0
2750	50.0	100	0	0	100	0	0

50 N Dynamic Force - Convergence Table

Test Condition		Convergence (%)			Result (%)		
Freq. (rad/s)	Exc. Force (N)	Run 1	Run 2	Failure	Strong	Weak	Failure
120	350	100	0	0	100	0	0
205	350	74.8	22.4	2.8	92.8	2.8	4.4
300	350	72.0	24.0	4.0	95.6	0.4	4.0
440	350	100	0	0	90.4	4.4	5.2
650	350	85.2	14.0	0.8	90.8	2.8	6.4
1280	350	94.0	5.6	0.4	92.0	1.6	6.4
1800	350	83.6	12.4	4.0	87.2	3.6	9.2
2340	350	75.6	21.2	3.2	75.6	8.4	16.0
2750	350	99.2	0.8	0	90.0	5.2	4.8

350 N Dynamic Force - Convergence Table

	Amplitude Error (%)			Phase Error (deg)		
Freq. (rad/s)	Lower	**Median**	Upper	Lower	**Median**	Upper
120	0.470	**0.480**	0.491	0.093	**0.107**	0.124
205	0.110	**0.146**	0.180	0.101	**0.135**	0.179
300	0.035	**0.045**	0.051	0.040	**0.052**	0.061
440	0.080	**0.100**	0.126	0.020	**0.025**	0.036
650	0.030	**0.040**	0.060	0.012	**0.016**	0.022
1280	0.070	**0.090**	0.120	0.023	**0.027**	0.030
1800	0.200	**0.240**	0.287	0.011	**0.013**	0.016
2340	0.350	**0.411**	0.470	0.027	**0.032**	0.037
2750	1.126	**1.150**	1.200	0.258	**0.268**	0.283

Compensated Dynamic Force - Amplitude & Phase Errors

	Amplitude Error (%)			Phase Error (deg)		
Freq. (rad/s)	Lower	**Median**	Upper	Lower	**Median**	Upper
120	2.226	**2.260**	2.290	0.503	**0.532**	0.553
205	0.610	**0.655**	0.700	0.272	**0.308**	0.350
300	0.160	**0.175**	0.193	0.186	**0.204**	0.231
440	0.314	**0.330**	0.370	0.066	**0.072**	0.086
650	0.602	**0.820**	1.021	0.061	**0.074**	0.090
1280	1.949	**2.060**	2.240	0.051	**0.059**	0.067
1800	2.161	**2.298**	2.410	0.013	**0.015**	0.018
2340	1.489	**1.609**	1.700	0.093	**0.098**	0.102
2750	1.490	**1.555**	1.602	0.327	**0.349**	0.365

50 N Dynamic Force - Amplitude & Phase Errors

	Amplitude Error (%)			Phase Error (deg)		
Freq. (rad/s)	Lower	**Median**	Upper	Lower	**Median**	Upper
120	0.289	**0.300**	0.315	0.087	**0.098**	0.111
205	0.060	**0.076**	0.090	0.154	**0.221**	0.294
300	0.027	**0.030**	0.042	0.027	**0.035**	0.042
440	0.080	**0.100**	0.135	0.019	**0.022**	0.030
650	0.026	**0.034**	0.048	0.010	**0.014**	0.018
1280	0.080	**0.108**	0.150	0.023	**0.028**	0.033
1800	0.200	**0.200**	0.237	0.011	**0.016**	0.022
2340	0.260	**0.260**	0.340	0.023	**0.028**	0.042
2750	0.116	**0.140**	0.160	0.035	**0.041**	0.054

Table 13: 350 N Dynamic Force - Amplitude & Phase Errors

C Sensor Transforms

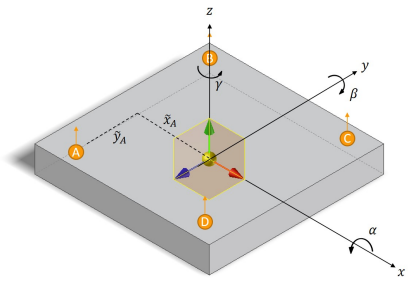

(a) Sensor A

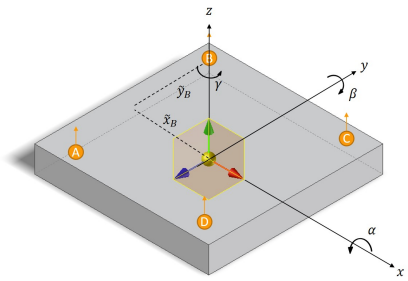

(b) Sensor B

$$[Q_{SA}] = \begin{bmatrix} 1 & 0 & 0 & 0 & \tilde{z}_{SA} & -\tilde{y}_{SA} \\ 0 & 1 & 0 & -\tilde{z}_{SA} & 0 & \tilde{x}_{SA} \\ 0 & 0 & 1 & \tilde{y}_{SA} & -\tilde{x}_{SA} & 0 \end{bmatrix}$$

$$[Q_{SB}] = \begin{bmatrix} 1 & 0 & 0 & 0 & \tilde{z}_{SB} & -\tilde{y}_{SB} \\ 0 & 1 & 0 & -\tilde{z}_{SB} & 0 & \tilde{x}_{SB} \\ 0 & 0 & 1 & \tilde{y}_{SB} & -\tilde{x}_{SB} & 0 \end{bmatrix}$$

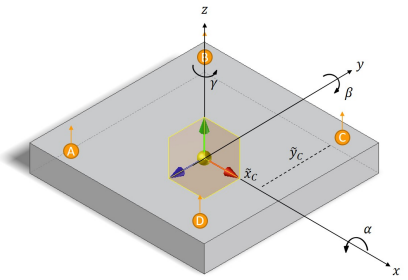

(a) Sensor C

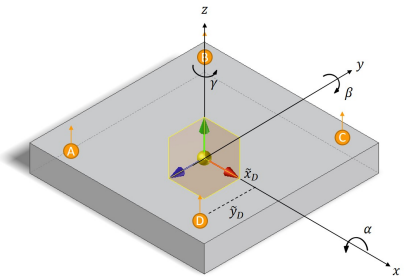

(b) Sensor D

$$[Q_{SC}] = \begin{bmatrix} 1 & 0 & 0 & 0 & \tilde{z}_{SC} & -\tilde{y}_{SC} \\ 0 & 1 & 0 & -\tilde{z}_{SC} & 0 & \tilde{x}_{SC} \\ 0 & 0 & 1 & \tilde{y}_{SC} & -\tilde{x}_{SC} & 0 \end{bmatrix}$$

$$[Q_{SD}] = \begin{bmatrix} 1 & 0 & 0 & 0 & \tilde{z}_{SD} & -\tilde{y}_{SD} \\ 0 & 1 & 0 & -\tilde{z}_{SD} & 0 & \tilde{x}_{SD} \\ 0 & 0 & 1 & \tilde{y}_{SD} & -\tilde{x}_{SD} & 0 \end{bmatrix}$$

$$[Q_S] = \begin{bmatrix} Q_{SA} & Q_{SB} & Q_{SC} & Q_{SD} \end{bmatrix}^T$$

D Actuator Transforms

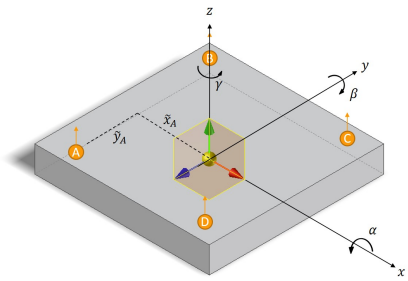

(a) Sensor A

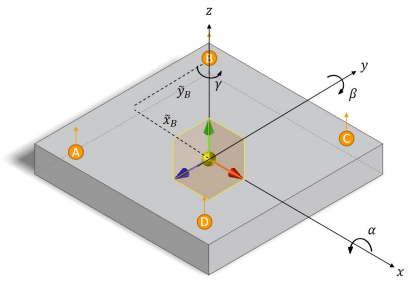

(b) Sensor B

$$[Q_A] = \begin{bmatrix} 1 & 0 & 0 & 0 & \tilde{z}_A & -\tilde{y}_A \\ 0 & 1 & 0 & -\tilde{z}_A & 0 & \tilde{x}_A \\ 0 & 0 & 1 & \tilde{y}_A & -\tilde{x}_A & 0 \end{bmatrix}$$

$$[Q_B] = \begin{bmatrix} 1 & 0 & 0 & 0 & \tilde{z}_B & -\tilde{y}_B \\ 0 & 1 & 0 & -\tilde{z}_B & 0 & \tilde{x}_B \\ 0 & 0 & 1 & \tilde{y}_B & -\tilde{x}_B & 0 \end{bmatrix}$$

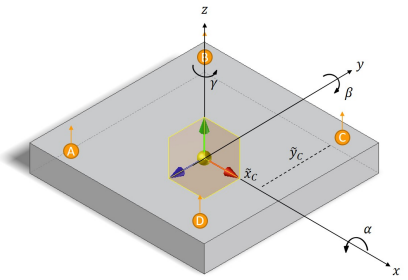

(a) Sensor C

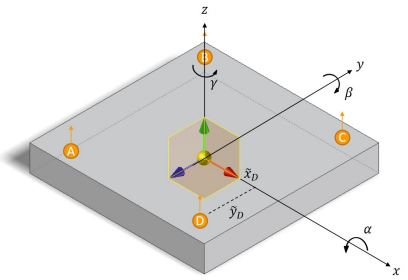

(b) Sensor D

$$[Q_C] = \begin{bmatrix} 1 & 0 & 0 & 0 & \tilde{z}_C & -\tilde{y}_C \\ 0 & 1 & 0 & -\tilde{z}_C & 0 & \tilde{x}_C \\ 0 & 0 & 1 & \tilde{y}_C & -\tilde{x}_C & 0 \end{bmatrix}$$

$$[Q_D] = \begin{bmatrix} 1 & 0 & 0 & 0 & \tilde{z}_D & -\tilde{y}_D \\ 0 & 1 & 0 & -\tilde{z}_D & 0 & \tilde{x}_D \\ 0 & 0 & 1 & \tilde{y}_D & -\tilde{x}_D & 0 \end{bmatrix}$$

$$[Q_{Act}] = \begin{bmatrix} Q_A & Q_B & Q_C & Q_D \end{bmatrix}^T$$

E Solid Body Matrices

E.1 Rotor

Mass Matrix

$$M_r = \begin{bmatrix} m_r & 0 & 0 & 0 & 0 & 0 \\ 0 & m_r & 0 & 0 & 0 & 0 \\ 0 & 0 & m_r & 0 & 0 & 0 \\ 0 & 0 & 0 & I_{xx,r} & I_{xy,r} & I_{xz,r} \\ 0 & 0 & 0 & I_{xy,r} & I_{yy,r} & I_{yz,r} \\ 0 & 0 & 0 & I_{xz,r} & I_{yz,r} & I_{zz,r} \end{bmatrix}$$

Stiffness Matrix

$$K_r = \begin{bmatrix} k_{x,r} & 0 & 0 & 0 & 0 & 0 \\ 0 & k_{y,r} & 0 & 0 & 0 & 0 \\ 0 & 0 & k_{z,r} & 0 & 0 & 0 \\ 0 & 0 & 0 & k_{\alpha,r} & 0 & 0 \\ 0 & 0 & 0 & 0 & k_{\beta,r} & 0 \\ 0 & 0 & 0 & 0 & 0 & k_{\gamma,r} \end{bmatrix}$$

Damping Matrix

$$C_r = \begin{bmatrix} c_{x,r} & 0 & 0 & 0 & 0 & 0 \\ 0 & c_{y,r} & 0 & 0 & 0 & 0 \\ 0 & 0 & c_{z,r} & 0 & 0 & 0 \\ 0 & 0 & 0 & c_{\alpha,r} & 0 & 0 \\ 0 & 0 & 0 & 0 & c_{\beta,r} & 0 \\ 0 & 0 & 0 & 0 & 0 & c_{\gamma,r} \end{bmatrix}$$

E.2 Housing

Mass Matrix

$$M_h = \begin{bmatrix} m_h & 0 & 0 & 0 & 0 & 0 \\ 0 & m_h & 0 & 0 & 0 & 0 \\ 0 & 0 & m_h & 0 & 0 & 0 \\ 0 & 0 & 0 & I_{xx,h} & I_{xy,h} & I_{xz,h} \\ 0 & 0 & 0 & I_{xy,h} & I_{yy,h} & I_{yz,h} \\ 0 & 0 & 0 & I_{xz,h} & I_{yz,h} & I_{zz,h} \end{bmatrix}$$

Stiffness Matrix

$$K_h = \begin{bmatrix} k_{x,h} & 0 & 0 & 0 & 0 & 0 \\ 0 & k_{y,h} & 0 & 0 & 0 & 0 \\ 0 & 0 & k_{z,h} & 0 & 0 & 0 \\ 0 & 0 & 0 & k_{\alpha,h} & 0 & 0 \\ 0 & 0 & 0 & 0 & k_{\beta,h} & 0 \\ 0 & 0 & 0 & 0 & 0 & k_{\gamma,h} \end{bmatrix}$$

Damping Matrix

$$C_h = \begin{bmatrix} c_{x,h} & 0 & 0 & 0 & 0 & 0 \\ 0 & c_{y,h} & 0 & 0 & 0 & 0 \\ 0 & 0 & c_{z,h} & 0 & 0 & 0 \\ 0 & 0 & 0 & c_{\alpha,h} & 0 & 0 \\ 0 & 0 & 0 & 0 & c_{\beta,h} & 0 \\ 0 & 0 & 0 & 0 & 0 & c_{\gamma,h} \end{bmatrix}$$

E.3 Bearing

Stiffness Matrix

$$K_b = \begin{bmatrix} k_{xx,b} & k_{xy,b} & k_{xz,b} & 0 & 0 & 0 \\ k_{xy,b} & k_{yy,b} & k_{yz,b} & 0 & 0 & 0 \\ k_{xz,b} & k_{yz,b} & k_{zz,b} & 0 & 0 & 0 \\ 0 & 0 & 0 & k_{\alpha,b} & 0 & 0 \\ 0 & 0 & 0 & 0 & k_{\beta,b} & 0 \\ 0 & 0 & 0 & 0 & 0 & k_{\gamma,b} \end{bmatrix}$$

Damping Matrix

$$C_b = \begin{bmatrix} c_{xx,b} & c_{xy,b} & c_{xz,b} & 0 & 0 & 0 \\ c_{xy,b} & c_{yy,b} & c_{yz,b} & 0 & 0 & 0 \\ c_{xz,b} & c_{yz,b} & c_{zz,b} & 0 & 0 & 0 \\ 0 & 0 & 0 & c_{\alpha,b} & 0 & 0 \\ 0 & 0 & 0 & 0 & c_{\beta,b} & 0 \\ 0 & 0 & 0 & 0 & 0 & c_{\gamma,b} \end{bmatrix}$$

F Matlab/Simulink Models

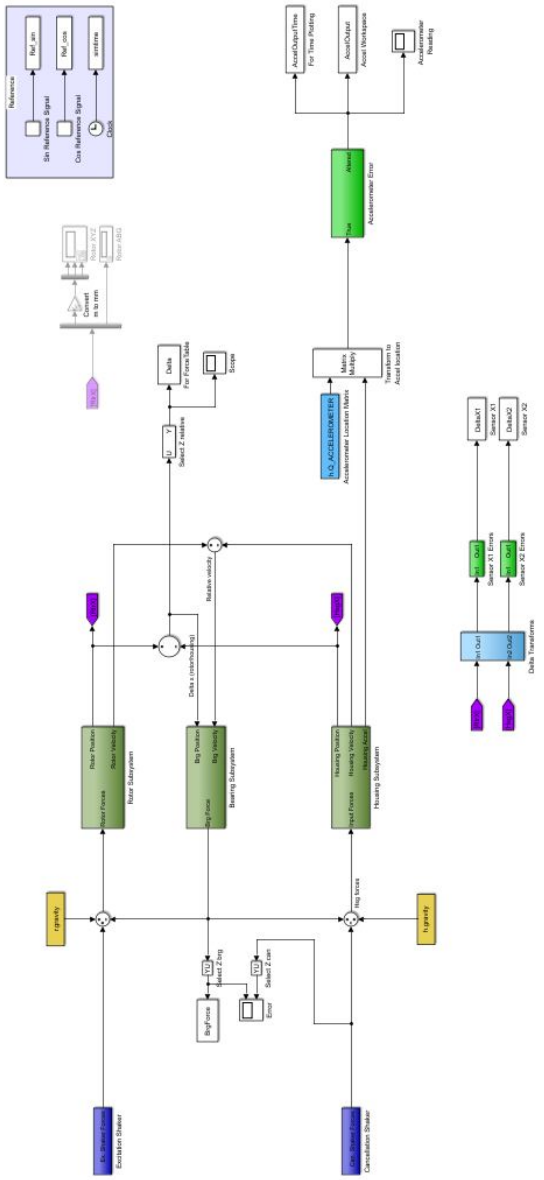

Figure F.1: Simulink Model Overview

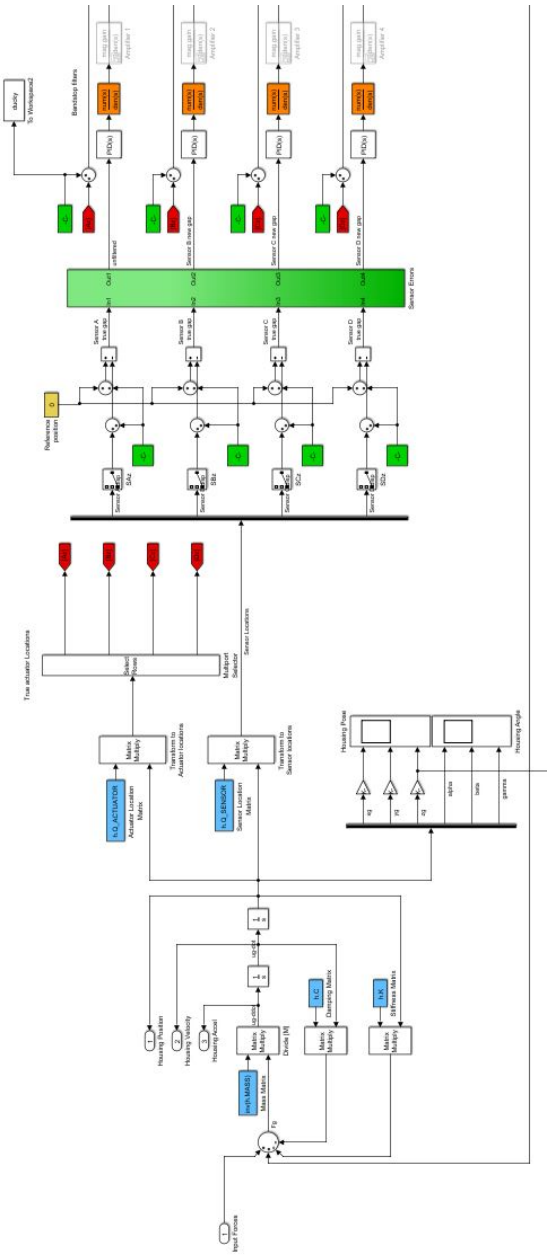

Figure F.2: Housing & Magnetic Subsystem (part 1)

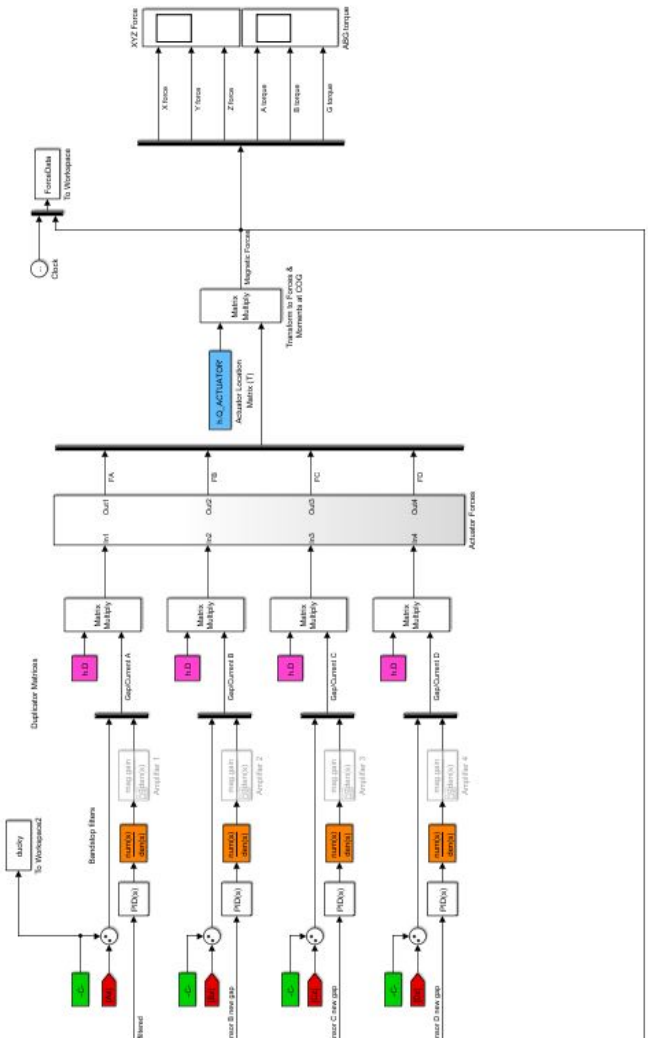

Figure F.3: Housing & Magnetic Subsystem (part 2)

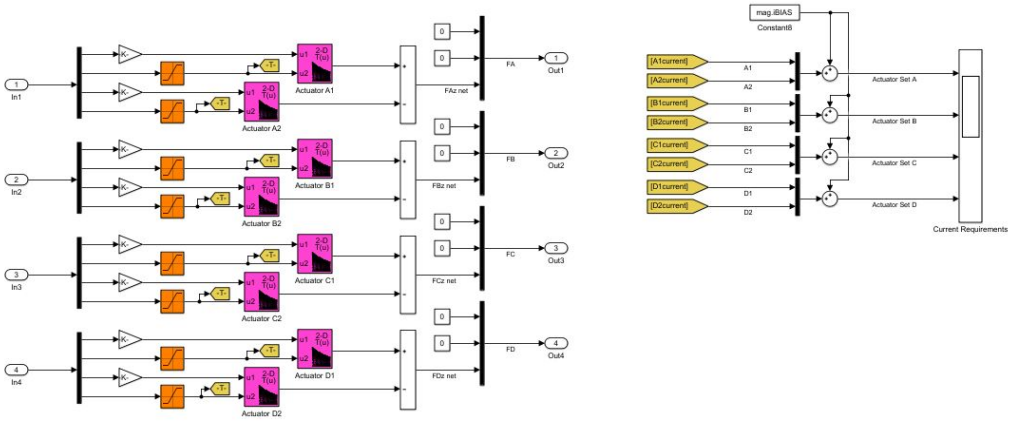

Figure F.4: Magnetic Actuator models

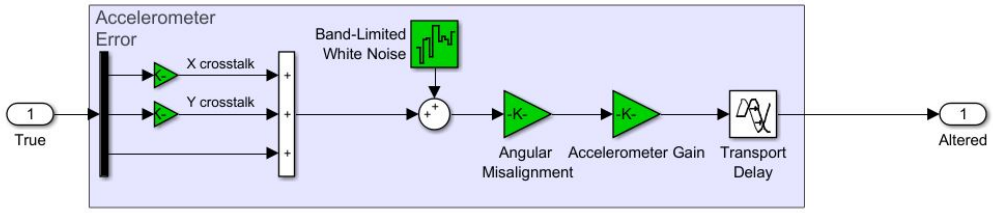

Figure F.5: Accelerometer Errors

G Equipment Documentation

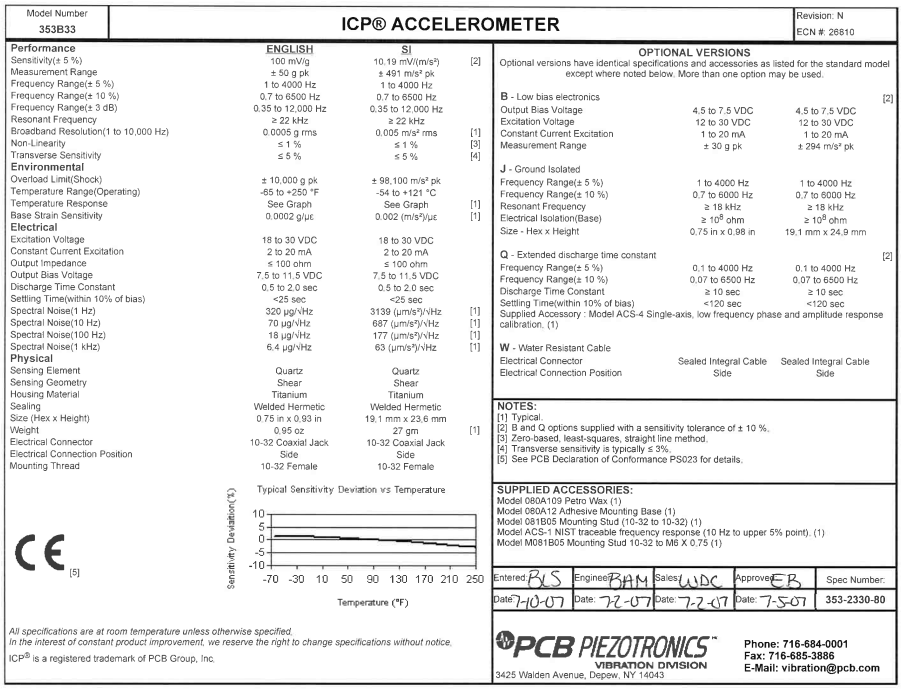

Model Number	ICP® ACCELEROMETER	Revision: N
353B33		ECN #: 26810

Performance	ENGLISH	SI	
Sensitivity(± 5 %)	100 mV/g	10.19 mV/(m/s²)	[2]
Measurement Range	± 50 g pk	± 491 m/s² pk	
Frequency Range(± 5 %)	1 to 4000 Hz	1 to 4000 Hz	
Frequency Range(± 10 %)	0.7 to 6500 Hz	0.7 to 6500 Hz	
Frequency Range(± 3 dB)	0.35 to 12,000 Hz	0.35 to 12,000 Hz	
Resonant Frequency	≥ 22 kHz	≥ 22 kHz	
Broadband Resolution(1 to 10,000 Hz)	0.0005 g rms	0.005 m/s² rms	[1]
Non-Linearity	≤ 1 %	≤ 1 %	[3]
Transverse Sensitivity	≤ 5 %	≤ 5 %	[4]
Environmental			
Overload Limit(Shock)	± 10,000 g pk	± 98,100 m/s² pk	
Temperature Range(Operating)	-65 to +250 °F	-54 to +121 °C	
Temperature Response	See Graph	See Graph	[1]
Base Strain Sensitivity	0.0002 g/με	0.002 (m/s²)/με	[1]
Electrical			
Excitation Voltage	18 to 30 VDC	18 to 30 VDC	
Constant Current Excitation	2 to 20 mA	2 to 20 mA	
Output Impedance	≤ 100 ohm	≤ 100 ohm	
Output Bias Voltage	7.5 to 11.5 VDC	7.5 to 11.5 VDC	
Discharge Time Constant	0.5 to 2.0 sec	0.5 to 2.0 sec	
Settling Time(within 10% of bias)	<25 sec	<25 sec	
Spectral Noise(1 Hz)	320 μg/√Hz	3139 (μm/s²)/√Hz	[1]
Spectral Noise(10 Hz)	70 μg/√Hz	687 (μm/s²)/√Hz	[1]
Spectral Noise(100 Hz)	18 μg/√Hz	177 (μm/s²)/√Hz	[1]
Spectral Noise(1 kHz)	6.4 μg/√Hz	63 (μm/s²)/√Hz	[1]
Physical			
Sensing Element	Quartz	Quartz	
Sensing Geometry	Shear	Shear	
Housing Material	Titanium	Titanium	
Sealing	Welded Hermetic	Welded Hermetic	
Size (Hex x Height)	0.75 in x 0.93 in	19.1 mm x 23.6 mm	
Weight	0.95 oz	27 gm	[1]
Electrical Connector	10-32 Coaxial Jack	10-32 Coaxial Jack	
Electrical Connection Position	Side	Side	
Mounting Thread	10-32 Female	10-32 Female	

CE [5]

Typical Sensitivity Deviation vs Temperature

All specifications are at room temperature unless otherwise specified.
In the interest of constant product improvement, we reserve the right to change specifications without notice.

ICP® is a registered trademark of PCB Group, Inc.

OPTIONAL VERSIONS

Optional versions have identical specifications and accessories as listed for the standard model except where noted below. More than one option may be used.

B - Low bias electronics			[2]
Output Bias Voltage	4.5 to 7.5 VDC	4.5 to 7.5 VDC	
Excitation Voltage	12 to 30 VDC	12 to 30 VDC	
Constant Current Excitation	1 to 20 mA	1 to 20 mA	
Measurement Range	± 30 g pk	± 294 m/s² pk	
J - Ground Isolated			
Frequency Range(± 5 %)	1 to 4000 Hz	1 to 4000 Hz	
Frequency Range(± 10 %)	0.7 to 6000 Hz	0.7 to 6000 Hz	
Resonant Frequency	≥ 18 kHz	≥ 18 kHz	
Electrical Isolation(Base)	≥ 10^8 ohm	≥ 10^8 ohm	
Size - Hex x Height	0.75 in x 0.98 in	19.1 mm x 24.9 mm	
Q - Extended discharge time constant			[2]
Frequency Range(± 5 %)	0.1 to 4000 Hz	0.1 to 4000 Hz	
Frequency Range(± 10 %)	0.07 to 6500 Hz	0.07 to 6500 Hz	
Discharge Time Constant	≥ 10 sec	≥ 10 sec	
Settling Time(within 10% of bias)	<120 sec	<120 sec	
Supplied Accessory : Model ACS-4 Single-axis, low frequency phase and amplitude response calibration. (1)			
W - Water Resistant Cable			
Electrical Connector	Sealed Integral Cable	Sealed Integral Cable	
Electrical Connection Position	Side	Side	

NOTES:
[1] Typical.
[2] B and Q options supplied with a sensitivity tolerance of ± 10 %.
[3] Zero-based, least-squares, straight line method.
[4] Transverse sensitivity is typically ≤ 3%.
[5] See PCB Declaration of Conformance PS023 for details.

SUPPLIED ACCESSORIES:
Model 080A109 Petro Wax (1)
Model 080A12 Adhesive Mounting Base (1)
Model 081B05 Mounting Stud (10-32 to 10-32) (1)
Model ACS-1 NIST traceable frequency response (10 Hz to upper 5% point). (1)
Model M081B05 Mounting Stud 10-32 to M6 X 0.75 (1)

Entered: BLS	Engineer: BAM	Sales: WDC	Approved: EB	Spec Number:
Date: 7-10-07	Date: 7-2-07	Date: 7-2-07	Date: 7-5-07	353-2330-80

PCB PIEZOTRONICS™
VIBRATION DIVISION
3425 Walden Avenue, Depew, NY 14043

Phone: 716-684-0001
Fax: 716-685-3886
E-Mail: vibration@pcb.com

Figure G.1: Accelerometer, from PCB Piezoelectronics

Elite Series Sensor Modules

CPL190 Single Range CPL290 Dual Range Sub-Nanometer Sensor Modules

The CPL190 has one range (sensitivity); the CPL290 has two ranges.

- High resolution
- Five-element range indicator
- Coarse/Fine zero adjusts
- Zero adjust disable
- Front-panel BNC analog output
- Differential output to National Instruments 68-pin connector

Specifications

Resolution[1]:	0.0005% @100 Hz 0.003% @ 15 kHz
Bandwidth:	Selectable: 100 Hz, 1, 10, 15 kHz
Linearity[2]:	<0.2% F.S. typical
Max Drift:	0.04% F.S./°C
Operating Temp:	4-50 °C
Front-Panel BNC:	±10 V, 0 Ω, 10 mA max
National Inst. Rear Conn.:	±10 V, 0 Ω, Differential

[1]Dependent on probe, range, and bandwidth. See next page for details.

[2]Dependent on probe and range. See next page for details.

Export License

Because of high resolutions, export of the Elite Series to some countries requires an export license.

Ranges/Probes Table (Next Page)

The CPL190/CPL290 uses **Standard Probes**. Standard Probe ranges and performance specifications are on the next page.

Range is determined by the probe Sensing Area diameter. The larger the diameter, the larger the range.

Listed specifications assume a 2 meter probe cable; flat measurement area diameter at least 1.3 times larger than the Sensing Area diameter; and no customizations.

Standard Probe mechanical details are on page 18.

Different probe body styles/sizes are available for each Sensing Area.

Elite Series

Standard Probes and Ranges for use with the CPL190 and CPL290 Capacitive Sensor Modules

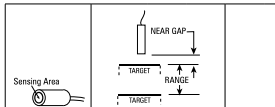

Sensing Area Diameter mm	Measurement Range: Range Type	Range µm mils	Near Gap µm mils	Resolution[1] @ Bandwidth: 100 Hz nm µin	1 kHz nm µin	10 kHz nm µin	15 kHz nm µin	Linearity % F.S.	Available Body Sizes: Models	Body Styles
0.5	Fine	10 0.4	20 0.8	0.05 0.003	0.10 0.004	0.40 0.016	0.50 0.020	0.25	C3S C3R C5S C5R C5	
	Standard	50 2.0	50 2.0	0.30 0.012	0.50 0.020	3.0 0.12	4.0 0.16	0.25		
	Extended	80 3.0	60 2.4	0.50 0.020	1.0 0.040	5.0 0.20	—	0.25		
0.8	Fine	25 1.0	75 3.0	0.20 0.008	0.50 0.020	1.2 0.050	1.5 0.060	0.15	C3S C3R C5S C5R C5	
	Standard	100 4.0	100 4.0	0.50 0.020	1.0 0.040	3.5 0.14	5.0 0.20	0.15		
2.0	Ultrafine	10 0.4	20 0.8	0.05 0.002	0.08 0.003	0.15 0.006	0.25 0.010	0.15	C5S C5R C5 C8S C8R C8	
	Fine	50 2.0	75 3.0	0.20 0.008	0.30 0.010	0.60 0.024	1.0 0.040	0.15		
	Standard	250 10.0	125 5.0	0.8 0.030	1.0 0.040	4.0 0.16	5.0 0.20	0.10		
	Extended	500 20.0	125 5.0	1.5 0.060	3.0 0.12	8.0 0.32	10 0.40	0.15		
3.2	Fine	50 2.0	125 5.0	0.25 0.010	0.4 0.016	1.0 0.032	1.6 0.052	0.20	C8S C8R C8	
	Standard	500 20.0	250 10	2.0 0.10	3.0 0.12	6.0 0.28	10 0.40	0.15		
	Extended	1250 50.0	250 10	10 0.28	15 0.40	20 0.80	30 1.2	0.20		
5.6	Fine	50 2.0	225 9.0	0.3 0.012	0.4 0.016	0.8 0.040	1.3 0.060	0.20	C9.5S C9.5R C9.5 R20	
	Standard	500 20.0	500 20	2.5 0.080	3.0 0.12	7.0 0.24	10 0.40	0.15		
	Extended	2000 80.0	250 10	7.0 0.40	10 0.60	20 0.80	30 1.2	0.20		
13	Fine	2000 80	2000 80	20 0.80	30 1.2	35 1.4	40 1.6	0.50	C18	
	Standard	3200 125	2000 80	30 1.2	40 1.6	50 2.0	60 2.4	0.50		
	Extended	5000 200	3000 120	75 3.0	100 4.0	130 5.2	150 6.0	0.50		
19	Standard	2500 100	5000 200	50 2.0	70 2.8	90 3.6	100 4.0	0.30	R45	
	Extended	6000 250	3000 120	90 3.6	120 4.8	160 6.4	180 7.2	1.0		
21	Standard	8000 300	5000 200	75 3.0	100 4.0	130 5.2	150 6.0	0.50	C25	
	Extended	12500 500	5000 200	130 5.2	180 7.2	230 9.2	250 10	0.50		

[1]Resolution values are RMS. Peak-to-peak values are typically 8-10 times greater than the RMS values.
In high EMI conditions (10 V/m) output DC level may shift and noise may rise to 0.2 VRMS (1% resolution).

Figure G.2: Displacement Sensors, from Lion Precision

Figure G.3: Shakers, from MB Dynamics

MB Dynamics ... Innovating and Delivering Solutions ... Vibration and Shock

PM-SHAKERS

Specifications

MB **PM-Series Shakers** use *permanent magnet technology* and the voice coil principle to create vibration. These general-purpose shakers are heavy duty, industrial-quality equipment with a proven track record of lasting ten, fifteen, even over twenty years in demanding applications. You can buy "*bargain basement*" shakers or you can invest in MB **PM-Shakers** that will provide you with years of dependable, reliable, and consistent testing. Choose from five different sizes -- depending on your needs – with maximum sine force ratings of 25, 50, 100, 250 or 500 pounds.

The **PM25A**, **PM50A**, and **PM100A** Shakers all have ½" stroke and a 2.7" diameter mounting table. The **PM250HP** and **PM500HP** Shakers each have 2" of stroke and a 4.1" diameter mounting table.

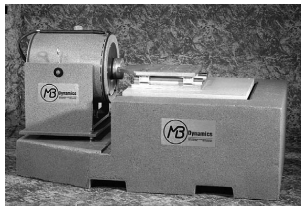

PERFORMANCE RATINGS

** Rated output with forced air cooling; Derate 50% for natural convection cooling*

Description	PM25A	PM50A	PM100A	PM250HP	PM500HP
Force Output	25 pounds Pk*	50 pounds Pk*	100 pounds Pk*	250 pounds Pk*	500 pounds Pk*
Displacement	0.5" Pk-Pk	0.5" Pk-Pk	0.5" Pk-Pk	2" Pk-Pk	2" Pk-Pk
Velocity	70 in/sec Pk	70 in/sec Pk	70 in/sec Pk	60 in/sec Pk	60 in/sec Pk
Acceleration (bare table)	80 g Pk	80 g Pk	106 g Pk	80 g Pk	80 g Pk
Frequency Range	DC-10,000 Hz	DC-10,000 Hz	DC-7000 Hz	DC-3500 Hz	DC-3000 Hz
Cooling	8 scfm @3" H_2O	13 scfm @3" H_2O	26 scfm@12" H_2O	80 scfm @30" H_2O	80 scfm @30" H_2O
Coil Current & Resistance	4 amps; 2.7 ohms	8.5 amps; 1.3 ohms	8 amps; 2.6 ohms	40 amps; .021 ohms	38 amps; 0.5 ohms
Suspension Stiffness	75 lbs/in	75 lbs/in	75 lbs/in	40 lbs/in	40 lbs/in
Stray Field - 1" over center	< 20gauss	< 7 gauss	< 8 gauss	< 40 gauss	< 20 gauss
DC Centering				Drives 25 lbs to 1" Pk-Pk with 20% force derating	Drives 50 lbs to 1" Pk-Pk with 20% force derating

MECHANICAL SPECIFICATIONS

Description	PM25A	PM50A	PM100A	PM250HP	PM500HP
Mounting Surface Bolt Holes	Six 10-32 threaded holes at 60° on 2.25" bolt circle (+ center)	Six 10-32 threaded holes at 60° on 2.25" bolt circle (+ center)	Six 10-32 threaded holes at 60° on 2.25" bolt circle (+ center)	Six ¼x28 threaded holes at 60° on 3.50" bolt circle (+ center)	Six ¼x28 threaded holes at 60° on 3.50" bolt circle (+ center)
Moving Element Diam.	2.70"	2.70"	2.70"	4.10"	4.10"
Base Footprint	10" x 7.5"	10" x 7.5"	10" x 7.5"	18" x 14"	18" x 14"
Body Diameter	7"	7"	7"	14¼"	14¼"
Height (to table top)	7½"	9½"	13½"	17¼"	20½"
Moving Element Axial Resonance	8200 Hz	8000 Hz	6000 Hz	3000 Hz	2800 Hz
Weight, Moving Element	0.50 pounds	0.62 pounds	0.94 pounds	2.6 pounds	5.0 pounds
Weight, Exciter	38 pounds	55 pounds	80 pounds	250 pounds	420 pounds
Weight, Base	7 pounds	11 pounds	15 pounds	25 pounds	25 pounds
Base Type	2-position; rigid	2-position; rigid	2-position; rigid	trunnion	trunnion
Trunnion Base	optional	optional	optional	standard	standard
Cooling Connections	0.5" NPT	0.5" NPT	0.5" NPT	2.0" port	2.0" port

Ratings & Specifications subject to change without notice 05/97)

DIMENSIONS

PM SHAKERS 25A / 50A / 100A

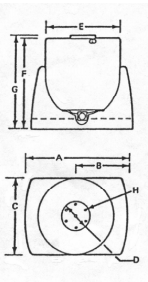

PM SHAKERS 250HP / 500HP

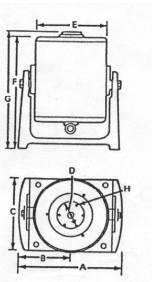

Dimensions	A	B	C	D	E	F	G	H	Cooling
PM25A	10"	5"	5 ½"	2.25"	7-3/8"	7-7/32"	7-15/32"	10-32	½ NPT connection for cooling air 8 CFM at 3" H_2O
PM50A	10"	5"	7 ½"	2.25"	7-3/8"	9-7/32"	9-15/32"	10-32	½ NPT connection for cooling air 13 CFM at 4" H_2O
PM100A	10"	5"	7 ½"	2.25"	7-3/8"	13-7/32"	13-15/32"	10-32	½ NPT connection for cooling air 26 CFM at 12" H_2O
PM250HP	18"	9"	14"	3.50"	14 ¼"	16-5/8"	17-3/16"	¼ - 28	2" connection for cooling air 80 CFM
M500HP	18"	9"	14"	3.50"	14 ¼"	19-3/4"	20-5/16"	¼ - 28	2" connection for cooling air 80 CFM

Dimensions subject to change without notice (05/97)

25865 Richmond Rd · Cleveland OH 44146 · 216-292-5850 · fax 216-292-5514 · email mbd@mbdynamics · www.mbdynamics.com

Extension Spring with Hook Ends

Spring-Tempered Steel, 2.375" Overall Length

In stock
$8.12 per pack of 6
1832K27

Spring Type	Extension
End Type	Hook
Material	Spring-Tempered Steel
Overall Length	2.375"
OD	0.75"
Wire Diameter	0.105"
Extended Length	3.004"
Load, lbs.	
Minimum	12.80
Maximum	50.00
Rate	59.19 lbs./in.
RoHS	Compliant

Figure G.4: Flexure Spring, from McMaster-Carr